LhARA-Gov-PMB-2023-xx Draft 1.0
1272-pa1-pm-rpt-0007-1.0-twelve-month-design-review-report

November 2, 2023

LhARA/ITRF: twelve month progress report

C. Baker [1], J. Bamber [2], W. Bertsche [13,5], N. Bliss [3], E. Boella [4,5], N.P. Dover [6], A. Goulden [3,5], R. Gray [7,5], E. Harris [2], M. Johnson [3,5], K. Kirkby [12,13,5], N.Kumar [5,14], A. Kurup [6,8], K.R. Long [6,8], R. Mclauchlan [9], H. Owen [3,5], J.L. Parsons [10], J. Pasternak [6,8], M. Patel [5,14], T. Price [11], C. Welsch [5,14], C. Whyte [7,5]

to be updated

1. *Department of Physics, Faculty of Science and Engineering, Swansea University, Singleton Park, Swansea, SA2 8PP*
2. *Institute of Cancer Research, UK*
3. *UKRI-STFC Daresbury Laboratory, Sci-Tech Daresbury, Daresbury, Warrington, WA4 4AD, UK*
4. *Lancaster University, UK*
5. *Cockcroft Institute, Sci-Tech Daresbury, Daresbury, Warrington, WA4 4AD, UK*
6. *The John Adams Institute for Accelerator Science, Imperial College London, Exhibition Road, London, SW7 2AZ, UK*
7. *Department of Physics, SUPA, University of Strathclyde, 16 Richmond Street, Glasgow, G1 1XQ, UK*
8. *UKRI-STFC Rutherford Appleton Laboratory, Didcot, OX11 0QX, UK*
9. *Imperial College NHS Healthcare Trust, The Bays, South Wharf Road, St Mary's Hospital, London W2 1NY, UK*
10. *Institute of Cancer and Genomic Sciences, University of Birmingham, Edgbaston, Birmingham, B15 2TT, UK*
11. *School of Physics and Astronomy, University of Birmingham, Edgbaston, Birmingham, B15 2TT, UK*
12. *Division of Cancer Sciences, Faculty of Biology, Medicine and Health, The University of Manchester, The Christie Proton Therapy Centre, The Cristie NHS Foundation Trust, Wimslow Rd, Manchester M20 4BX*
13. *Department of Physics and Astronomy, The University of Manchester, Oxford Rd, Manchester, M13 9PL, UK*
14. *Department of Physics, University of Liverpool, Oliver Lodge, Oxford Street, Liverpool, L69 7ZE*

Contents

Introduction

The Ion Therapy Research Facility (ITRF) will be a unique radiobiological research facility exploiting technologies that have the potential to transform ion-beam therapy and the treatment of "hard-to-treat" cancers. The ambition is that the ITRF will become the world-leading, compact, single-site research infrastructure that will support the multidisciplinary programme necessary to:

- Elucidate radiobiological mechanisms that underpin the clinical efficacy of particle therapy;
- Generate the accelerator, diagnostic, imaging, and computing technologies required to transform the clinical practice of IBT; and
- Deliver the capability to provide IBT in completely new regimens by combining ion species from protons to carbon exploiting ultra-high dose rates and novel spectral-, spatial- and temporal-fractionation schemes.

The UKRI Infrastructure Fund is investing £2M over two years (October 2022 to September 2024) in a Preliminary Activity (PA1) to deliver the conceptual design report (CDR) for the ITRF to be served by LhARA, the Laser-hybrid Accelerator for Radiobiological Applications. This report summarises the progress made in PA1 over the first 12 months of the project.

Development of the LhARA/ITRF programme beyond September 2024

The ITRF/LhARA programme is supported through a two-year Preliminary Activity running from 1^{st} October 2022 to 30^{th} September 2024. Over the reporting period the project team was encouraged to submit a proposal for a second Preliminary Activity (PA2) in Wave 4 of the UKRI Infrastructure Fund to support the pre-construction R&D programme from 1^{st} October 2024. The PA2 proposal was designed to build on the CDR delivered in PA1 to complete the design and planning of the ITRF construction project. ITRF PA1 has defined a two-stage implementation scheme:

- Stage 1: proton beams with energies in the range 12 MeV to 15 MeV to the Low-energy *in-vitro* End Station;
- Stage 2: proton beams of 127 MeV and ion beams of 33.4 MeV/nucleon to the High-energy *in-vitro* and *in-vivo* End Stations.

The PA2 proposal requests £21.5M over the four-year period from October 2024 to September 2028 to deliver:

- Technical Design Reports for the staged implementation of the facility;
- A site study leading to site selection and building implementation plan; and
- A proof-of-principle demonstrator system at an existing pulsed-laser facility.

0 Work package 0: Project management

0.1 Project Organisation

The ITRF project follows standard STFC project management practice, and is described in the ITRF Organisational Breakdown Structure [1]. The project comprises 4 Work Packages, with Work Package 0 responsible for delivery of the project outcomes. The first phase of the R&D programme required to mitigate the risks inherent in developing the Laser-hybrid Accelerator for Radiobiological Applications (LhARA) [2, 3] to serve the ITRF are carried out under Work Package 1. The engineering work required to develop LhARA to serve the ITRF and to deliver the ITRF facility is carried out inder Work Package 2. Work Package 3 is focused on the study of a conventional, synchrotron-based, alternative to the baseline, laser-hybrid based accelerator system, The organisation and management of the LhARA collaboration and its integration with the ITRF project management is described in [4].

Table 1: Sections and supporting documents forming the ITRF Project Management Plan (current version 1272-pa1-pm-pmp-0001-v13.0-itrf-2023-09-28).

Section	Supporting Document
Project Description	
Project Organisation	1272-pa1-pm-pmp-0004-v3.0 [8]
Objectives and Deliverables	
Project Schedule	1272-pa1-pm-ppl-0001-v2.2
	1272-pa1-pm-ppl-0004-v1.0
	1272-pa1-pm-ppl-0007-v3.0
Finance	1272-pa1-pm-fin-0002-v5.1
	1272-pa1-pm-fin-0004-v3.0
Resources	1272-pa1-pm-fin-0002-v5.1
	1272-pa1-pm-fin-0004-v3.0
Risk Management	1272-pa1-pm-risk-0001-v1.2
Stakeholder Communication	
Monitoring and Reporting	1272-pa1-pm-rpt-0001-v3.1
Quality Plan	
Benefits Realisation and Impact Plan	1272-pa1-pm-rpt-0003-v0.6
SHE Plan	
Diversity Issues	
History	

0.2 Documentation

ITRF project documents follow an STFC standardised document naming and folder structure convention [5] and are stored on the ITRF SharePoint site [6]. Documents generated by the LhARA collaboration are stored on the LhARA wiki [7]. The documents are appropriatelyt cross-referenced to ensure a complete and consistent archive.

0.3 Project Reporting and Governance

The ITRF project delivery committee (ITRF Work Package 0) meets typically bi-weekly with membership that includes Principal Investigator, Project Manager, Project Coordinator, and Work Package Managers from the 3 Work Packages:

- Work package 1: LhARA;
- Work package 2: ITRF Facilities and Costing; and
- Work package 3: Conventional Technology.

Project management is coordinated and recorded to enable the ITRF project manager to provide monthly project reports to the UKRI–STFC Project Review Committee and the UKRI Infrastructure Fund.

Project reports cover: Progress; Finance; Risk; and Issues. The ITRF project has established a Project Board and and Advisory Committee that both meet at a frequency of approximately once every 3 to 6 months. An ITRF project Roles and Responsibilities document has been established that covers the Project Sponsor, Project Manager, Project Team Members and Project Governance [8].

0.4 Quality Assurance

Project management is being conducted in accordance with the UKRI–STFC Project Management Framework and the STFC–Daresbury Laboratory ISO9001:2015 Quality Management System (QMS) [9]. Under the QMS processes and procedures, the ITRF project is subject to internal audits by STFC staff and external audits by the British Standards Institute (BSI) [10]. A Business Case [11] and Project Management Plan (PMP) [12] have been established and are regularly updated. The Business Case details the potential benefits of the project and the PMP is the top-level plan for the delivery of the project containing the subsections and related underpinning documents referenced in red text in Table 1.

1 Work package 1: LhARA

LhARA [2, 3] is conceived as the new, highly flexible, source of radiation that is required to explore the vast "terra incognita" of the mechanisms by which the biological response to ionising radiation is determined by the physical characteristics of the beam [13]. The rationales for the technological choices made to define the laser-hybrid concept are presented in the pre-CDR [2, 3], in the narative of the five-year R&D plan prepared prior to the approval of PA1 [4], and in [14]. In summary, the key elements of the rationales are:

- The laser-driven proton and ion source is capable of creating short ($\sim 10\,\mathrm{ps}$) intense pulses ($\sim 10^9$ protons per pulse, $\sim 10^8$ ions per pulse) at energies significantly larger than those that can be achieved in a traditional discharge source. The baseline energy for proton capture from the LhARA source is 15 MeV, ~ 240 times higher than a typical discharge source. The higher capture energy elegantly mitigates the current space-charge limit on the instantaneous dose rate that can be delivered [15]. The tiny spot size at source ($\sim 40\,\mu\mathrm{m}$) allows the beam to be tightly focused to deliver mini-beams without collimation if space charge effects can be managed. The laser can be triggered to deliver an arbitrary time structure, with the minimum time between pulses being determined by the repetition-rate specification of the laser; a 10 Hz repetition rate laser is specified in the LhARA baseline [16]. The laser-driven source therefore provides significantly greater flexibility in the delivery of beams for the investigation of the temporal and spatial dependence of the biological effects induced by proton and ion beams than is possible at conventional sources.
- The electron plasma (Gabor) lens provides the same focusing strength as high-field solenoids at a fraction of the cost. To maximise the capture efficiency of the divergent beam that emerges from the laser-driven source requires strong, cylindrically-symmetric focusing that maximises the geometrical acceptance for the relevant energy byte. The LhARA concept requires a lens with a focal length of around 1 metre.

  If implemented using solenoids, fields of between 1.1 T and 1.3 T are required. The design of a normal-conducting solenoid meeting these specifications has been developed [14]. The mass of the magnet is ~ 2 tons and the power consumption is estimated to be between about 100 kW and 150 kW. An initial evaluation of a superconducting magnet has been performed [17]. A particular challenge was the design of a tapered cryostat that would allow the lens to be be placed close enough to the target to preserve the capture acceptance. The issue of eddy currents induced in the superconductor by the electromagnetic pulse created by firing the laser remains to be investigated.

In contrast, the Gabor lens solution requires a solenoid magnetic field on the order of hundreds of mT with a device with a weight a fraction of that of the equivalent solenid. The plasma-lens solution, therefore, offers significant advantages in terms of investment and operational costs, and will significantly reduce the carbon footprint of the focusing system in construction and operation.

The advantages of the Gabor lens become even more compelling when considering the development of the laser-hybrid technique for clinical application. In this case, it is likely that lasers of higher power will be required to provide beams of higher energy for injection into the acceleration system. The efficient capture of such a beam will require stronger focusing, which, if delivered with conventional solenoids, will require fields in excess of 1.4 T. Such fields will require superconducting technology, most likely incurring substantially increased investment and running costs.

- Post-acceleration using a fixed-field alternating-gradient accelerator (FFA) preserves the unique flexibility in the time, energy, and spatial structure of the beam afforded by the laser-driven source.

  The alternative technological choice would be a synchrotron. For the LhARA/ITRF application, the key disadvantage of the synchrotron option lies in the fact that it will fix the time structure of bunches that can be delivered to multiples of the cycle time, thereby reducing the temporal flexibility of the facility. Furthermore, the adoption of, for example, a state-of-the-art 10 Hz rapid-cycling synchrotron would make it impossible for the ITRF to profit from the development of lasers capable of repetition rates of 100 Hz or above.

  The magnet powers-ystems of state-of-the-art synchrotrons are designed to minimise power consumption. However, energy is required both to create the magnetic field and to reduce it during the synchrotron acceleration cycle. Since—for an FFA—the magnetic field is fixed, such power losses are not incurred and it is anticipated that the power consumption during operation will be lower than the equivalent synchrotron.

1.1 Work package 1.1: Project Management

The LhARA project is managed through bi-weekly meetings of the Project Management Board (PMB) [18]. The PMB is attended by all Work Package Managers and is chaired by the LhARA Project Manager. Individual Work Packages [19–23] hold weekly or bi-weekly meetings to which the PMB and LhARA Executive Board [24] have standing invitations; attendance at these meetings allows the management team directly to engage with the R&D programme, monitor progress and stay abreast of developments.

The LhARA PMB provides monthly reports to the ITRF project manager. These reports include spend to date, highlights of progress and raise issues as they arise. The reports also include a forward look to the next months of planned activity. The monthly reports to the ITRF are condensed from monthly reports provided by the work package managers to the PMB.

Overview of progress

Progress to date has largely been as planned and no un-anticipated risks have been identified. However, LhARA has seen risks related to the recruitment of new staff and staff retention realised in WP2,3 and 5. WP1.3 has been most seriously affected with a full year's delay incurred by a combination of University administrative paperwork, advertising of the position, availability of recruits and ultimately UK border control delays of 6 months. WP1.3 has managed the situation through the provision of additional manpower resource from within the Swansea University group, but the planned experimental campaign has been significantly delayed. Milestone 3.1 was moved back to March 24. Milestones 3.2 and 3.3 can still be delivered within the PA1 timeframe, but the level of detail will be reduced. A no-cost extension was required at Swansea to enable the recruitment. This will ensure the planned effort is delivered to the project as the results become available.

WP1.2 experienced similar delays to new staff recruitment for the modelling effort, ultimately resulting in a full years delay in securing staff in post. This issue was initially mitigated by additional effort from the Lancaster PI along with windfall access to HPC resources worth £40k, secured in open competition. In April 2023, the Lancaster PI resigned their position at Lancaster. A new PI is in place and the new PDRA staff member is being supported by the rest of the WP2 staff who have also been able to source some limited additional simulation resource from their own groups. The impact of this has been largely confined to the simulation aspects of Milestone 2.1. LhARA management have allowed WP1.2 to slip the simulation part of Milestone 2.1 to May 2024 to fully exploit the staffing resources that are now available. Milestone 2.1 is not a pre-cursor for following work and the only requirement is that the results are available in good time for the final report in September 2024, there is therefore no reason to hold the original milestone date. Similarly to WP1.3, the full resources planned for the PDRA recruitment were committed at the time the post was advertised.

Staff recruitment issues have arisen in two areas of WP5. The effort of ther PDRA recruited to contribute to the beam-intrumentation work was recruited in Liverpool to contribute to LhARA and other projecs. The impact on the LhARA programme could therefore be partially mitigated by other staff. Delays were experienced as a result of delayed recruitment, but, staff were able to provide the required additional effort to complete deliverables to schedule. The second point of underspend in WP1.5 is related to the buyout of the NHS Medical Physics staff member. Freeing the individual from clinical commitments has proved problematic at the management level as the part-time resource required to replace the effort bought out for LhARA hass not been available for purchase. The net result has been prioritisation of NHS related work and reduced, though important, input to LhARA. The solution to this problem requires management-level input which is currently being discussed.

Earned value

A preliminary earned-value analysis is presented in figure 1. For a task, work package, or project, the earned value (EV) is defined to be the the total value ("budget at completion") of the task, work package or project multiplied by the fraction (fC) of the task, work package or project that has been completed. Cost variance (CV) is then by:

$$CV = EV - AC\,;$$

where AC is that "actual cost" of executing the fraction work-fraction fC. Schedule variance (SV) is given by:

$$CV = EV - PV\,;$$

where PV is the planned value of the fraction of work complete. Budget variance (BV) is defined by:

$$BV = Spnd - PV\,;$$

where $Spnd$ is the total spend on the work performed. The cost performance index and schedule performance indices, CPI and SPI respectively are defined by:

$$\begin{aligned} CPI &= \frac{EV}{Spnd}\,;\text{and} \\ SPI &= \frac{PV}{EV}\,. \end{aligned}$$

where $Spnd$ is the total spend on the work performed. The performance indices in figure 1 indicate that, in the initial few months, reporting was not uniformly accurate across the work packages. Missing data led to unreasonably high CPI figures which self-corrected once financial reporting was established. The Values (EV, PV and $Spnd$) record the underspend on staff identified above which persists to date. With all staff now in place we expect the future Value graphs to match in gradient if not in magnitude. The variance graphs tell

the same story, LhARA has accumulated an underspend of close to £200k or 13%, the majority of which is not amenable to intervention as the funds lie with the universities, held against future salary commitments.

WP1.6 experienced some delays in the delivery of reports internal to the LhARA project and not reflected in the higher level ITRF milestones or deliverables. The LhARA Stage 1 beamline required additional work including a switch from a 5 element design to one using 7 Gabor lenses. The new configuration offers improved flexibility to deliver both the required range of beam sizes at the endstation and also a beam suitable for injection into the FFA. In the process of completing this work, an update to the predicted dose calculations was made and cross checked against independent calculations. The variations were small, but combined with the other changes, an update of the LhARA baseline has been prepared for discussion prior to its adoption as the new baseline.

Development of baseline configuration and radiation-biology programme

A first update of the LhARA FFA design has been developed and the project teams is working towards a formal revision of the baseline. The revision of the baseline will follow the change-control procedude defined in [16]. The status of the work is is reported in section 1.6. Work will now be required to translate the magnet field maps into engineering input which can be adopted into the CAD model of the facility. During the FFA re-design a change in the FFA average diameter was required as well as adjustments to the magnet configuration. It will be important to capture these changes and construct an accurate CAD model capable of identifying space conflicts for the additonal FFA components yet to be designed including the FFA RF cavities and injection/extraction lines.

The LhARA collaboration has started the process of refining and documenting its radiobiology objectives, ahead of an international expert review of these aspects of the LhARA programme. The review of the radiobiology programme will follow a process similar to the autumn 2022 review: a panel of internationally-recognised experts will be convened and charged with interrogating the LhARA collaboration's objectives. The outcomes of this radiobiology review will be recorded on the LhARA wiki [7] and in an expanded LhARA radiobiological-science baseline document.

Highlights of progress

Progress in the individual work packages is covered in the sections which follow and will not be repeated here. Highlights of the programme to date include:

- The first two peer-group-consultation meetings have taken place (see [25, 26]). Each was well attended and engaged participants from the UK and overseas.
- Revision of the low-energy Stage 1 transport line and FFA designs. The revision of the Stage 1 beam line design is now being documented in detail. In line with the agreed process by which changes are made to the LhARA baseline, a request to change the Stage 1 beam line will be presented to the collaboration on the 7^{th} November 2023. The PMB and EB will then consider any issues raised. Since the revised Stage 1 beam line provides significant additional flexibility and preserves the performance of the system, it is anticipated that the change request will be agreed.
- Examination and revision of the simulation required to estimate the dose that will be delivered to the endstations. This work will be documented in the baseline-change request mentioned above.
- Detailed discussions on the ion source/capture interfaces and low energy line configuration. The discussions have led to an improved understanding of the challenges in this area and new solutions have been found, providing much improved access to the source while preserving the operational functionality.
- The design of a proof-of-principle experiment to demonstrate the ion-acoustic dose-profile measurement technique is and discussions with LMU on a possible collaborative experiment on the LION beam line of the CALA facility in Munich.

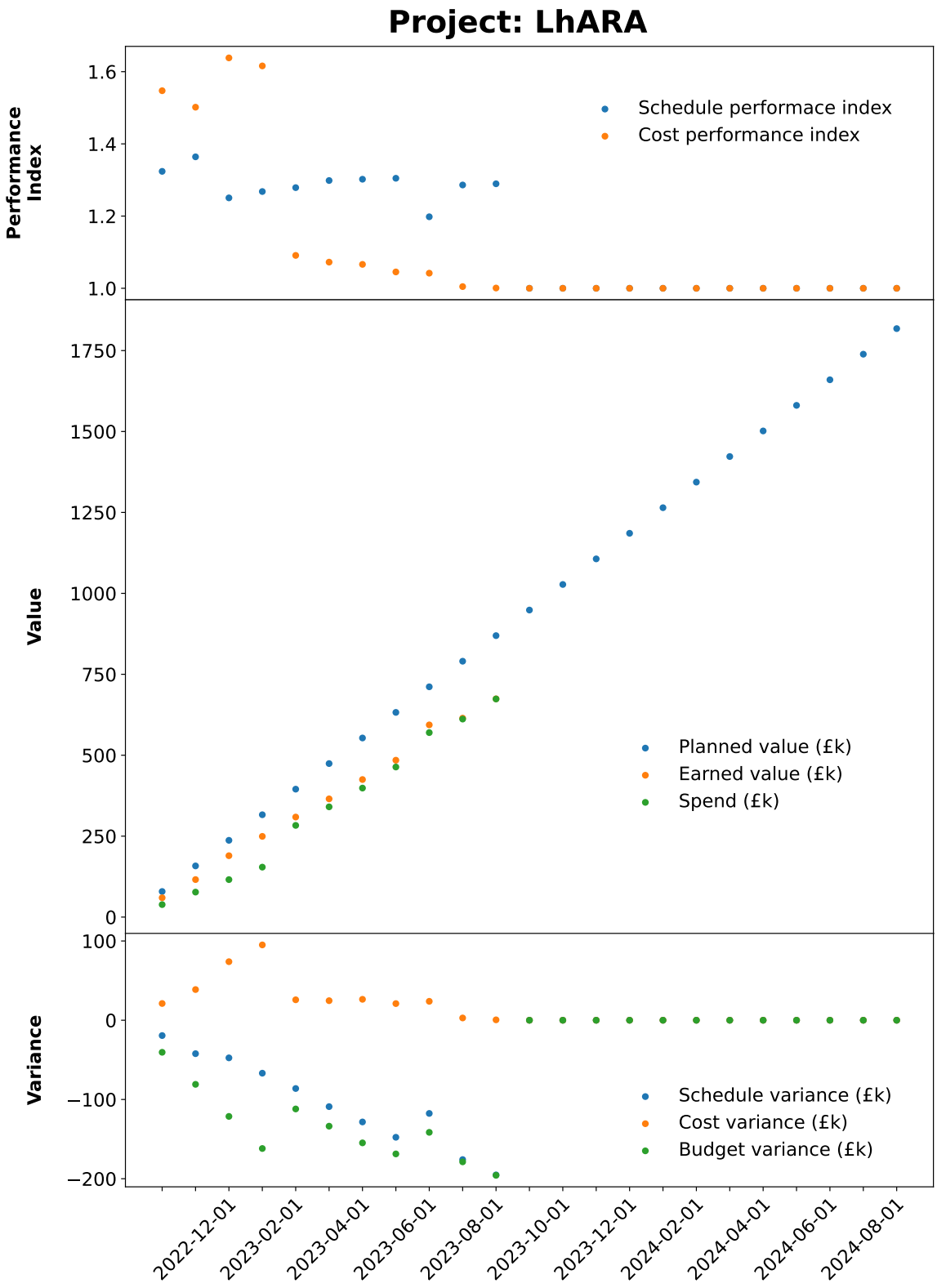

Figure 1: LhARA earned value analysis. The definitions of the various performance indicators plotted are defined in the text.

- The first period of continuous high repetition rate running has been completed at SCAPA. Analysis of the results is ongoing. Initial feedback from the experimental results will be used to guide the next phase of simulations.

The third LhARA collaboration meeting was held in February 2023 at the University of Birmingham [27]. Discussion was robust with a full day's material presented to the collaboration. The date was chosen to coincide with the mid-term break in teaching; this led to the meeting occurring 6 weeks in advance of the preparation of the ITRF six-monthly progress report.

LhARA Collaboration meeting #4 (CM4) took place on the 20^{th} September at Strathclyde University, at the start of term for some Scottish universities but before the start of term for the majority of those involved. The meeting included the ITRF PA1 12-month progress review, and a concise action list was prepared that has allowed the 12 month progress report to be finalised.

CM4 was a full day event with time set aside to develop the future plan for work post September 2024. The LhARA/ITRF project team submitted a bid to Infrastructure Fund Wave 4 for £21.5M, for a second Preliminary Activity (PA2). The bid was updated bring out the current level of commitment of the various LhARA collaborators to the project. The updated bid document was passed by the Visions Panel to the STFC Science Board for further review. The timing of this application is such that, if successful, funds will be in place to dovetail with the end of current (PA1) funding. PA2 will include a 'Proof of Principle' Radiobiology experiment, demonstrating the LhARA concept.

1.2 WP1.2 - Laser-driven ion source

1.2.1 Overview of recent progress in WP1.2

WP1.2 has been designed to develop and test the technology required to deliver the laser-driven ion-source for LhARA to serve the ITRF. To address this, WP1.2 has successfully established an active collaboration between all the major laser-driven ion source groups in the UK, including the University of Strathclyde, Queen's University Belfast, Lancaster University, Imperial College London, and the STFC Central Laser Facility. The collaboration is working effectively, with regular meetings and cross-institute collaborative projects. The funding from the ITRF has enabled increased staff effort at the partner institutes and is allowing excellent progress to be made.

The first milestone, M2.1, is to investigate and optimise a proton source driven by 100+ TW laser systems, using hydrodynamic and kinetic simulations. Led by collaborators at Lancaster University, state-of-the-art full 3D particle-in-cell simulations relevant to modelling the SCAPA laser and the proposed LhARA facility have been performed. The target front surface density profile has been varied, showing clearly that a gentle gradient enhances coupling and ion source output. Output from the preliminary simulations has already been shared with other work packages, particularly WP1.6, to allow more realistic beam parameters to be used in simulations of the beamlines. More details will be given in subsection 1.2.2.

The second milestone, M2.2, is to perform the first ion source experiments and simulations for the SCAPA facility at the University of Strathclyde. SCAPA is a key infrastructure for WP1.2, enabling experiments nearly at the baseline LhARA specification, and therefore these initial experiments are directly relevant to de-risking the ion source project. Following a design phase in the first 6 months, the subsequent 6 months has seen the first beam time on SCAPA. This is an important first step and has resulted in a data set for benchmarking simulations and to support the development of high repetition-rate targetry and diagnostics aimed specifically at the requirements of LhARA. Further information is given in subsection 1.2.3.

In addition, experiments have begun using the high repetition rate Zhi laser at Imperial College London to focus on targetry and technical issues related to high repetition rate. As described in subsection 1.2.4, the experimental chamber has been prepared and the laser beamline is being readied to deliver the compressed,

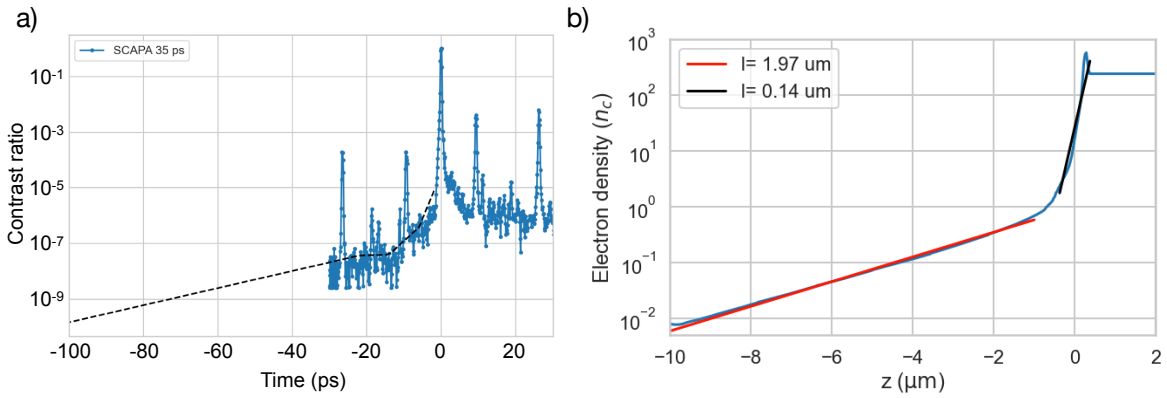

Figure 2: a) Laser contrast curve for the SCAPA laser (blue), and input to FLASH code (dashed black). The larger pre-pulses near -10 and -28 ps are measurement artefacts. b) Predicted axial density profile on the front surface of the target. A typical double exponential scale is shown to form during the pre-pulse driven ablation. The initial target front surface was at $z = 0\,\mu\mathrm{m}$.

femtosecond beam to target. The first experiments irradiating tape targets at $> 10\,\mathrm{Hz}$ have begun, building a platform for the next 12 months of intensive data-taking.

1.2.2 Update on Simulations

Hydrodynamic simulation of the laser pulse

A well known feature of laser-driven ion sources is sensitivity to the laser pre-pulse, which here refers to any laser energy arriving at the target before the high energy, high intensity main pulse. The ratio of the energy in the pre-pulse to the energy of the main pulse, known as the laser contrast, for the SCAPA laser system is shown in figure 2a. Although modern laser systems use numerous advanced techniques to minimise the contrast, the wavelength-scale focal spot typically results in significant target ionisation and heating picoseconds to nanoseconds before the main pulse. This results in ablation of the front surface, causing a shockwave to be driven into the target and a plasma plume to be ejected away from the target. When the high intensity main pulse arrives, it has to travel through the plasma plume up to the dense part of the target, and therefore the properties of the plasma plume, or pre-plasma, often dominate the laser absorption properties, and therefore also the characteristics of the ensuing laser-driven ion source.

Simulating the laser pre-pulse is therefore an important part of the modelling stack, and can be used to determine the initial conditions of Particle-in-Cell simulations of the high intensity pulse interaction. Therefore, the FLASH code [28] has been used to estimate the influence of the laser pre-pulse. This code has been widely used in the high energy density physics community for this application. The code was run using 2D cylindrical geometry and modelled the pre-pulse absorption using an inverse bremmstrahlung heating model based on ray tracing. Heat conduction and energy exchange between electrons and ions are based on the Lee-More model. An example density profile at the centre of the laser axis for the SCAPA laser contrast is shown in figure 2b. The simulation model can easily be extended to different irradiation or target conditions. In the next 6 months, these results will be integrated into the Particle-In-Cell modelling to investigate benchmarking of the SCAPA experiments and to aid optimisation studies for the final LhARA design.

High fidelity 3D Particle-in-Cell simulations

We have conducted three-dimensional (3D) Particle-In-Cell (PIC) simulations exploring the interaction of the SCAPA Ti:sapphire laser (laser wavelength $\lambda_0 = 800\,\mathrm{nm}$) with aluminium foils $6\,\mu\mathrm{m}$ thick. We performed

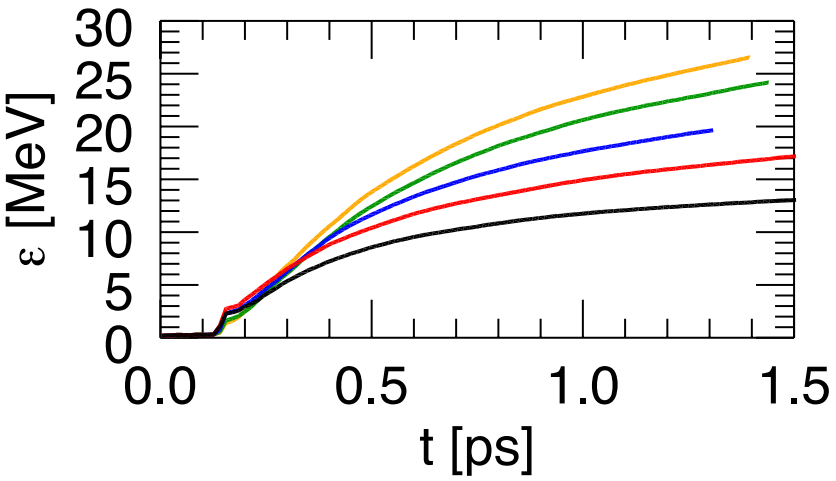

Figure 3: Evolution of the proton cutoff energy for $L_g = 0.08$ (black), 0.3 (red), 0.5 (blue), 0.75 (green) and 1 (yellow) μm and laser $a_0 = 21.60$.

simulations considering laser intensities of $9 \times 10^{20}\,\mathrm{W/cm^2}$ and $9.97 \times 10^{20}\,\mathrm{W/cm^2}$ for normalised vector potentials $a_0 = 20.52$ and 21.60 respectively. The p-polarised pulses were focused on the target to a spot size w_0 of $1.5\,\mu\mathrm{m}$ and had a FWHM pulse duration of 25 fs. The target was modelled as a pre-formed plasma composed of Al^{3+} ions and electrons with density $70\,n_c \sim 10^{23}\,\mathrm{cm^{-3}}$ (here n_c is the critical density corresponding to the laser frequency). To explore the presence of a pre-plasma, the front of the target was modelled following a hyperbolic tangent density profile with the parameter L_g determining the pre-plasma scale-length. On the back of the target, a thin layer of H^+ ions was inserted to mimic contaminants naturally present on the back surface of solid targets.

We carried out simulations considering values of L_g in the range $0.08 - 1\,\mu\mathrm{m}$. Here, $L_g = 0.08\,\mu\mathrm{m}$ corresponds to an almost abrupt plasma-to-vacuum transition and highest laser contrast. Figure 3 shows the evolution of the proton cutoff energy for different values of L_g and $a_0 = 21.60$. In the case of an almost abrupt plasma-to-vacuum transition, protons reach a maximum energy below $15\,\mathrm{MeV}$. Thus much thinner targets would be necessary to meet LhARA requirements. However, a short scale-length pre-plasma results in increased proton maximum energy beyond $15\,\mathrm{MeV}$. The proton cutoff energy increases approximately linearly with larger pre-plasma scale-length values within the tested range. Increasing the proton cutoff energy well beyond the proton energy desired value of $15\,\mathrm{MeV}$ is preferable because it leads to a larger charge in the baseline capture energy interval of $14.5 - 15.5\,\mathrm{MeV}$. A long scale-length pre-plasma also seems to be beneficial to achieve proton beams with better spectral properties. Figure 4 shows the angularly resolved proton spectra at saturation for the case of an almost abrupt plasma-to-vacuum transition ($L_g = 0.08\,\mu\mathrm{m}$) and the longest value of L_g modelled. In the latter case, the beam appears not only to be more energetic but also more collimated.

We note that these simulations represent only an initial step to understand the effect of a pre-plasma in front of the target. The pre-plasma is modelled in an idealistic way with a very smooth density profile and one scale-length. The bulk of the target is unperturbed. In reality, the formation of a pre-plasma by either the laser pedestal or a customised pre-pulse will involve the generation of a shock wave which travels through the target modifying its characteristics. Hydrodynamic simulations are thus necessary to evaluate these effects and provide more detailed information of the pre-plasma.

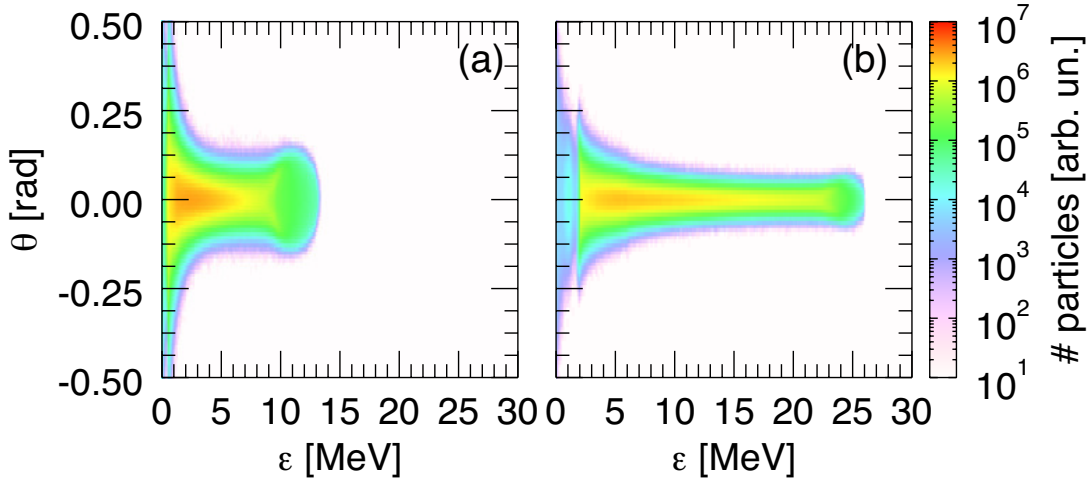

Figure 4: Proton spectrum at saturation for $L_g = 0.08\,\mu\mathrm{m}$ (a) and $1\,\mu\mathrm{m}$ (b). In these simulations $a_0 = 21.60$.

1.2.3 Update on experimental development at Strathclyde

During this 6-month period substantial progress has been made at Strathclyde in key areas related to the LhARA programme covering diagnostic development, beamline development, data analysis and handling, culminating in the delivery of the first experimental beamtime for LhARA on SCAPA. The progress made in these areas are detailed below.

Diagnostic development and targetry

Diagnostics:

In the first 12 months significant progress has been made in the development of diagnostics related to the objectives of WP1.2. We have continued the development of a version of a proton beam imaging spectrometer, called PROBIES [29], as previously reported [30]. PROBIES enables proton beam spatial profiling and energy spectrum analysis at the multi-Hz source repetition rates required for LhARA. PROBIES was used as a primary diagnostic on a first LhARA experimental campaign to characterise high repetition rate laser-driven proton acceleration and to further explore its use under such conditions. Notably, we have achieved a series of measurements investigating the diagnostic lifetime over a number of full power laser-solid interactions (>100 shots), in order to determine its response under high repetition rate conditions. Furthermore, updated versions of this diagnostic have also been manufactured and tested. Updates include alterations to the overall size of the diagnostic and improvements in its energy resolution. We have also made significant progress in the development of algorithms for the deconvolution and analysis of this diagnostic. The process for extracting data is now semi-automated, enabling faster deconvolution of the proton signal. Further development is required for rapid analysis at repetition rates >1 Hz. The next key steps in the development of this diagnostic involve both calibrating the chosen scintillator layer, to measure the number of protons, and testing alternative scintillating materials, which may be more responsive to protons compared to other background ionising radiation produced in the interaction (i.e. electrons, x-ray etc). Calibration will involve the employment of the PROBIES at the MC40 Cyclotron Facility, at the University of Birmingham, planned for late 2023.

Further to the PROBIES, we have also added a Thomson parabola ion spectrometer to our ion source development setup, within the SCAPA facility. This enables both comparative measurements of the proton energy spectrum (at a higher energy resolution) and measurement of the energy spectra of heavier ion species accelerated during the interaction. As this is a well-established measurement technique, it gives confidence in the

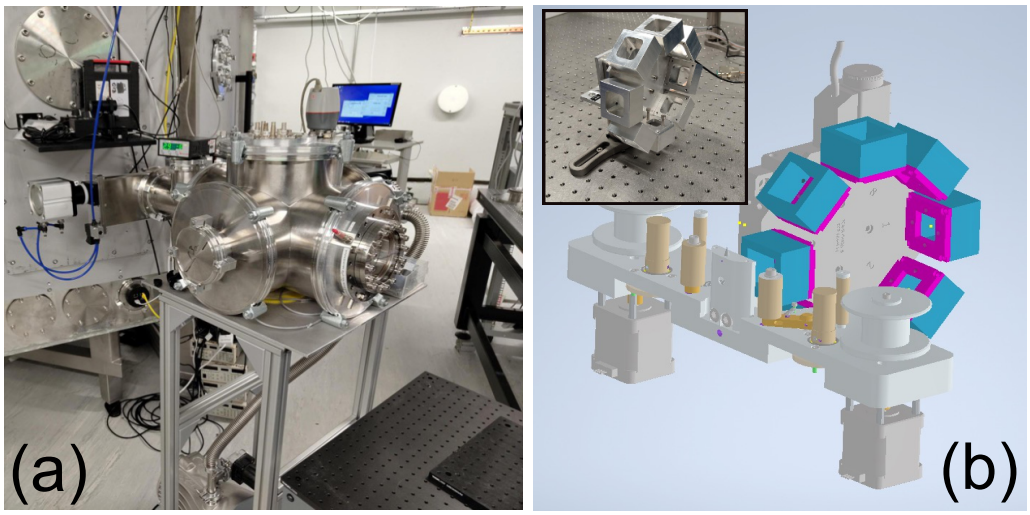

Figure 5: Photographs of (a) the external chamber added to setup to house the Thomson parabola ion spectrometer and (b) the radiochromic film stack system developed to aid in the characterisation of the proton source.

characterisation of the ion source and aids in the development of the PROBIES diagnostic through comparison of proton measurements. The implementation of the Thomson parabola has involved the addition of a new external chamber linked to our main interaction chamber (see figure 5 and the manufacture of custom parts to mount the high repetition rate detector (microchannel plate detector). Furthermore, this setup was designed to be aligned along the normal axis of the interaction, to enable accurate measurement of ions generated by the TNSA mechanism. The setup was successfully employed in the LhARA experimental campaign, enabling the first characterisation measurements of the ions generated from source. Moving forward, we plan to increase the size of this external chamber to ease alignment of the ion spectrometer and, possibly, also to add further diagnostics. In addition, we plan to test alternative detectors in conjunction with this ion spectrometer, in order to relax the restrictions of using a microchannel plate. In parallel with this development, we have made significant progress in the development of analysis algorithms to reconstruct particle energy spectra from this diagnostic at the repetition rate of the laser system.

In addition to the diagnostics for characterising proton acceleration described above, we have also developed a radiochromic film stack system. This has been designed to allow for 8 shots per pump down cycle (as the diagnostic is single use), with the primary use being to give comparable data to PROBIES, enabling cross-calibration. This system has been designed to operate in conjunction with the tape drive targetry system.

Further to the previous report [30], the progress reported above represents significant progress in the development and employment of diagnostics to measure the proton and ion beam properties accurately at high repetition rate. The initial experimental results have yielded encouraging results and providing valuable insights related to the objectives of WP1.2.

Targetry:

During this review period, we have continued the use of a custom tape-drive system for generating laser-driven protons and ions, as introduced in the previous report [30]. We have again successfully employed this targetry system on an experiment within the SCAPA facility, with ≈2000 shots conducted during the experiment, providing detailed parameter scans and a wealth of data for analysis. In the past [30], the design of the tape drive restricted the angle at which the laser could be directed onto the target to $\lesssim 15°$. Over the reporting period

a tape drive modified to increase the limit on the angle of incidence to $\approx 30^{\circ}$ has been tested (see figure 6). To date, experiments employing this system have been conducted without any serious electromagnetic pulse (EMP) issues, however, to further mitigate any possible EMP issues we have now incorporated plastic isolation posts in the mounting of this system. Further testing of this targetry system within this review period has provided further confidence in the suitability of this system to reach multi-Hz repetition rates through rapid target replacement and high alignment stability.

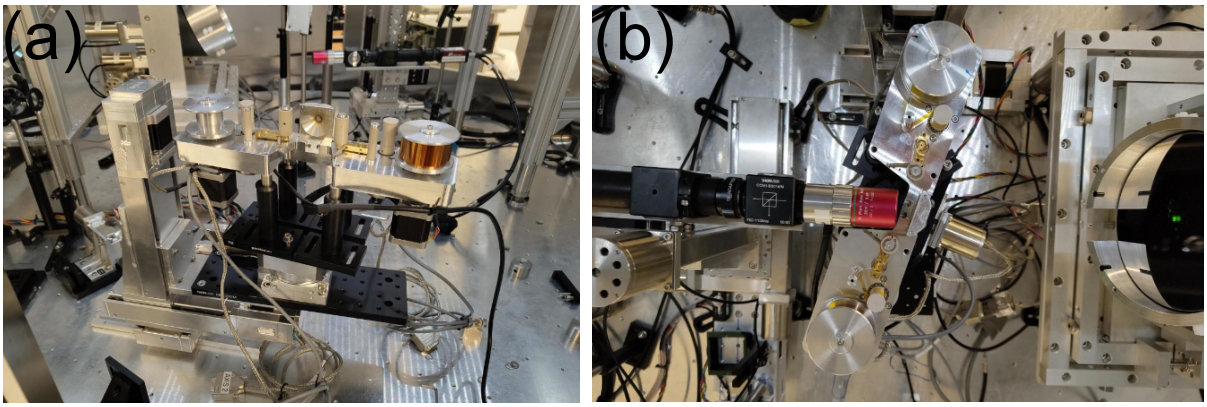

Figure 6: Photographs of the updated tape drive targetry system, with (a) displaying its integration with our target movement drives, and (b) within our source development setup.

Update on experimental beamline and design

Since the previous report, our ion source development setup within the SCAPA facility, used for investigation relating to the objectives of WP1.2, has progressed to a semi-permanent state, with a fixed beamline configuration and permanently setup diagnostics. This will aid in reducing the time needed to move from one setup to the next and help to improve the stability, reliability and overall quality of both the ion source and the diagnostics employed to characterise it.

In addition, we have begun the development and setup of two new optical components linked to the main beamline; a pre-plasma generator and a transverse optical probe (see figure 7). Both are formed from a small sample of the main interaction beam and are guided to a compact breadboard setup used for probe timing and pre-plasma generator energy tuning, enabling this setup to be easier to add to the main interaction chamber. The build of each component is underway, with commissioning planned for late 2023.

Over the reporting period we have also begun the commissioning of a double plasma mirror system within the SCAPA facility. Such a system is employed to improve the temporal-intensity contrast of the laser pulse and will enable investigation of the interaction of high-intensity laser pulses with ultra-thin nm-scale targety.

Finally, during the previous experimental campaign we have identified numerous improvements to be made to the experimental design. These include alterations to the focal spot imaging system, based on achieved improvements to the focal spot quality, and incorporation with the upgraded tape drive targety system. Progress is underway regrading the identified improvements, with the aim of accomplishing these prior to future experimental beamtime.

Data capture and high repetition rate operations

Significant progress has been made in the previous 12 months on data handling and control for experiments on SCAPA and WP1.2. We developed a new version of the *DARB* software that is used on SCAPA to capture and structure experimental data. This update increases data capture rates to 1 Hz, which enables us to collect more

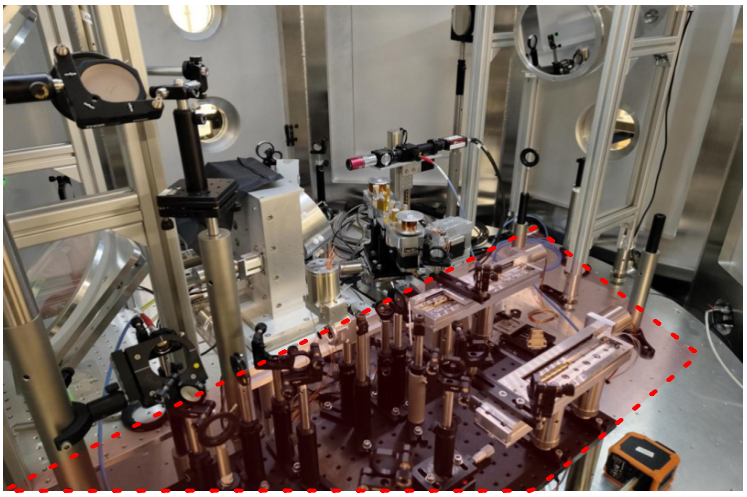

Figure 7: Photograph showing the transverse optical probe timing system and pre-plasma generator energy tuning system, both contained on a compact breadboard (highlighted in red).

detailed data from experiments. The initial testing of these updates were highlighted in the 6-month report [30]. Over the past six months, this system has been deployed to acquire data at up to 1 Hz on SCAPA. Through this testing, new features were identified and added to improve performance.

In addition to the data capture software, further developments have been made to facilitate online data analysis via the *LPI-Py* software. These modifications include features for the live creation of a searchable database of experimental data, live dashboarding capabilities and the construction of basic analysis tools for proton and ion acceleration. The *LPI-Py* software was applied on the most recent SCAPA experiment and has now been demonstrated to enable online data analysis at up to 1 Hz.

As a consequence of delivering these developments, R. Gray (Strathclyde) was invited to give a seminar on *LPI-Py* at the Central Laser Facility. R. Gray is engaging on a data-management workshop for the EPAC facility. These efforts are a key additional output related to the creation of the tools necessary to meet the requirements of LhARA.

First experimental beamtime using SCAPA

In the summer of 2023, the first dedicated beamtime on SCAPA for the LhARA programme was completed. This was a short period of access consisting of 1 week of setup and 1 week of data capture. The objectives of the experiment were to:

1. Perform key parameter scans in laser energy, pulse duration and spot size, measuring the proton and ion energy spectrum at high repetition rate;
2. Characterise the target debris production at high repetition rate; and
3. Continue testing new diagnostic techniques for the proton beam profile, spectrum and for debris production.

The general beamline and diagnostic setup of this experiment is detailed above. For the majority of shots the target was a 25 μm kapton tape which enabled high repetition rate operations up to 1 Hz. The laser parameters were varied as part of a number of detailed parameter scans including 2D scans of the laser energy and focus, laser pulse duration, and a source stability scan. The highest intensity configuration of the laser during the run was an energy 6.5 J, pulse duration of 27 fs, and spot size on the order of 3 μm in diameter giving a peak intensity (considering the measured throughput and encircled energy) of up to 3×10^{21} W/cm^2.

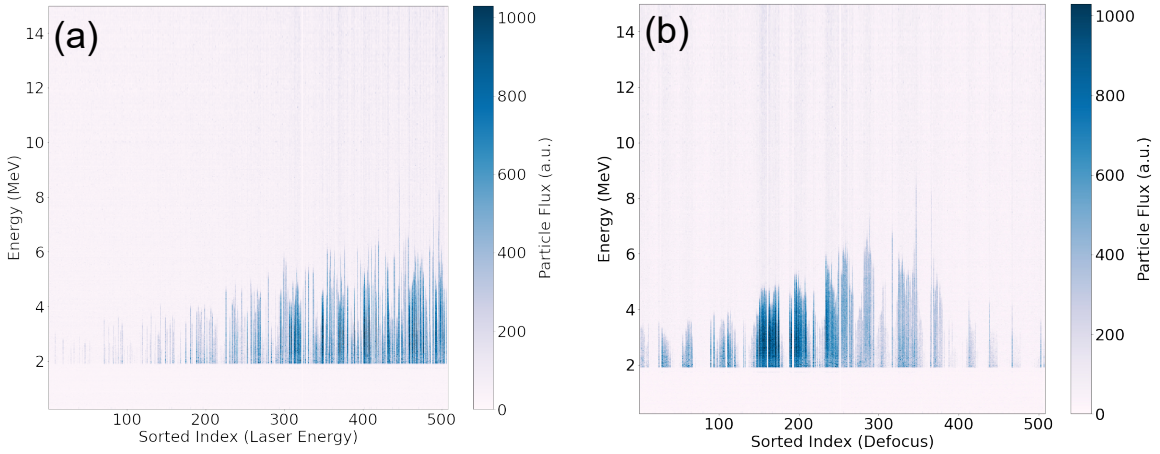

Figure 8: Heatmap of proton spectra measured using Thomson parabola spectrometer as a function of (a) incident laser energy, (b) laser defocus.

The beamtime was delivered on schedule and we successfully completed each of these objectives. Some indicative data from approximately 2000 shots taken during the run are presented here. In figure 8(a), the proton spectrum, measured using a Thomson parabola spectrometer, is shown as a function of the laser energy across approximately 500 shots. The x-axis here is a sorted index of energy in order to give a uniform mapping for the heatmap plot. The two most salient points from this data are the obvious scaling of the flux and the maximum proton energy with laser energy. Although there is shot-to-shot noise in the data, the variations seen in the maximum proton energy are primarily a result of changes in other parameters (such as the laser focus) which occurred at the same time. In the current arrangement the maximum energy observed was slightly greater than 8 MeV, a higher end-point energy is required for LhARA. Future plans to increase the maximum proton energy to $>$15 MeV are detailed in the next section, but target thickness and pre-plasma scale length are two key parameters that will support further optimisation. A similar plot is shown in figure 8(b) for the maximum energy as a function of laser focus. Taken together, the maximum proton energy is optimised for the highest laser energy and near the best focus.

From the measured proton spectrum it is possible to extract the spectral cutoff energy (i.e. the maximum proton energy measured). In figure 9(a-d) the measured cutoff energy is shown as a function of the laser energy, defocus and pulse duration. Typically, a 2D data scan was performed where two of the laser parameters were varied together. The second parameter that is being changed as part of these data scans is indicated in the colour bar. This data is a clear visualisation of the key dependencies of the TNSA ion acceleration mechanism. In figure 9(a), scaling with laser energy is shown to be approximately linear and, as shown before, the maximum energy also strongly depends on the laser focal position. For clarity, and for comparison to the LhARA baseline design, the effective laser power is indicated by red dashed lines. Alternative views of the defocus dependence are shown in figure 9(b-c). In figure 9(d) the dependence of the maximum proton energy with pulse duration is shown, with the laser focal position indicated on the colour bar. The laser energy is fixed for this data scan at around 6.5 J. These measurements indicate that there is no significant change in the proton maximum energy over an 8-fold increase in the pulse duration. The strongest dependencies identified to date are therefore the laser energy and focus. Thus, in a future laser system, emphasis should be placed on achieving high energy on target and a small, optimised (i.e high encircled energy) focal spot. Improving the laser power (and intensity) by reducing the laser pulse duration is not an optimal route to increase maximum proton energy. These results are consistent with previous measurements of TNSA which determined that it is the fast electron number density

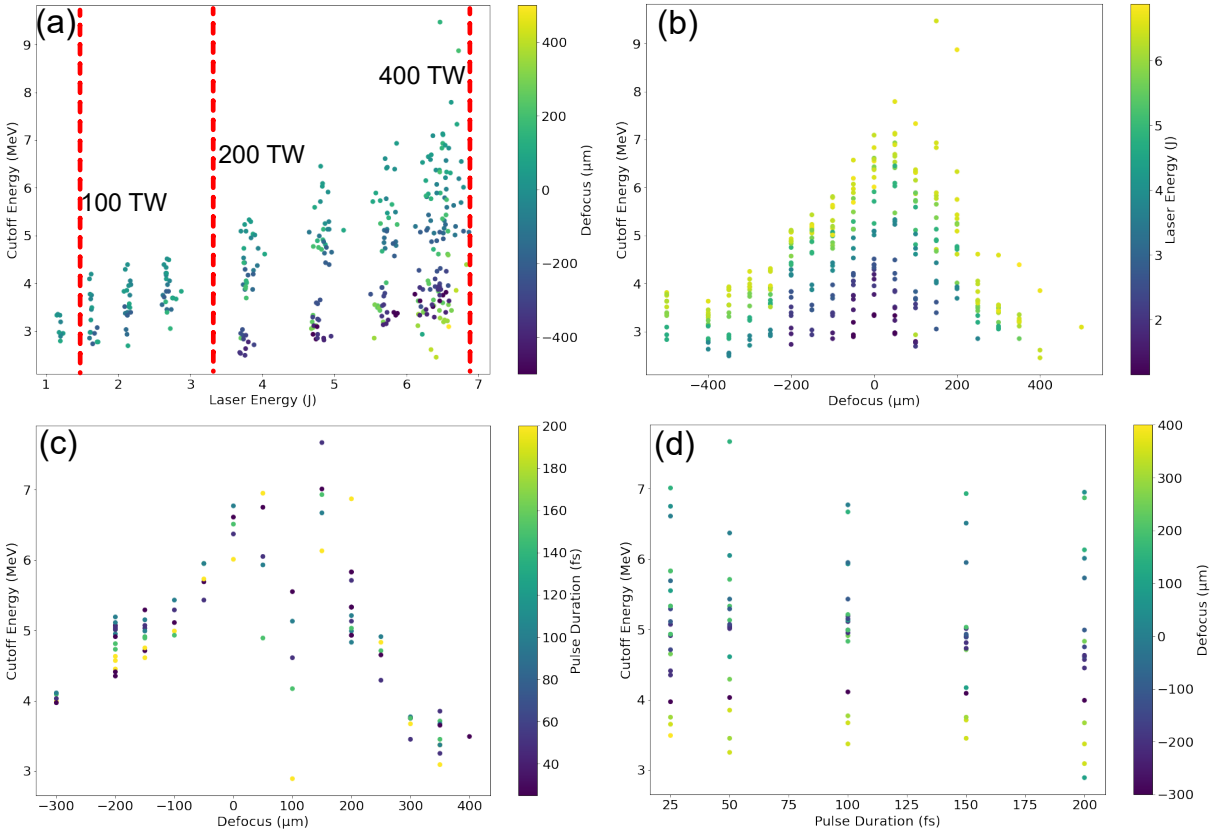

Figure 9: Scatter plots of maximum proton energy as a function of (a) laser defocus and laser energy (b) laser defocus and pulse duration (c) pulse duration and laser defocus.

and the temperature of the fast electron population which most strongly define the sheath field at the target rear, which ultimately accelerates the ions. The fast electron number is closely related to the initial laser energy and the fractional absorption into the target. The fast electron temperature scales with the laser intensity, which scales as the square of the focal spot radius. The result of further analysis into these scalings and comparable results for carbon-ion acceleration will be included in future reports.

At this stage in the programme we have not had the opportunity to investigate the scaling of the maximum proton energy with target thickness and with the pre-plasma scalelength. Previous literature in this area indicates that optimising both of these parameters (along side the laser parameters) can strongly influence the maximum proton energy.

Debris and beamline lifetime issues

An important insight gained from the first dedicated LhARA experiment was the measurement of the lifetime of key optics in the beamline. All of the major optics in the system are rated for a laser fluence above what SCAPA is capable of delivering and thus should not be damaged. However, during this beamtime, the first time that SCAPA has been operated at maximum power for extended periods, both the coating of the parabola and the pellicle (which protects the parabola from target debris) were beginning to show signs of damage. Whereas the accumulation of damage (degradation of the optical coating) on the parabola was relatively minor and did not significantly impact the energy throughput of the beamline, the damage to the pellicle was significant and rapid. In figure 10(a-c) we show a data scan which was intended to test the stability of the proton source over hundreds of shots. In (a) we show that the spectral stability is initially good, with a cutoff of around

6 MeV. After accumulating >75 full power shots, the proton cutoff energy starts to decrease monatonically. In (b) the proton cutoff energy is plotted and the laser energy is shown in the colour map. The laser energy is stable within <10% across these shots,. Despite this, the proton energy cutoff decreased over 200 shots by as much as 25%. The issue becomes clearer in (c), which shows the cutoff energy using the colour map to show the back-reflected energy (in the second harmonic). The energy reflected from the target is seen to decrease. Investigations into this issue identified that the incident laser energy at full power on to the target was reducing because the pellicle was accumulating laser-burn damage which was reducing its transmission. This issue is not related to the accumulation of target debris as tests, shown in (d), demonstrate both that initial transmission of the pellicle is only 80% and over tens of shots (even without a target in place) it begins to damage at full power. At half power the pellicle can withstand over 1000 shots with no signs of damage. This issue poses a significant challenge to long term operations but is likely to be mitigated by the introduction of higher quality, anti-reflection coated, pellicles. Tests of this type of pellicle will be conducted during the next 6-month period.

In addition to investigations of the beamline lifetime due to laser damage induced over many shots, significant steps were also made towards characterisation of laser debris production. New diagnostic techniques have been developed by the Imperial College team to measure the accumulated debris on a sacrificial mirror in the interaction chamber. Both this diagnostic and standard glass slide 'witness plates' were deployed on the SCAPA run. Surface metrology of the witness plates, supported by target fabrication at the CLF, and detailed data analysis from the active debris diagnostics is ongoing and will be reported within the next 6-month period.

Future developments for SCAPA experiments

As a first set of parameter scans, and as a means to identify key issues not previously considered, the first beamtime on SCAPA dedicated to the LhARA programme was successful in achieving the main objectives and provided highly valuable results that will inform further developments.

In the next 6-month period, we will prepare for and deliver the next LhARA dedicated beamtime on SCAPA. This access period will include 1 week of setup and 3 weeks of data collection. We will implement key changes to the diagnostics and general system operation identified from the previous access period. We will also bring online the optical probe diagnostic and the pre-heater beam capability to measure and control the pre-plasma scale length on the front surface of the target. In order to optimise the proton source further and reach the maximum energy and flux requirements for LhARA, control of the pre-plasma scale length and the target thickness will be essential. These two parameters will be investigated in detail during the next beam time. This pre-plasma control will be extended by implementation of the plasma mirror system which underwent initial testing during the previous 6-months.

A significant development during the next period will be in system monitoring and automation. All of the relevant diagnostics have been tested to operate at up to 1 Hz, the targetry can now be automatically replaced and our data capture and analysis is automated. A final step remains to automate the shot parameter selection via automated control of the laser energy, pulse duration, laser focus and pre-heater energy. Within *LPI-Py* a capability already exists to perform some of these functions. This will be further developed and implemented on SCAPA. These capabilities will also be expanded to include monitoring and operation of other key subsystems (e.g. shutters and translation stages).

1.2.4 Update on experimental development at Imperial College London

Construction of ion source driven by the Zhi laser

Over the last 6 months we have been commissioning a laser-driven ion source driven by the Zhi laser in the Blackett Laboratory, Imperial College London. Collaboration members have been involved both in maintaining the laser system and in the development of the target chamber and associated hardware. The Zhi laser is a home-built 100 Hz Ti:Sapphire laser, delivering pulse energies of up to 100 mJ with pulse lengths of ≈ 40 fs, giving

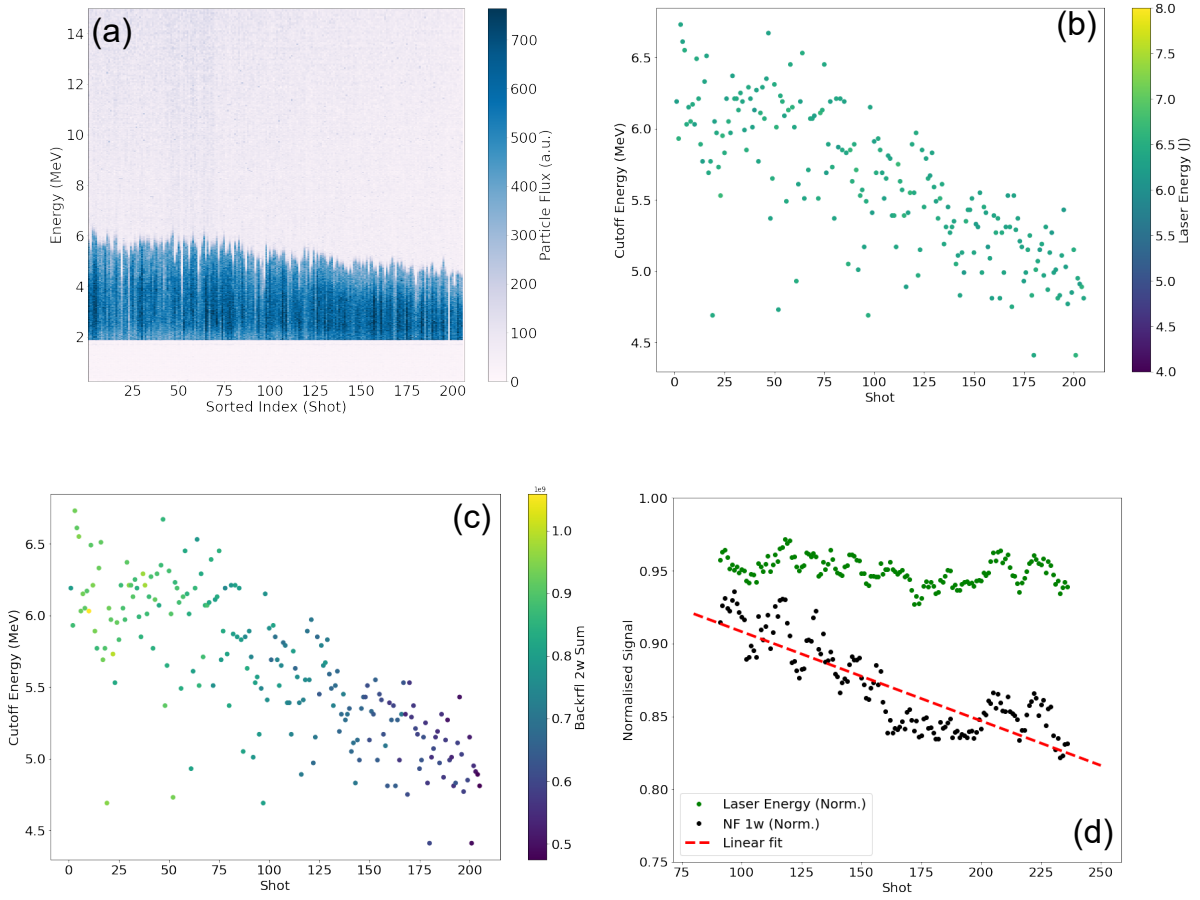

Figure 10: Proton spectra measured as part of a stability scan (a) proton spectra in order of shot number. (b) Cutoff energy as a function of shot number with laser energy in colour map. (c) Cutoff energy as a function of shot number with the total back reflected energy (in the second harmonic) in the colour map. (d) Normalised transmission of the pellicle over a sequence of full power shots.

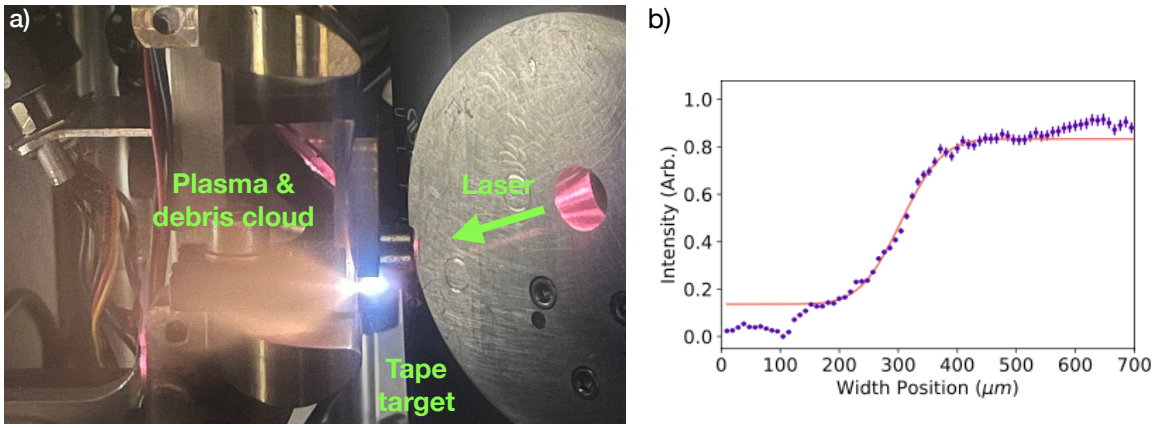

Figure 11: a) Example of an ion source experiment using the Zhi laser. The laser is focused onto the surface of a tape target at 100 Hz, generating ions. b) Preliminary data showing a knife edge measurement of keV x-rays generated from the interaction, indicating a heated region in the order of $\sim 100\mu$m (figure courtesy of J. Hills, MSci thesis, Imperial College London [31]).

a power of ≈ 2.5 TW. Although the laser power and energy are much smaller than required for LhARA, the average power delivery of 1 J/s onto target is comparable to that of the SCAPA facility (≈ 5 J/s), making it a useful in-house facility for doing LhARA related R&D on topics related to high repetition rate and longevity. Furthermore, we have regular access to the Zhi laser, enabling different types of experiments to be performed.

The preparation of the vacuum chamber for the laser-driven ion source has been completed. The chamber is separated from the laser compressor chamber with a gate valve. The beam is then sent down a periscope before being directed onto a protected gold off-axis parabolic mirror (OAP). The OAP focuses the beam upwards, and a sacrificial turning mirror turns the beam back into the horizontal plane and towards the target. The target is a tape target developed independently from the one at SCAPA ([32]) and allows irradiation at 100 Hz, matched to the repetition rate of the laser.

Figure 11a shows an example of a time integrated image of the interaction region, showing a bright plasma emission from the solid target and a cloud of plasma being emitted from the target surface. Although results from the newly commissioned ion diagnostics are not yet ready, preliminary tests measuring the x-rays emitted during irradiation at a lower laser energy (~ 1 mJ) show x-ray energies on the order of 10 keV and a source size $\approx 100\,\mu$m, consistent with predictions.

Experiments at full laser energy are going to begin within the next month. Ions will be measured using a Thomson parabola spectrometer and time-of-flight spectroscopy capable of 100 Hz operation. The reflected laser light will also be measured in 1^{st} and 2^{nd} harmonic, which will help to diagnose the scale length of the plasma on the front surface of the tape. During the next 12 months, the ion source will be characterised and its stability measured shot-to-shot and over 100,000 shots. The debris emission will be measured and its effect on beamline optics will be investigated. Debris capture using magnetic fields will be tested.

Dedicated debris measurements

A serious potential issue for the deployment of a laser-driven ion source at high repetition rate is the production of debris from the target. This debris could potentially affect critical system components, such as optical surfaces. Historically, laser-driven ion sources have been run at low repetition rate or at low laser energies. Therefore, significant effort has not yet been invested on the mitigation of the issue. However, the combination of high repetition rate, high laser energy and continuous operation envisioned for the LhARA means that this

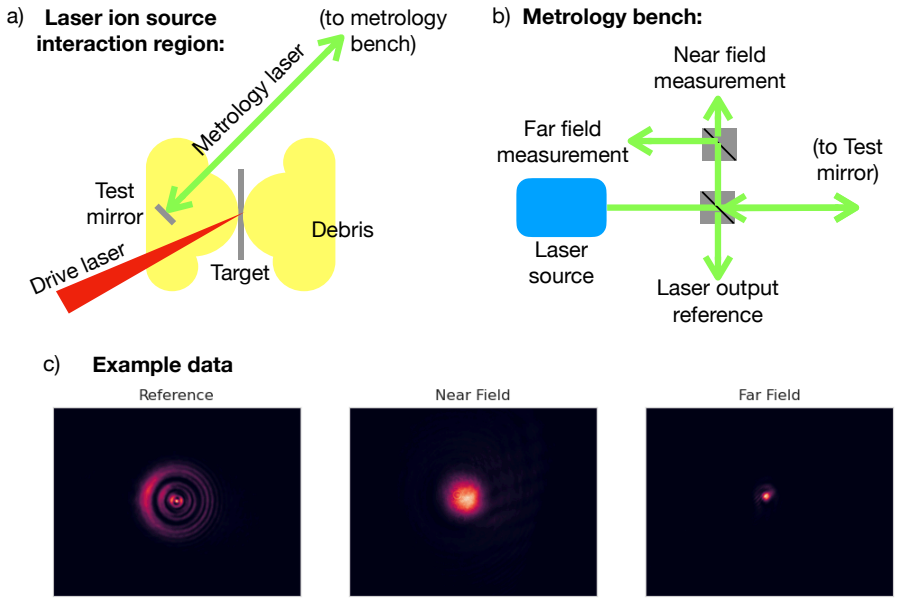

Figure 12: Schematic view of debris monitor a) in chamber and b) on the metrology bench. The test mirror is placed near the debris generating ion source. The quality of the mirror is measured using the metrology laser, which measures both the spatially resolved optical reflectivity (near field, imaged onto the test mirror) and also the focusability (far field) of the beam. c) Example data taken on the SCAPA experiment.

issue needs to be addressed. This requires:

1. The development of techniques to measure debris and its effect;
2. The measurement of debris in different laser and target configurations to understand the debris characteristics expected for the LhARA ion source; and
3. The investigation of debris mitigation techniques such as novel targetry, debris manipulation by magnetic and electric fields, or debris capture by buffer gas.

In the past 6 months, we have developed a new debris diagnostic aimed at understanding the impact of debris on optical substrates. A schematic of the diagnostic is shown in figures 12a and b. As the test mirror accumulates debris, the reflectivity and focusability of light reflected from the mirror is measured. By observing the trend during the experiment it is possible to measure the impact of the debris on the optical surface. In the future, data from this diagnostic will be used to predict the lifetime of the optical beamline delivering the high-power drive laser, and allow quantitative predictions of the impact on the laser-driven ion source. The first test of the diagnostic was carried out during the SCAPA experiments described above (section 1.2.3), with some preliminary data shown in figure 12. Further analysis is ongoing, and the diagnostic will continue to be used in both the Zhi and SCAPA experimental campaigns over the next 12 months. The design of further debris diagnostics is ongoing. Debris velocity will be measured using a fast shutter, and the charge state of the debris will be measured using a magnetic deflector. Debris will be measured under a variety of irradiation conditions with the aim of making a quantitative prediction of the debris generation and properties at the LhARA ion source.

1.2.5 Conclusion and brief outlook for next year

We have made significant progress towards out project goals over the first 12 months of this project. Major highlights since the 6-month report [30] include the first beamtime at SCAPA, in which we were able to suc-

cessfully generate proton and carbon beams at 1 Hz and investigate the stability of the source. As an outlook for the next 12 months, we will continue to execute our project plan in all areas. We have 3 weeks of planned beamtime at the SCAPA facility scheduled for early 2024. We will use this time to develop parametric optimisation of the laser ion source and provide a full specification for the laser requirements for LhARA. We will also deliver a report on these experiments for milestone M2.2 in March 2024. High-repetition rate experiments will continue via regular access to the Zhi laser, investigating source stability over 10,000+ shots and testing debris capture methods including magnetic deflection and fast shutters. These will be supported with further numerical simulations of the laser plasma interaction. Specifically, we will perform full scale 3D simulations of the laser source considering a realistic plasma density profile, and investigate the importance of the laser contrast, an important specification for the laser. Further simulations will predict the optimal angle of incidence of the laser onto the target.

1.3 Work package 1.3: Proton and ion capture

The principal task of the Capture Work Package (WP1.3) during PA1 is the detailed design of a standalone Gabor lens test bench to be constructed during the Preconstruction Phase. The test bench will be capable of operating at 2 kV and of being interfaced with an appropriate ion source.

To achieve this, milestones M3.1 and M3.2 were identified for completion within the first 12 months of PA1, and milestone M3.3 due at month 18. As previously reported and with the support of WP1.1 [30], M3.1 has been rescheduled to December 2023 (month 14), with delivery of M3.2 and M3.2 expected to be postponed due to their serial nature.

The cause of such significant delays is external to WP1.3, and represented by top level risk register entry 3: the availability of key specialist staff. As previously highlighted [30], external administration has delayed the start of the PDRA tasked with the numerical simulations and operating the physical apparatus. This post is now occupied from early October 2023, which permits a significant scaling up of activities.

The risk of delaying the programme has been mitigated with a temporary reprofiling of the focus of existing personnel and use of new collaborators, resulting in progress during the reporting period (months 7-12) with the open-source particle-in-cell code WarpX [33, 34]. The advantage of using WarpX is cost effectivenss with an unlimited number of licence seats allowing for team and collaborative work. Our existing results with the commercial VSim [35] software will serve as a benchmark. Progress with WarpX is summarised below.

- Unity runtime scaling with CPU number has been achieved in small scale workstation-based simulations, with significant positive scaling observed for larger scale tests on SCW HPC CPU resources. A reasonable understanding of the current HPC scaling limitations has been obtained, and is a result of the *current* simulation domain decomposition choices and hardware resource allocation.
  In addition, implementation and positive scaling has also been achieved with the significantly-more capable A100 SCW HPC GPU resources which should enable a twenty-fold increase in data production when required (albeit at an increased cost).
- As part of these runtime and scaling tests, small-scale particle ensembles and plasmas have been initialised and allowed to evolve within a simulation environment similar to the experimental apparatus at Swansea University. Studies carried out as part of the simulation programme include:
  - These WarpX simulations have reproduced the previously obtained VSim results [14]. As illustrated in figure 13, there is excellent agreement between analytical model, experiment, VSim simulations, and WarpX simulations, for the single-particle magnetron frequency of a charged particle as the external solenoidal magnetic field is varied.
  - Ideal cylindrical plasmas with densities comparable to that expected of the final plasma lens have been initialised within the simulation environment and permitted to evolve for over 10^6 iterations (time steps) and hundreds of microseconds. Figure 14 illustrates the simulated axial and radial

plasma densities, as initialised and after 75 μs. The unrealistic, uniformly initialised, density distribution evolves into a larger volume with density variations (or plasma waves) present, and most clearly visible in figure 14d. These outcomes are expected due to the initialisation which causes instabilities due to a mismatch between the ideal plasma equilibrium in the vacuum potential and the simplified plasma initial condition used here.
In addition, the position of the plasma column has changed its radial position during the simulation. This behaviour and the subsequent azimuthal, or diocotron, motion, is similar to the previously discussed magnetron motion.

- To confirm the plasma-based diocotron behaviour of the rotational motion, and to ensure its distinction to the single-particle behaviour, the frequency of the rotational motion was investigated as the plasma density changed. This behaviour is presented in figure 15 for two trap configurations (of 100 V and 1 kV applied confining potentials), and compared to a simple analytical model for the expected diocotron frequency.
  Qualitatively, the deviations from the analytical model may be interpreted as resulting from a mismatch between conditions in the simulations and those captured by the simple model. For example, if the space charge in the initialised plasma in the simulations exceeds the confining potential, a deviation from the linear behaviour in the simple model may result as observed in the simulation results for higher plasma densities in figure 15.
  While more work is required to draw accurate conclusions from simulations, this result is an illustration of the sensitivity of the rotational dynamics of plasmas to conditions in the Penning trap which is also readily observed in experiments, thus illustrating the suitability of our approach for validating simulations.
- As previously reported [30], the loading of electrons into a Penning-Malmberg trap was to be studied during this period. To achieve this, the dynamical loading of the trap from a constant current electron source (similar to that often employed within the experimental apparatus at Swansea University) has been simulated, and observations are presented in figure 16. The dynamical loading technique requires time-dependent voltages to be applied to the trap electrodes for a short time (2 μs discussed here) which produces discrete structure within the energy distribution (illustrated in figure 16a) and axial density variations (plasma waves, as illustrated in figure 16c). Following an evolution time, the trapped plasma tends towards an equilibrium with a smoother energy distribution (illustrated in figure 16d) and lower amplitude plasma waves (illustrated in figure 16f).
  This technique enables testing of the WarpX code against dynamical processes which are experimentally reproducible, and establishment of realistic initial conditions for simulation of long-term effects (e.g. seconds).

Thus, in summary, many of the techniques required to simulate the apparatus and plasma have been established on both local and HPC resources. These have resulted in the production of data and its analysis to provide qualitative agreement with the expectations, and understanding of the *current* limitations. With the PDRA available and these foundational aspects complete, progress towards milestones M3.1 and M3.2 is expected to proceed apace.

In addition, contacts and meetings with the wider community have been made, with discussions occurring between several European and UK based colleagues who are currently interested, and are pursuing, alternative strategies for the implementation of a the Gabor-type lens or high voltage plasmas. These will continue.

1.4 Work package 1.4: Real-time dose-deposition profiling

Work Package 4 has two objectives in the current Preliminary Activity phase (PA1) of the project: O4.1 the development of a Geant4 Monte-Carlo simulation component of a forward model; O4.2 the development of

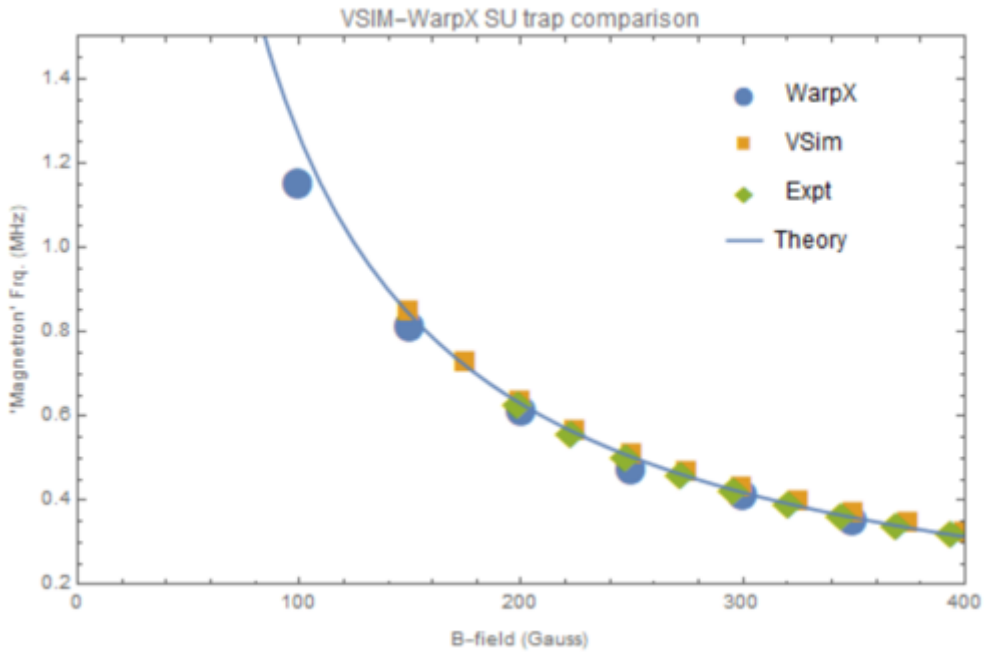

Figure 13: Comparison between previously obtained analytical model, experiment, VSim simulations and the current WarpX simulations. The single-particle magnetron frequency is extracted as the external solenoid magnetic field is varied.

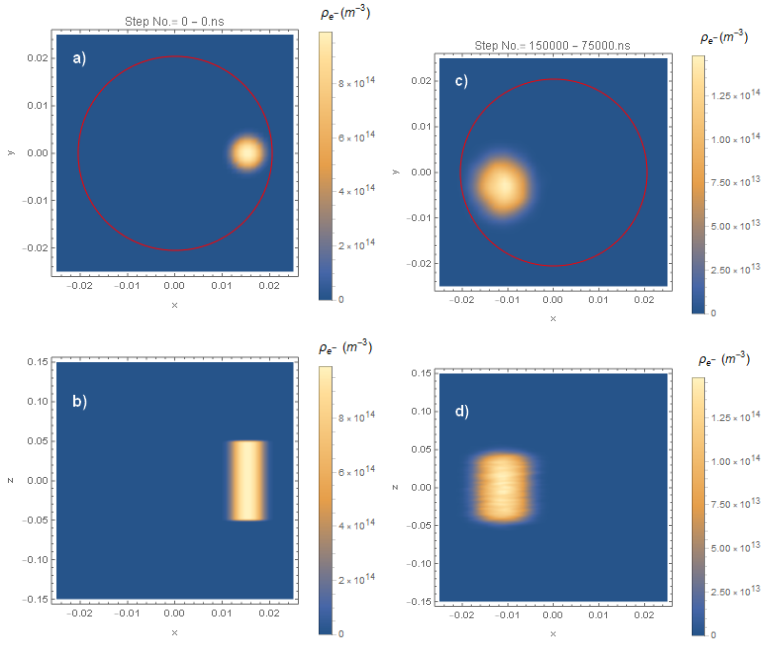

Figure 14: Examples of 2D density profiles for a WarpX simulated plasma within the Swansea apparatus. (a) as initialised radial plasma density, b) as initialised axial plasma density, c) radial plasma density after 75 μs of evolution, d) axial plasma density after 75 μs of evolution.

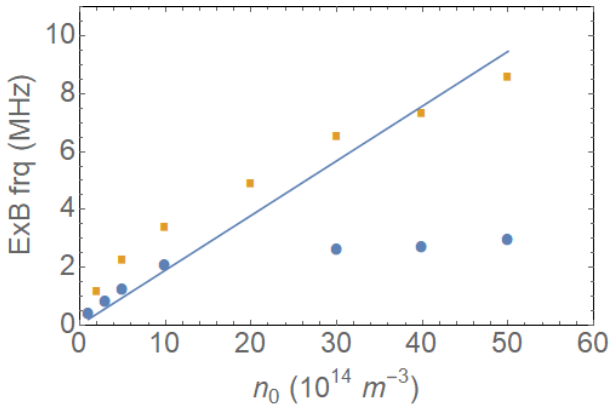

Figure 15: Diocotron frequency as a function of plasma density for 100 V (●) and 1 kV (■) confining potentials, and simple analytical theory (–).

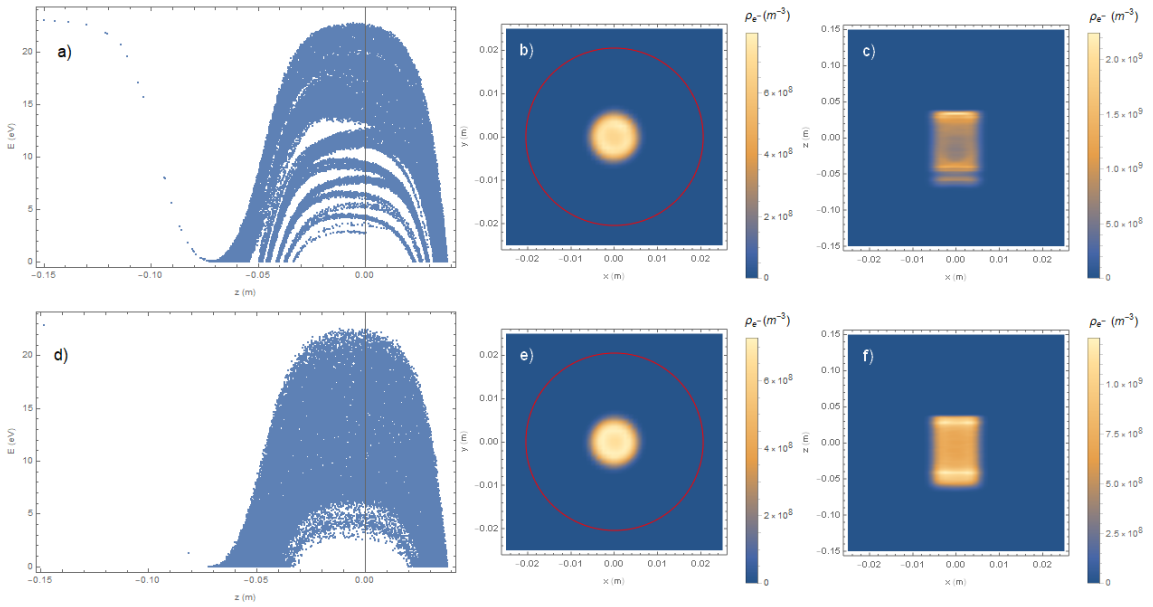

Figure 16: Simulated dynamical loading of a cylindrical Penning-Malmberg trap. (a) macroparticle axial position and energy at early simulation time (2.3 μs). (b) radial density distribution at early simulation time (2.3 μs). (c) axial density distribution at early simulation time (2.3 μs). (d) macroparticle axial position and energy at later simulation time (100 μs). (e) radial density distribution at later simulation time (100 μs). (f) axial density distribution at later simulation time (100 μs).

a K-Wave simulation component of the same forward model. These objectives together enable the principal task for PA1, which is the detailed design – including identification of potential suppliers of components – of an experiment to prove the principle of ion-acoustic dose-profile measurement to be executed during PA2. No researchers were resourced for Work Package 4 in the grant for PA1, the work instead being carried out by research students leveraged from outside the PA1 funding. With reference to the tasks defined in the Gantt chart of table 8 of [36], progress during the current 12-month reporting period is summarised below.

1.4.1 Review

The review of the literature on ion-acoustic dose-profile measurement has been updated since the 6-month review [30], with published papers discussed at the group's biweekly meetings. Overall, encouraging proof-of-principle results have been presented by other groups, indicating detectability of ionacoustic and x-ray-acoustic signals for transient deposition of dose in water, in phantoms and *in vivo*. As expected from first principles, the frequency content of the emitted acoustic waves depends on a combination of radiation pulse duration and the spatial frequency structure in the dose distribution. Groups unable to generate the very short pulses expected from LhARA have deliberately employed ultrasound sensors with a centre frequency (e.g., 350 kHz) much lower than normally used for ultrasound anatomical imaging (e.g., 3-7 MHz). Even sensors centred at 350 kHz, however, tend to edge-detect the a smooth x-ray field (e.g., Zhang et al, 2023 [37]). Superior signal-to-noise ratio and structure is expected from LhARA, although the evidence from the literature is that we can expect ion-energy dependent high-frequency contributions from the Bragg peak region but largely ion-energy independent low-frequency contributions from the plateau region of the dose distribution upstream of the Bragg peak. Extremely broad bandwidth sensors will therefore be required if all features of the dose map are eventually to be reconstructed quantitatively. Our workplan, including signal bandwidth studies and reconstruction algorithm development, remains novel and promising.

1.4.2 Monte Carlo part of the forward model

1.4.2.1 Simulation of current beam line and smart phantom:
As mentioned in the 6-month report [30], a collaboration has been established with Ludwig-Maximillian (LMU) University Munich, with a view to conducting an experiment there to test our SmartPhantom and our own existing acoustic detectors and to validate our simulation. This represents a major, but highly positive departure, from the work plan described in the original proposal. It is now planned to test the SmartPhantom in 2024.

Code was written in Python to generate source data which was confirmed to have the required energy distribution and a flat angular distribution. The proton energy distribution extended to 25 MeV. BDSIM was used to simulate the laser driven LION beamline directed into our SmartPhantom. The LMU beam line consists of a pair of orthogonal quadrupole magnets and a number of collimators. The energy spectrum of protons at the exit window peaked at about 21 MeV with a full width at half maximum (FWHM) of about 1.4 MeV. The beam at this point was asymmetric in diameter with a FWHM of about 0.67 mm in the x direction and a about 0.37 mm in the y direction.

Geant4 was used to simulate particle transport in water within the SmartPhantom in an aluminium box and a Kapton entrance window at the end of a cylindrical air-filled port into the phantom, producing a 3D deposited-energy distribution with a Bragg peak 4 mm from the Kapton window and a beam at the Bragg peak of FWHM diameter about 1.5 mm in the x direction and about 0.9 mm in the y direction. This dose distribution, assumed to be present for about 40 ns, was used as the input to the K-Wave part of the forward model (see below).

As described in the 6-month report [30], four planes of scintillating fibres, an essential part of the SmartPhantom design for the planned validation experiment, were previously incorporated in the Geant4 simulation. Each plane consisted of 66 polystyrene fibres each of length 10 mm, 250 um diameter, with an array pitch of 300 um

and hence a gap between fibres of 50 um, forming a sensitive area of 20 mm $\times$ 20 mm. The simulated energy deposited in this fibre array suggested that up to 5 fibres should generate an optical signal for the above beam. With fibre planes positioned at about 0, 1, 2, and 3 mm from the entrance window, the Bortfeld equation [38] gave a good description of the axial dose-distribution, representing an excellent pulse-specific reference against which to compare the axial profile of the deposited-dose reconstructed from the ionacoustic signal. Prototype scintillating fibre planes have also been successfully constructed to this design, with fibres wound on aluminium frames. Since the 6-month report this construction has been finished. Future work will involve experimental testing of the fibre planes with a proton beam and finally using them in an experiment to validate the simulations with experimental data.

As mentioned in 4.4.1 below, however, K-Wave simulations conducted since the 6-month report have shown that simultaneous ionacoustic and scintillating fibre measurement of the pulse-by-pulse proton dose distribution will not be possible due to the acoustic wave distortion introduced by the fibre planes. Separate scintillating fibre and ionacoustic measurements will therefore need to be conducted in the planned experiment.

Work initiated to explore the possibility of using liquid scintillators in the SmartPhantom, and reconstruction of the dose distribution from multi-view optical cameras, has continued. This is to mitigate the acoustic wave disruption caused by the fibre planes mentioned above, to allow the pulse-by-pulse validation of the ionacoustic method. A liquid scintillator consisting of 2,5 diphenyloxazole and 1,4 (2-methylstyryl)-benzine in a combination of various solvents was identified and shown to be miscible in water. The feasibility of the detecion of the scintillation light is being invstigated using ray-tracing software (for a black anodised inner surface of the phantom having 5% reflectivity, split 80% Lambertian diffuse scattering and 20% specular reflection). Linearity and dynamic range of the CCD camera have been calibrated using a flourescent dye disolved in water. Given this success, work in developing the liquid scintillator reference method will continue.

An MRes Cancer Technology project was run between the Institute of Cancer Research (ICR) and Imperial College to explore an alternative simulation validation experiment that would not require a beamline. This project (completed since the 6-month report) employed the output of the Geant4 simulation to 3D print thresholded versions of the deposited-dose distribution as plastic moulds. The moulds were used to create pigmented gel phantoms in the shapes of outlines of the dose distribution at two threshold values, for a 70 MeV proton beam of 40 ns duration. This kinetic energy was chosen to create a Bragg peak at a depth suitable for imaging with an existing photoacoustic system at the ICR. Each phantom was imaged using one of two available broadband (100 kHz–4 MHz) sensor arrays. A part-circular ring array surrounding the beam was mechanically scanned along the beam axis to explore signals from radially emitted acoustic waves at various axial positions, and a part-spherical cup array was positioned on-axis beyond the Bragg peak to explore signals from acoustic waves emitted down the beam axis from the distal region of the Bragg peak. The signals and reconstructed images of the thresholded dose distribution, were studied in comparison with K-Wave equivalents, for two threshold values (5% and 40% of the global maximum dose at the Bragg peak), providing an alternative validation and allowing further understanding of the overall acoustic signal time-frequency composition to be better understood for sensor elements placed in various locations. In general, it was confirmed that good low-frequency response is necessary for imaging the relatively constant plateau region of the dose distribution upstream of the Bragg peak and good high-frequency response is necessary for reconstructing and localising the Bragg peak. For the kinds of beam diameters expected, the signals detected from radially emitted acoustic waves agreed well with both analytical predictions and simulations, having maximum signal amplitude at a frequency of about 200 kHz. Transducers with bandwidths extending to 100 kHz were able to detect these signals in practice, and images reconstructed from such signals showed excellent agreement between the measured beam diameter and the true beam diameter, as well as good ability to display the constant dose value in the plateau region of the beam. Flaring of the beam diameter towards the Bragg peak was clearly visible in the 3D images reconstructed using the mechanically-scanned ring array. The cup array was able to detect the signal

associated with the on-axis sharp fall-off of the dose distribution distal to the Bragg peak, which was blurred due to the longitudinal resolution of the ring array. It was, however, unable to detect signals upstream of this because the unidirectional on-axis laser illumination originating downstream of the Bragg peak, which was strongly absorbed by the pigmented gel, did not adequately simulate the ionacoustic experiment. To achieve adequate simulation, more omnidirectional diffuse illumination, as employed with the ring array, would be needed. Nevertheless, the results were strongly suggestive that a 4-5 MHz upper frequency response would be sufficient for detecting on-axis signals from and resolving the Bragg peak for 70 MeV proton beams.

1.4.2.2 Updated simulation of LhARA and smart phantom

This was updated as described above. Further updates are expected in preparation for the validation experiment at LMU, particularly to adjust the energy and beamline properties to produce the best acoustic signal detectability using the sensor arrays currently available at the ICR.

1.4.3 K-Wave part of the forward model

1.4.3.1 Simulation of ionacoustic source, propagation and sensing, and design of array configuration for validation experiments

For a preliminary demonstration of the full simulation pipeline, the above 3D deposited-energy distribution was assumed to exist for 40 ns with instantaneous rise and fall. When converted to an acoustic source pressure distribution using a Grüneisen parameter for water, this rate of change of deposited energy then acted as the source in a K-Wave simulation. Convergence tests demonstrated that a K-Wave finite-element mesh of 0.1 mm voxels is sufficient for accurate simulation of the acoustic source and the propagating acoustic wave at this proton energy. Movies of the wave travelling away from the deposited-energy distribution showed wave directions and rates of decay in a loss-less medium (water) qualitatively consistent with a cylindrically-diverging wave along the radial direction upstream of the Bragg peak, and pseudo-spherical divergence from around the Bragg peak, due to the proton beam flaring due to forward and small angle proton scattering. Inward propagating waves were also seen from the boundaries of the deposited-energy distribution, as expected. These phenomena will influence the bandwidth of the acoustic waves and hence of the acoustic sensor array design, and their further study is an important next step. Temporarily, to complete the preliminary test of the full simulation pipeline, an array consisting of 186 acoustic sensor elements each a 1 mm diameter disc, were placed on a hemispherical surface of 16 mm diameter positioned with its centre about 2 mm upstream of the Bragg peak. These provided simulated detected acoustic signals for preliminary testing of several potential dose-map reconstruction algorithms under noiseless conditions (see 4.4 below).

1.4.3.2 Updated simulation of ionacoustic source and development of sensor array specification, as LhARA specifications are developed in other work packages

This update has started, as described in 4.2.1 above. In addition, a matrix sensor array has been defined in the K-Wave simulation, consisting of 1024 square elements with a pitch of 0.3 mm distributed in four banks of eight rows of elements with a missing row between each bank over an elevation aperture of 14 mm, and a single bank of 32 columns of elements with no missing columns over a lateral aperture of 12 mm. The elements have a nominal centre frequency of 3.5 MHz with 60% bandwidth. K-Wave simulations of ionacoustic image reconstruction performance with this matrix array, which will be obtained on loan for the planned experiment using the LION beamline at LMU, are about to begin. This will be the first simulations conducted in the project with sensors of restricted acoustic bandwidth. From the work described in 4.3.1 above, expectations are that it will be able to localise the Bragg peak and the edges of dose distribution, even though its limited low frequency response will be insufficient to detect signals from the upstream plateau region of the beam.

1.4.4 Implementation, simulation evaluation and development of inverse dose-map reconstruction software

1.4.4.1 Direct ionacoustic reconstruction with handling of sensor array configurations

Using the sensors arranged in a hemispherical array (section 4.3.1 above), three image reconstruction methods were evaluated: iterative time reversal, model-based minimisation, and direct back-projection. Iterative time reversal appeared to provide a 3D dose-map reconstruction, the shape of which most closely approximated that of the original deposited-dose distribution, with a shape around the Bragg peak that converged on the correct shape after four iterations. Model-based minimisation required more iterations (greater than 5) and never fully converged in the study so far. Back-projection is a rapid non-iterative method and directly provided a result similar to that of the first iteration of time reversal and arguably superior to the first iteration of the model-based minimisation method. For higher proton energies, all methods failed to produce an adequate representation of the deposited-dose distribution at beam depths upstream of the centre of the hemispherical array, although this was expected as this region is out of the field of view of the hemispherical detector array, and could be corrected by mechanical motion of the array in the final device, or by compromising on resolution for extended field of view using other shapes of array and/or other sizes and number of elements. For proton energies of 20 MeV and lower, the reconstruction provided a good representation of the source deposited energy distribution, even upstream of the Bragg peak. As mentioned above, however, a next step is to explore the effect of restricted acoustic-sensor bandwidth.

K-Wave modelling with four scintillating fibre planes present in the SmartPhantom showed extensive disruption of the acoustic waves and reconstructed acoustic pressure distributions that were far from adequate as a representation of the source pressure distribution, even for the basic task of localising the Bragg peak. As a consequence, the plans for scintillation reference mapping of the deposited dose were altered as described above.

1.4.4.2 Iterative reconstruction methods with model-based priors from 4.2:
This activity is due to start Q2 of 2024.

1.4.4.3 Iterative reconstruction methods with angular dependence of frequency content from 4.2 and 4.3:
This activity is due to start Q4 of 2024.

1.4.4.4 Implementation of various dose-map reconstruction programs on Verasonics system:
This activity is due to start Q2 of 2024.

1.4.5 Additional experimental work

As mentioned in section 4.1.1 above, experimental work not envisaged in the original proposal submitted as a bid for funding, is now planned at LMU. In preparation for this experiment, existing transducer arrays (the matrix array referred to in 4.4.1 above and a GE L9-D) and a 256-channel ultrasound data acquisition system (Verasonics Vantage-256™) and 1024-256 multiplexer have been identified at ICR and their loan agreed for the purpose of the experiment. Discussions are underway with Photosound Ltd, for the hire of a 256-channel low-noise high-impedance preamplifier that will help us to maximise the acoustic signal-to-noise ratio, especially for improving the desired low-frequency performance mentioned above. A computer aided design of the SmartPhantom has now been produced, which will contain three viewing ports, providing interchangeable acoustic access to one radial view of the beam and one downstream on-axis view. The design is shown in Ffigure 17.

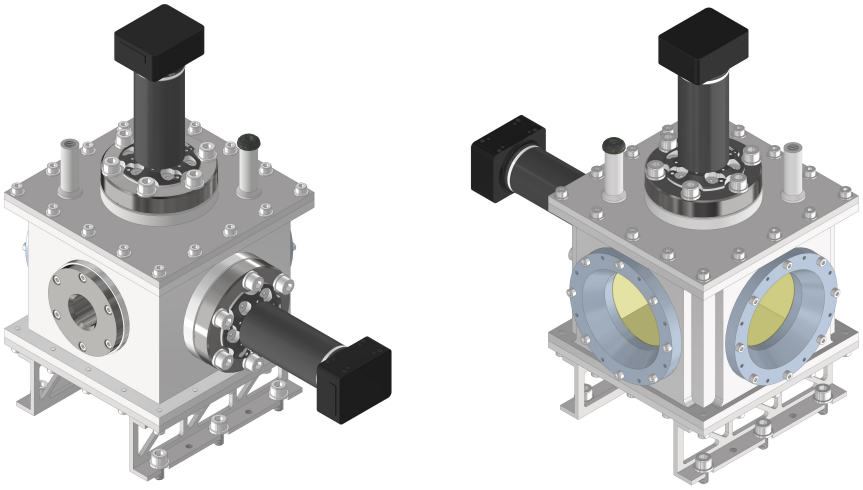

Figure 17: Computer-aided design of the SmartPhantom. Water-based liquid scintillator, which forms the body of the phantom, is contained within an aluminium box. The beam enters through the port shown in the front face of the left-hand image. Two CCD cameras are mounted to view the scintillation light. Acoustic sensors will be mounted such that the tranducers are efficiently coupled to mylar windows, shown in yellow on the right-hand image.

1.5 Work package 1.5: Novel, automated end-station development

1.5.1 Consultation Meetings Update

The report for the first of the series of peer-group consultations to gather input on the specification and design of the end stations for LhARA was completed and included an appendix containing a summary of the conclusions C1–2 and recommendations R1–7 arising from the meeting [39]. The second consultation was held on 19^{th} June 2023 and hosted at the University of Birmingham; it attracted 31 registrants with 14 attending in person. The programme [40] was split into two sessions as per the first meeting, with focus this time being the Stage 1 *in-vitro* endstation—which will be served with a 15 MeV proton beam—and specific attention given to recommendations R1–5 made following the first consultation. Collaborators from within the LhARA/ITRF community presented key talks and the Mary Lyon Centre was introduced by its director, Dr. Sara Wells. Dr. Wells will be invited as an expert to the third consultation meeting which is intended to focus on the *in-vivo* end stations and animal houses, thereby covering recommendations R6–7 from the consultation 1 report.

During the second consultation meeting, lengthy discussions followed each of the morning presentations and the afternoon continued with presentations and discussions on the endstation design and potential radiobiology research programmes. The CERN Yellow Report on the feasibility study for BioLEIR was highlighted as a significant document to be studied [41]. Each of the recommendations R1-5 from consultation 1 was considered and a summary of the discussions for each included in the report for consultation 2. The conclusions from consultation 1 were supplemented with four additions, C3–6 in the report. The first of these is the adoption of "Simple, Robust, Reproducible, and Cheap" (C3) as the mantra for experiments and endstations and therefore, for the rest of the consultation, the Stage 1 *in-vitro* experiments will assume the use of plastic cell dishes (C4). A key point is the requirement of the inclusion of an x-ray source in the facility to allow control samples and low LET comparisons to be made with cultures in both Stage 1 and Stage 2 *in-vitro* endstations (C5). Strong cases were made for temperature, oxygen, and carbon dioxide levels to be controlled such that the integration of cell transport into the endstations and environmental stabilisation must be carefully considered to allow transport of

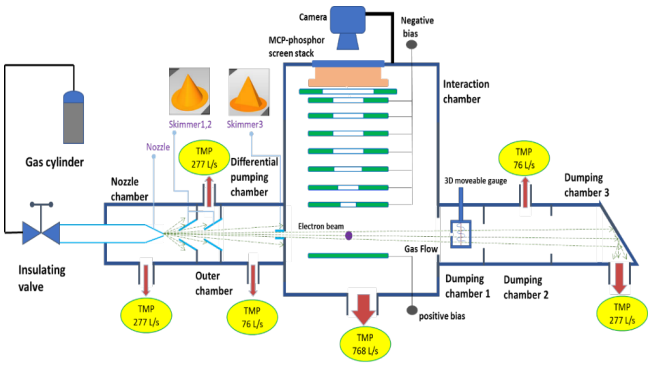

Figure 18: Schematic of the gas jet based ionization beam profile monitor. The beam direction is into the page.

cell samples in the order of minutes (C6).

In early September 2023, a survey was sent to all attendees of consultations 1 and 2 to capture details of potential flagship experiments for the LhARA Stage 1 facility. The survey can be found here [42] and the results will be analysed going forwards. Preparations are being made for consultation 3 to be held in the autumn.

1.5.2 Gas Jet Profiler Measurements

Current techniques for dosimetry typically provide limited information (one-dimensional dose profile or only total dose value), are distructive, provide low spatial resolution, and suffer from slow response times. A complete knowledge of the beam properties delivered to a sample, animal, or patient is essential, so calibration measurements must be taken at regular intervals. Currently there is no method to monitor the beam parameters to high fidelity in 2D during treatment without disturbing the beam. Ionisation chambers and Faraday cups require regular maintenance which includes replacing components followed by recalibration to verify their performance, which is time consuming. The use of current technologies is further complicated by the particular pulse structure to be used in LhARA, where the instantaneous dose rates will cause severe saturation effects in ionisation chambers. The detection of ions produced by the passage of a beam through a gas jet is being developed to overcome these issues.

The QUASAR group is a recognised leader in the use of gas jet technology for characterising charged particle beams [43]. This technology is optimised for use with low-energy electrons and anti-protons as well as for the high luminosity upgrade of the Large Hadron Collider (LHC) at CERN [44, 45]. The system has been tested extensively with a 10 mA, 10 keV electron beam with three different gases: nitrogen, neon and argon. The monitor works by generating a supersonic, low-density gas jet curtain using a bespoke nozzle-skimmer arrangement, see figure 18. The gas jet crosses the beam perpendicular to the direction of travel of the particle beam which ionises the gas molecules. The ions produced can be collected and imaged to generate the beam profile. The gas-jet based ionisation profile is identified and optimised for initial testing as a dosimeter for beams having characteristics similar those of LhARA. The modified gas jet dosimeter was transported to Dalton Cumbrian Facility (DCF), Whitehaven, UK and coupled with one of the beamlines at DCF (see figure19).

The performance of the gas-jet dosimeter was tested for two different ion species, proton (H^{+}) and Carbon (C^{2+}, C^{3+}, C^{4+}, C^{5+}), with beams with energy in the ranges 4–8 MeV and 12–24 MeV at currents in the ranges of between 10-100 nA and 1-100 nA respectively. These benchmarking measurements were conducted with two different gases: nitrogen and argon. The measurements were realised with support from the Faculty Impact Fund (FIF), University of Liverpool with a grant of approximately £15k. Additional support for this experiment was provided by STFC-funded CLASP project JetDose.

Figure 19: Modified gas jet dosimeter coupled with one of the accelerator beamlines at Dalton Cumbrian Facility (DCF).

A new online, non-invasive beam dosimeter that can provide real time beam characterisation and dosimetry with good spatial resolution, requiring no regular maintenance, will be developed on the basis of the findings from the DCF experiment. Simulation studies will underpin the experimental campaigns and help to optimise the overall performance of the monitor. The project will capitalise on the existing infrastructure at the Cockcroft Institute which leads to very significant cost reduction. The monitor will not affect the particle beam properties, thus allowing measurements of dose and profile to be taken whilst the patient is being treated and allowing experimenters or clinicians to be given a detailed view of the 2D beam profile delivered to the sample, animal or patient.

1.5.3 Instrumentation Review

A literature review has identified the few existing techniques which are worth further study for LhARA beam monitoring. There was a recent publication titled "Absolute dosimetry for FLASH proton beam pencil beam scanning radiotherapy" [46] in which the measurement of the pencil proton beam at the CCHMC beamline was reported. CCHMC is equipped with a 250 MeV proton cyclotron (ProBeam, Varian Medical Systems, Palo Alto, CA, USA) that has been upgraded to deliver FLASH irradiations [47].

Calorimetry is a technique used for direct measurement of absorbed dose of a radiation. The technique involves measurement of radiation-induced temperature rise in combination with the accurate knowledge of the beam dependent correction factors to calculate the energy absorbed. The dosimetry was carried out on a proton beam of 250 MeV using the NPL Primary Standard Proton Calorimeter (PSPC) was compared with a set of ionisation chambers to determine the absolute measurement accuracy. The NPL PSPC is a graphite calorimeter with a disk-shaped core composed of a double layer of graphite jackets and mantle. Measurements are performed in a quasi-adiabatic mode of operation, where the jackets are used to shield the core from ambient temperature effects, delivering a temperature measurement accuracy of about 0.1 mK. A set of thermistors are used in the core and the jacket to control the temperature as well as to measure it. It is expected that the NPL PSPC is dose rate independent.

Measurements were carried out at a water-equivalent depth of 5.2 gcm^{-2} by placing the graphite build-up plates in front of the measurement equipment. Figure 20 shows the accuracy of the calorimeter relative to the ionisation chambers in terms of the ratio of dose measured by the calorimeter to the dose measured by three specific ionisation chambers: PTW Roos, PTW advance Markus, and IBA PPC05. Comparisons are

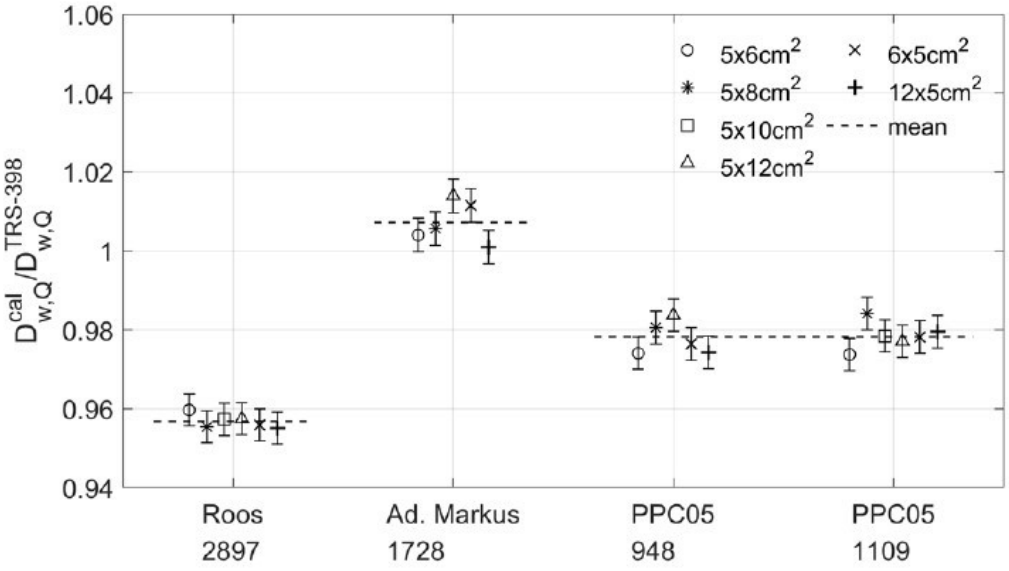

Figure 20: Ratio between the dose determined by the NPL PSPC and the dose derived from ionisation chambers for the various fields tested. Dashed lines represent the mean ratio value for each ionisation chamber type and the error bars represent type A standard uncertainties [46].

reported for six rectangular vertical scanning fields of 5×6, 5×8, 5×10, 5×12, 6×5 and 12×5 cm^2. Monte Carlo simulations using TOPAS [48] and FLUKA [49] codes were adopted for accurate modelling of beam parameters. The simulations were bench marked using a large-area ionisation chamber (IBA StingRay) using "Integrated Dose Depth" (IDD), see figure 21.

Observations:

The calorimeter is shown to be an accurate technology for the measurement of the dose rate with overall uncertainty of 0.9% (1σ), in line with the recommendations for reference dosimetry for effective radiotherapy treatments. The uncertainty is expected to be twice as good as that of the ionisation chambers. The response isreported to be dose-rate independent in contrast to the ionisation chamber where ion recombination effects need to be accounted for. The article also emphasises that the measurement technique is relatively complex

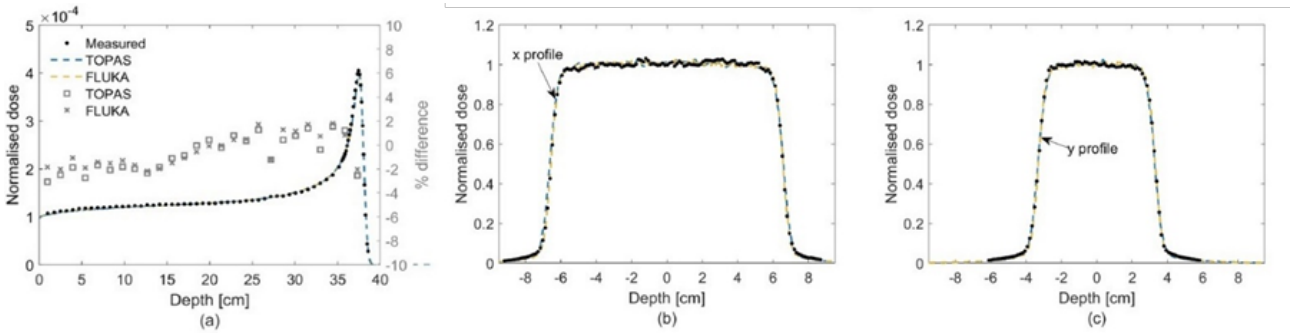

Figure 21: Measured and simulated dose distributions for the field 12×5 cm^2. Solid circles represent the measured data, dashed curves represent the simulated data, and open squares and crosses the percentage difference between simulated and measured data using TOPAS and FLUKA, respectively [46].

compared with that for ionisation chambers. However, it can be employed to test the accuracy and precision of the ionisation chambers to assess their feasibility for UHDR proton beams. It is currently pitched as the calibration and quality assurance tool for ionisation chambers.

The article titled "*in-vivo* dosimetry in external beam radiotherapy" highlights currently available techniques for *in-vivo* dosimetry in external beam radiotherapy (EBRT) [50]. *in-vivo* dosimetry means the measurement of the radiation dose received by the patient during treatment. Presently, *in-vivo* dosimetry (IVD) does not imply that the detector should be placed 'within the living'. However, most of the IVD techniques disturb the particle beam and can alter the beam properties. Pre-treatment *ex-vivo* or *in-vitro* verification checks for individual patients taking external beam radiotherapy are performed using independent dose-monitor unit calculation programs and experimentally using ionisation chambers and diode arrays. The current report focuses on the characteristics, advantages and limitations of the clinically available *in-vivo* dosimetry techniques.

Detectors for real time *in-vivo* dosimetry (invasive)

1. ***Silicon Diodes [51]*:**
   - Silicon diodes after its first implementation in 1980 were used routinely formerly for *in-vivo* dosimetry.
   - Advantages: Real-time readout, high sensitivity, simple instrumentation, reliability.
   - Limitations: Correction factor are required for the dependence of the signal on dose rate, irradiation angle and energy. Varying response with temperature and spectral range of radiation. Change in sensitivity post irradiation.
2. ***MOSFETs [52]*:**
   - MOSFET dosimetry is based on the measurement of the change in threshold voltage that is a linear function of dose [52].
   - Used in split beam treatments, TBI, IMRT, serial tomography, and IGRT.
   - Advantages: excellent spatial resolution with minimum attenuation due to small size, can be used to monitor the dose rate.
   - Limitations: Variation with energy and incident angle. Response affected by temperature, response changes with accumulated dose, lower accuracy and precision, limited lifetime.
3. ***Plastic Scintillation detectors (PSD) [50]***
   - Promising in *in-vivo* dosimetry and QA. Not widely used due to their lack of commercial availability.
   - Advantages: favourable diametric characteristics including water-equivalence, energy independence, dose-linearity and resistance to radiation damage, no correction factors are required, excellent spatial resolution due to small volume, real time detection. Uncertainty of about 1% is demonstrated.
   - Limitations: Lack of commercial availability.
4. ***Electronic portal imaging device (EPID) [50]*:**
   - Advantages: Provide 2D and 3D dosimetric information, response independent of dose rate and approximately linear with integrate dose.
   - Limitations: over sensitivity to photons of lower energy, continuous signal after irradiation (ghosting).

***Detectors for passive in-vivo dosimetry*:**

Passive dosimeters provide a record of the dose which requires finite time for read-out:

1. ***Thermoluminescent dosimeter (TLD) [53]***
   - Absorbs radiation energy retaining it in metastable states and release them in the form of light following the external excitation by heat. The amount of light produced is proportional to the radiation dose.

- Advantages: Multiple use, linear response over the dose.
- Limitations: Decrease in the signal due to spontaneous emission of light at room temperature (fading), labour intensive (require annealing and batch calibration), costly, and invasive.

2. ***Optically stimulated luminescence dosimeters (OSLD) [54]***
   - Similar to TLD, except, the light emission is stimulated optically instead of heat.
   - Advantages: removes the problem of 'fading' as in TLDs.
   - Limitations: Cannot be used multiple time due poor effectiveness of optical bleaching after measurement.
3. ***Radio-photoluminescence glass dosimeters [50]***
   - Passive solid state radiation detectors made up of silver activated phosphate glass. When exposed to radiation, stable ionisation centres are created which can be read multiple times using UV light. Ready to reuse after annealing at 400C for about an hour.
   - Advantages over TLD: very low fading, response is independent of temperature and photon energies above 0.2 MeV.
4. ***Radio-chromic films [50]***
   - Radio-chromic film uses a special dye that is polymerise and develops a colour upon exposure to radiation and hence is self-developing. It is relatively energy independent over a wider energy range, particularly in keV range. Information is read out using flat-bed scanners.
   - Advantage: can provide 2D dose information, permanent record.
   - Disadvantages: Cost specific scanning equipment and strict readout protocols.

1.5.4 Endstation Monte Carlo

A Monte Carlo simulation has been developed using the Geant4 toolkit with the primary goal being to evaluate the impact of various beam-line components on the low energy protons serving the Stage 1 *in-vitro* end station. Various configurations of the endstation have been simulated, including a default configuration matching that of the pre-CDR [2, 3]. The incident beam for the simulations can be chosen from a flat beam with a diameter of 35 mm or a Gaussian beam with sigma of 2.5 mm, and an incident beam energy of $15\,\mathrm{MeV} \pm 2\%$. The protons traverse a 25 μm Ti foil which serves as the beam window to preserve the vacuum and then a 100 μm thick Perspex window. The endstation is to be isolated from the beam pipe to allow a closed setup where the temperature and environment can be controlled as outlined in the consultation meetings. The thin Perspex window will allow for this whilst minimally perturbing the beam. Gas exchange studies will be conducted to test the feasibility of such a thin window for cell viability. A beam monitor is simulated in the endstation which can be selected from the Gas Jet Profiler, a plastic scintillator, or a Silicon pixellated detector. Following a 5 mm air gap a Polystyrene cell-dish base of thickness (1.2 ± 0.1) mm with 30 μm of cells grown onto it. Following this is either 2 mm of water or an air chamber matching a Markus Chamber in order to calculate the dose. At all of the material interfaces, the beam energy and profile is scored and the LET and dose deposited within each volume is recorded.

Accurate measurements of the cell dish base thickness are key for the Stage 1 endstation. Measurements of three sets of cell dishes have demonstrated intra-batch fluctuations of 0.1 mm. Within these fluctuations, the thicknesses are grouped into three distinct groups with uncertainties of just a few microns. This highlights an issue with the manufacturing process. Following the consultation meetings a decision was made to assume the use of plastic dishes, so the impact of the thickness changes has been studied. For the nominal 1.2 mm thickness, the energy onto cells is 7 MeV with an LET of 6.2 keV/μm. When allowing for the fluctuation in cell-dish thickness, the kinetic energy into the cells ranges between 6.2 MeV and 7.7 MeV with a similar range to the LET. Should the beam energy be lowered, or additional material be required before the samples, the loss of range could lead to significant changes. Therefore, the cell-dish thickness needs to be controlled. One source

of additional material would be glass cover slips onto which the cells are grown to allow certain end points to be studied. These cover slips have a water equivalent thickness of almost 0.3 mm and add significant additional material and changes to the beam parameters onto cells. Input from the radiobiological community is that these LETs are still in the low range and should not impact the results greatly as long as the beam parameters are well quantified and understood. A potential solution could be to use Mylar based cell dishes with a glass coverslip for cell growth. In this configuration, the kinetic energy into the cells is 13 MeV and the beam properties are more stable to additional material, but the experimental techniques required begin to diverge from standard procedures and advice received in the consultation meetings.

A study has started into the lowest potential beam energies which could allow a compelling proof-of-principle radiobiological experiment. For this study, the minimum amount of material possible in the beamline has been simulated, with the Gas Profiler being assumed to monitor the beam, and the endstation directly coupled to the beamline vacuum, separated by just the vacuum window. A Mylar cell base of just a few microns and a standard glass coverslip was included for cell growth, and a 30 μm cell layer is assumed. For this configuration, the distal edge of the Bragg peak is observed in the cell layer when a 5 MeV. This sets the absolute minimum capture energy for such an experiment to be conducted. The impact of dose gradients from these beams will be studied going forward.

The maximum dose rate offered by LhARA into the Stage 1 endstations has been studied and cross checked with a BDSIM-based simulation conducted in other work packages. Using the baseline pre-CDR geometry with the addition of the glass coverslip, the Markus chamber was placed directly after the cells—replacing the water volume. A beam of radius 5 mm and a Gaussian profile with sigma of 2.5 mm was incident upon the endstation. The dose delivered to the Marcus chamber per proton incident upon the beam monitor was found to be 1.44×10^{-8} Gy. When scaling for the nominal 10^9 protons per pulse and 10 Hz repetition rate, this yields 14.4 Gy/pulse and 144 Gy/s respectively.

The simulation will continue to be developed to reflect the Stage 1 and Stage 2 endstations over the next 12 months to understand the beam parameters and implications of endstation components.

1.6 Work package 1.6: Facility design and integration

1.6.1 Overview

The last six months have seen a significant progress in several areas:

- The recently proposed revision of the lattice for Stage 1 which uses seven (rather than the baseline 5) Gabor lenses has been explored proving its ability to deliver a spectrum of beams to the end-station and the provision of the matched beam required at the start of the FFA injection line for Stage 2. The optics matching was performed using the MAD-X [55] and tracking studies were performed, without space charge effects using BDSIM [56] and with space charge using GPT [57]. For the beam simulations the initial conditions from the SCAPA simulations were adopted. Optimisation of the beam matching with the presence of space charge was performed using GPT. The use of octupoles to improve the spatial uniformity of the beam distribution in phase space was studied with promising results. The performance of the lattice in simulations justified the proposal for the revised lattice to become the baseline for LhARA Stage 1.
- Further progress was made in understanding the geometry and space requirements for the Stage 1 lattice. In particular, a detailed study was performed of the setup of the laser beam, the target and the beam nozzle in the target chamber, taking into account requirements for laser diagnostics. Several essential items, such as shielding walls, vacuum pumps, vacuum valves, diagnostic devices, etc., were identified and added to the lattice schematic. Further work is expected to ensure that sufficient space is provided in all areas. Section 2 provides additional details.

Table 2: Beam parameters at exit of the target housing.

	Pre-CDR Beam	Smilei Sampled Beam	SCAPA Sampled Beam
Mean RMS Emittance [m]	3.26×10^{-7}	1.43×10^{-8}	8.25×10^{-8}
Mean Beta [m]	4.89	141.34	20.24
Mean Alpha	-50.22	-1418.43	-204.99

- A novel design for the lattice of the FFA post-accelerator was developed based on the double spiral scaling FFA principle. The lattice consists of ten identical cells containing two magnets each. For the nominal working point, $(Q_H, Q_V) = (2.83, 1.22)$, both magnets bend the beam in the same direction in the "Ff" configuration. A negative bend can be introduced in the "Fd" configuration. This lattice allows for a flexible choice of working point, if the k index can be varied by trim coils and the ratio of the fields in the doublet magnets can be changed. The choice between the baseline, singlet lattice and the aforementioned doublet lattice will be informed first by the design of the FETS-FFA magnet and then by the conceptual design of the LhARA FFA magnet.

1.6.2 Update on Stage 1 design

Ion source simulation update and baseline design performance

Simulations of the laser-target interaction in the PIC code OSIRIS [58] have shown differences to previous simulations with alternative codes. Since the LhARA/ITRF 6-month progress report [30], a simulation artefact was discovered which showed an artificial emittance growth which depended on the method of recording the beam profile in GPT; this issue is being documented and the GPT developers will be consulted. Beam transport within the target housing has been re-simulated with the latest beam parameters at the exit of the target housing. The new results are summarised in table 2 along with older simulation results. The beam parameters downstream of the target housing are very similar to those obtained previously and exhibit marginally better agreement with parameters assumed in the pre-CDR. These simulations of the laser-target setup at the SCAPA facility, which shares many properties with LhARA's proposed configuration, are considered the most reliable description of the beam to date.

Stage 1: 7 Gabor Lens Configuration

To address the challenges encountered with the baseline design, modification of the Stage 1 beam line into a configuration containing seven Gabor lenses has been the focus of recent work. The nominal Gabor-lens settings have been re-optimised in MAD-X given the updated parameters listed in table 2. The settings of the first three Gabor lenses are held constant for all spot-size configurations thus removing the need for the second energy selection collimator after Gabor lens 3 which was included in the 5-lens configuration. The Gabor=lens electron densities and equivalent strength solenoid fields are listed in table 3. The re-matched Gabor lens strengths for all spot-size configurations are listed in table 4.

The vertical beam size for 5 nominal spot-size configurations is shown in figure 22. Identical horizontal beam sizes are also achieved (not shown). Beam size is calculated including dispersion and an energy spread of $\pm 2\%$.

Performance and Optimisation

The performance of the full Stage 1 beam line for the 3.0 cm spot size configuration, when considering space charge forces, is shown in figure 23. In all simulations, when modelling space charge, a total of 10^9 particles per

Table 3: Nominal strength parameters of the first 3 Gabor lenses in the 7 Gabor lens configuration and their equivalent-solenoid fields.

	Equivalent-solenoid field (T) field (T)	Gabor lens e^- density ($\times 10^{15}\ m^{-3}$)
GL1	1.4000	5.188
GL2	0.5724	0.867
GL3	0.8139	1.753

Table 4: Equivalent=solenoid field strengths of matching solutions for 5 endstation spot sizes. Also shown is a configuration for FFA injection line matching, meeting the β=50 m requirement (* denotes beam sizes included for completion).

Spot size (2 σ diameter) (cm)	1 σ radius (mm)	Beta Value (m)	GL4 (T)	GL5 (T)	GL6 (T)	GL7 (T)
3.0	7.5	704.89	0.9942	0.9018	0.6964	0.6690
2.5	6.25	489.51	0.9974	0.8639	0.7306	0.7268
2.0	5.0	313.28	0.9999	0.8230	0.7866	0.8153
1.5	3.75	176.22	0.9999	0.7710	0.7137	1.0059
1.0	2.5	78.32	0.9058	0.8014	0.1292	1.2856
0.8*	2.0*	50.0	1.1875	0.5833	1.4000	0.3982

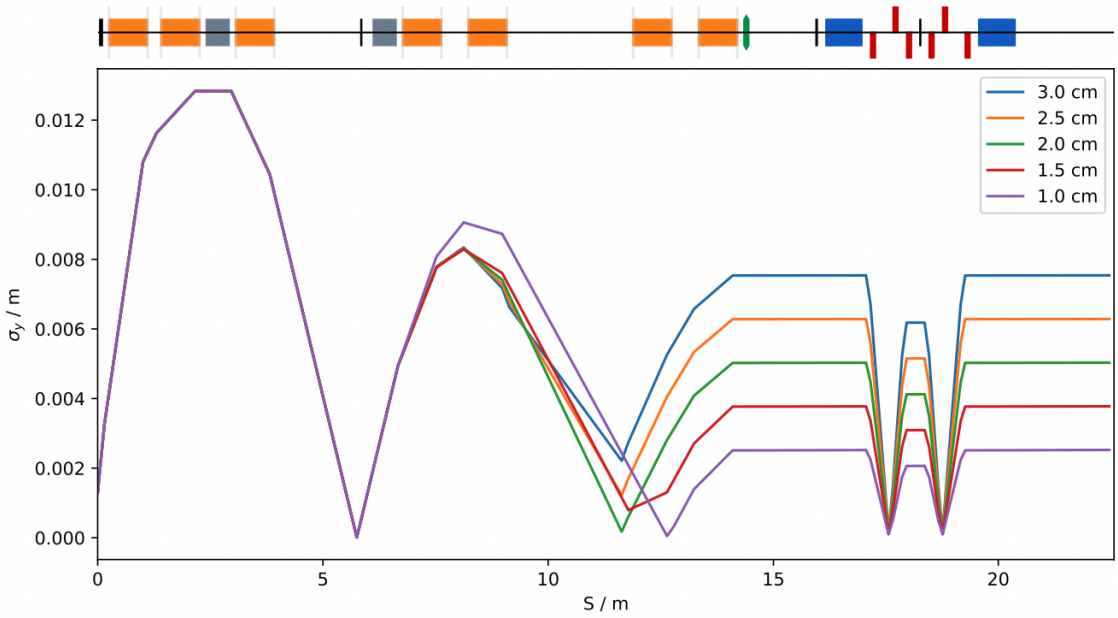

Figure 22: Nominal vertical beam size for 5 optics configurations of the LhARA stage 1 lattice to yield spot sizes of 3.0, 2.5, 2.0, 1.5, and 1.0 cm.

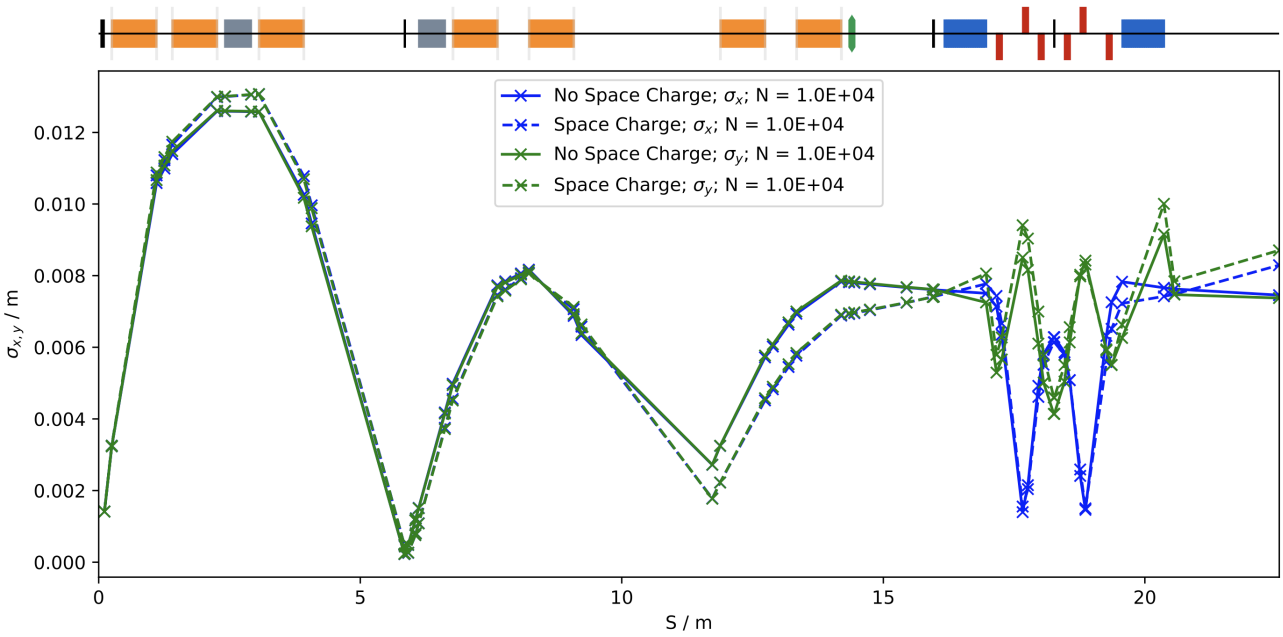

Figure 23: Impact of space-charge effects on nominal optical performance of the 7 Gabor lens configuration. N denotes number of macroparticles used in all tracking simulations.

bunch is assumed and represented by 10,000 macroparticles. Optimisation procedures were again performed to meet three objectives: parallel beams at the end of the capture and matching sections and the position of the focal plane of the third Gabor lens is required to be at the position of the energy collimator. The 1.4 T equivalent-solenoid-field limit is also kept as a constraint. Optimisation was again performed using GPT.

The strengths of the first three Gabor lenses are common to all optics configurations, so these beam-line elements are optimised first. Optimisation was performed in two stages. First, a parallel beam is produced after the second Gabor lens. The Courant-Snyder α function is optimised to be zero at three locations: the start of the first RF cavity, the midpoint of the cavity, and 2 m downstream. The beam size, constrained manually, is decreased until no further solutions can be found. This procedure yields the smallest possible beam size in the capture section. The midpoint of the RF cavity is chosen as an equidistant point between the second and third lenses. The point 2 m downstream also guarantees a parallel beam over a long distance and permits flexibility in the distance between Gabor lenses 2 and 3. The strength of the first lens is kept constant. For the second optimisation, α is constrained to be zero at the collimator location. The beam is tracked until the midpoint of the second RF cavity. The optimised beam size optics is shown in figure 24. A parallel beam has been achieved after Gabor lens 2, as shown by the dotted lines, confirming the flexibility to modify the drift length at this location without impacting the beam-tracking performance. The optimised Gabor-lens parameters and equivalent-solenoid field strengths are listed in table 5.

When simulating the capture section, the emittance was monitored at regular intervals and shown to grow throughout, even when space charge forces were not modelled. The beam-line model at present useing the equivalent solenoids. In solenoids, beam emittance is known to exhibit transverse coupling and has also been shown not to be conserved, particularly for the case of diverging beams [59, 60]. Whilst this will not impact endstation spot-size optimisation where only the beam size is constrained, this will impact the optimisation for $\beta = 50$ m for the FFA injection line. This emittance growth is still under investigation.

Spot Size Configurations

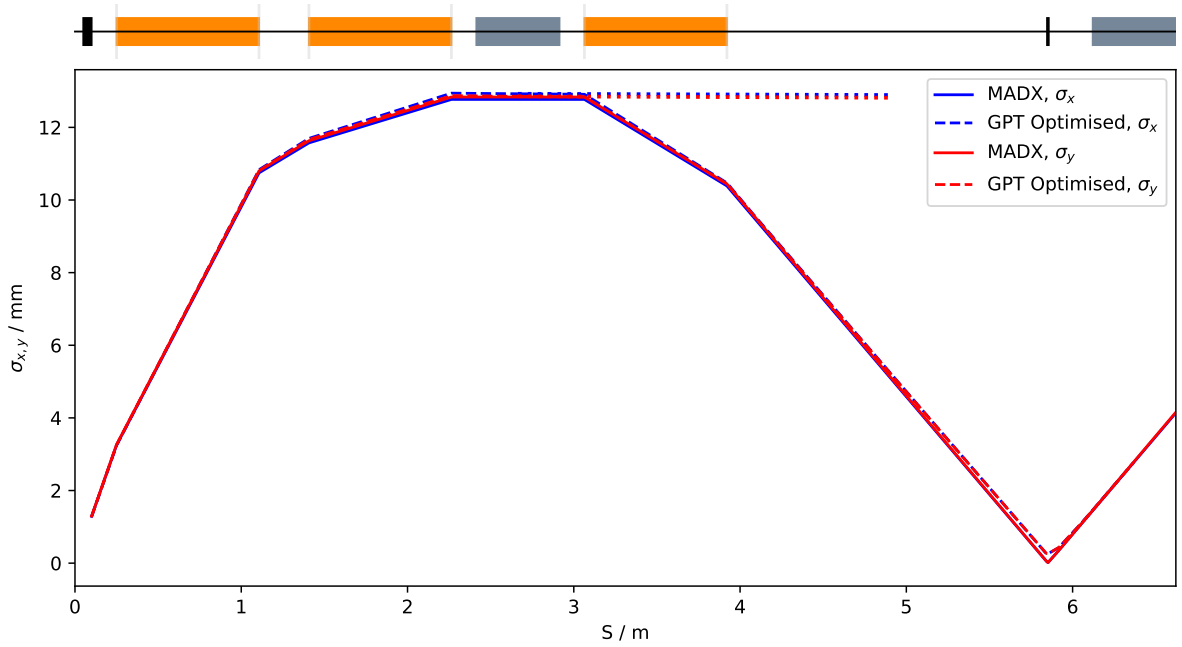

Figure 24: Beam size in the LhARA capture section with optimised Gabor lenses 1–3. The dashed lines show a parallel beam achieved when only considering the capture section, demonstrating flexibility in the drift length between the second and third Gabor lenses.

Table 5: Optimised strength parameters of Gabor lenses 1 to 3 & their equivalent-solenoid field.

	Equivalent-solenoid field (T) field (T)	Gabor lens e^- density ($\times 10^{15}$ m^{-3})
GL1	1.4000	5.188
GL2	0.5875	0.913
GL3	0.8146	1.756

Table 6: Optimised beam parameters at the vertical arc entrance for the 3.0 cm, 2.5 cm, and 2.0 cm spot size configurations.

Target Spot Size /	Emittance ($\times 10^{-6}$ m rad)		α		β (m)		Beam Size (mm)	
1 σ radius	X	Y	X	Y	X	Y	X	Y
3.0 cm / 7.50 mm	3.645	3.740	-0.044	-0.021	15.648	15.618	7.494	7.583
2.5 cm / 6.25 mm	3.633	3.729	-0.024	-0.0005	11.051	11.005	6.286	6.356
2.0 cm / 5.00 mm	3.493	3.604	-0.206	-0.172	7.687	7.347	5.141	5.106

For spot size optimisation, two methodologies have been used. For the larger spot sizes, the strength of lenses 4 to 7 are allowed to vary until the beam size constraints are met at 4 locations; the beginning of the octupole, 30 cm after the octupole, 1 m after the octupole, and a point 2 m downstream, to ensure a parallel beam. Achieving smaller spot sizes when varying all 4 lenses often failed to find solutions, therefore optimisation for some configurations is split. Lenses 4 and 5 are varied until a beam waist is achieved at the same location as the MAD-X optics which differs in each configuration as seen in figure 22. In some configurations this waist is within lens 6, therefore lenses 6 and 7 are turned off when optimising. Lenses 6 and 7 are then separately optimised with the beam starting at the exit of Gabor lens 5 (0.15 m downstream of lens 5). The vertical arc was not included in any optimisation simulations due to the large increase in computation time it requires. Once optimised, the whole Stage 1 beam line is simulated, including the vertical arc, to ensure a parallel beam and correct spot size at the endstation.

Figure 25 shows the optimised horizontal and vertical beam size for the 3.0 cm, 2.5 cm, and 2.0 cm spot-size configurations. The full Stage 1 beam line is simulated to assess the beam delivered to the endstation. In all configurations, the beam leaving the vertical arc is slightly divergent with the divergence increasing for smaller spot sizes. The beam parameters at the vertical-arc entrance are listed in table 6. For the larger spot sizes we are confident that a parallel beam can be achieved with minor corrections to the final 4 Gabor-lens strengths or vertical arc magnets. A beam size asymmetry is also observed; this originates in the generated beam; however, it is not apparent until the arc due to the lenses focusing equally in both transverse planes.

The beam profile and phase space at the endstation are shown in figure 26. The profile is broadly similar to that achieved with the 5 Gabor lens model. The aberration arising in the solenoids remains, resulting in the bow-tie-like transverse phase-space distributions. The beam profile appears slightly off-axis in the vertical plane, this may impact beam uniformity studies with the octupoles, however a number of corrector magnets are planned to be included in the beam line. The location of these has yet to be finalised, the impact of this offset will be investigated in future studies. The temporal profile and spectrum remain predominantly uniform as intended. The optimised Gabor lens parameters and the equivalent solenoid field strengths for the 3.0 cm, 2.5 cm, and 2.0 cm configurations are listed in table 7.

For the 2.0 cm spot size, the rate of divergence is detrimental to the beam transport performance despite it being the best solution achievable with GDFSOLVE [57] when not considering the vertical arc in simulations. To correct this, the vertical arc was optimised in MAD-X. The beam dimensions and single-plane focusing in the vertical arc diminish any major impact from space-charge forces, therefore a MAD-X-tracked beam can be considered a good approximation of LhARA's beam dynamics behaviour. All quadrupoles were varied with their focusing strengths, $K1$, limited to $\pm$ 40 m^{-2}. The magnet-strength symmetry seen in the baseline design was not maintained. The beam was constrained at 3 locations in the 2.0 m drift after the vertical arc, each separated by 0.5 m. The Courant-Snyder $\alpha_{x,y}$ functions, vertical dispersion and its derivative were all constrained to 0. The $\beta_{x,y}$ functions were constrained to a target of 7.158 m horizontally and 6.936 m vertically, given the emittances listed in table 6. Optimised quadrupole strengths were found and validated in GPT, with

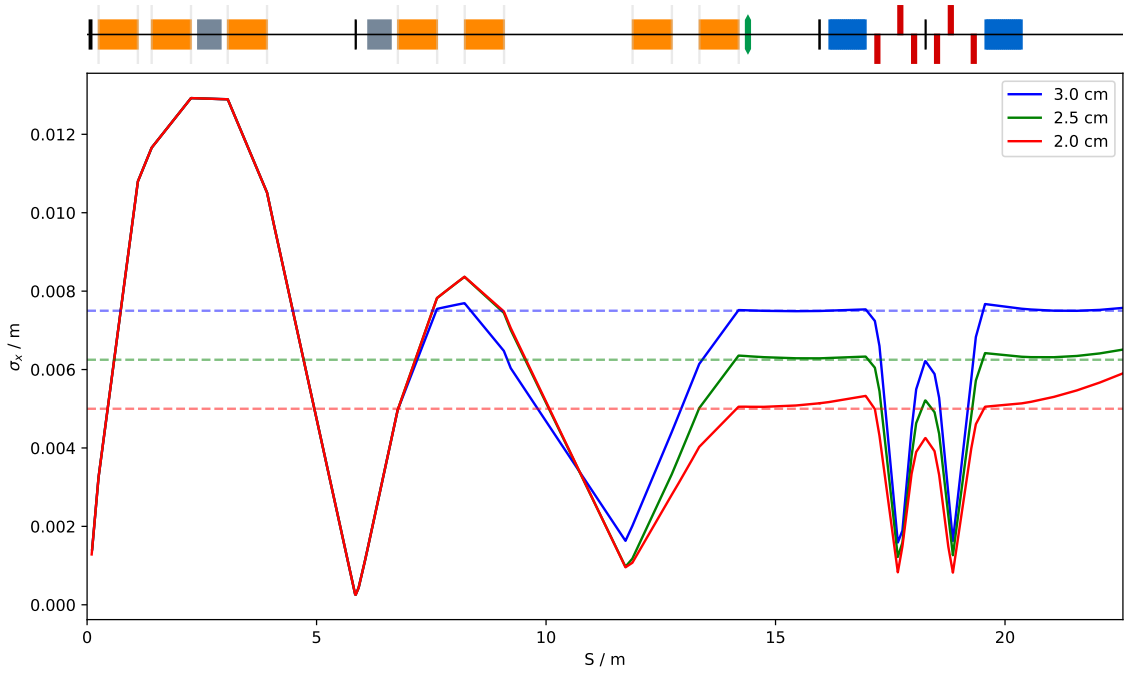

(a)

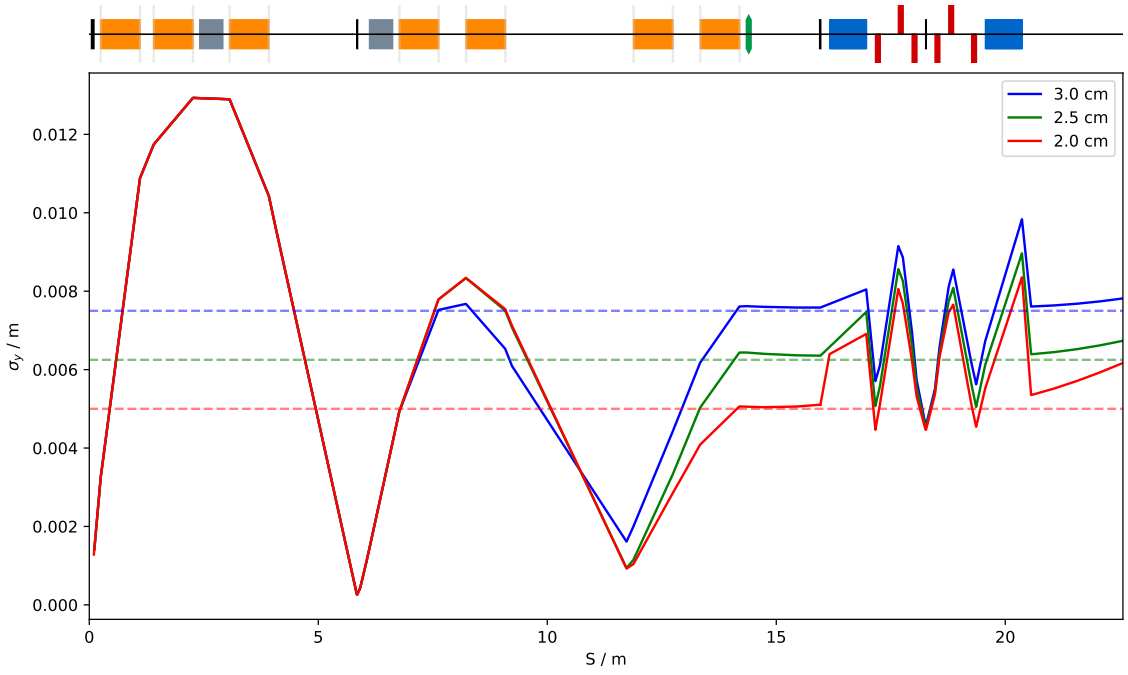

(b)

Figure 25: Optimised horizontal (a) and vertical (b) optics of the 7 Gabor lens design for spot sizes of 3 cm, 2.5 cm, and 2 cm, with target sizes indicated by the dashes lines.

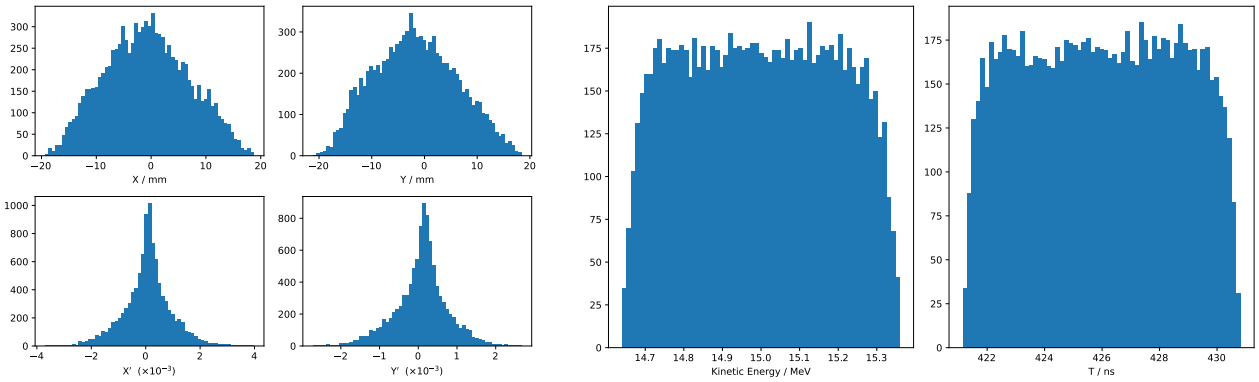

(a) (b)

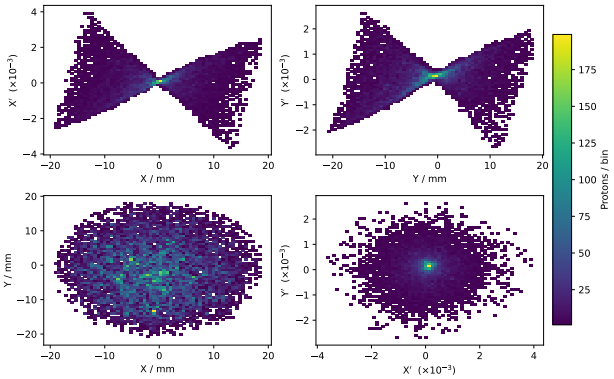

(c)

Figure 26: endstation beam profile and phase space for the 3.0 cm spot size configuration

Table 7: Optimised parameters of the 7 stage 1 Gabor lenses & equivalent-solenoid fields for the 3.0 cm, 2.5 cm, and 2.0 cm spot size configurations.

Spot Size Configuration	Gabor Lens	Equivalent-solenoid Field (T)	Gabor lens e^- density ($\times 10^{15}\ m^{-3}$)
3.0 cm	GL4	1.072940	3.0470
	GL5	0.807211	1.7246
	GL6	0.001191	4×10^{-6}
	GL7	0.787153	1.6400
2.5 cm	GL4	0.996313	2.6273
	GL5	0.832585	1.8348
	GL6	0.000871	2×10^{-6}
	GL7	0.858701	1.9517
2.0 cm	GL4	0.995976	2.6255
	GL5	0.823955	1.7969
	GL6	0.749300	1.4860
	GL7	0.836557	1.8523

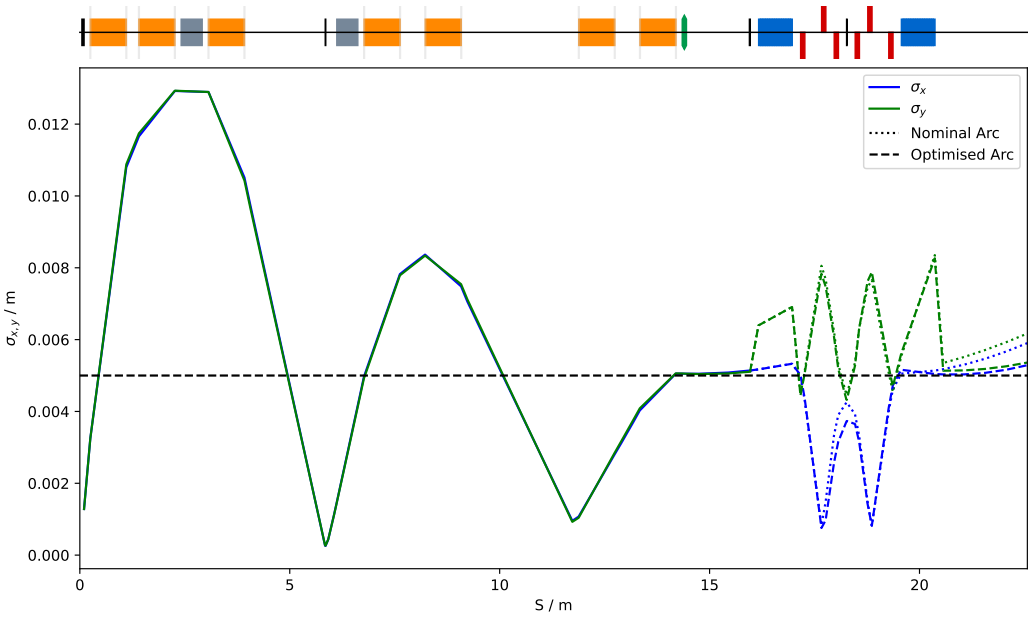

Figure 27: Beam size for the 2.0 cm spot size configuration with optimised vertical arc. The target 1 σ beam radius is indicated by the black dashed vertical line.

Table 8: Optimised strengths of the stage 1 vertical arc quadrupoles for the 2.0 cm spot size configuration.

Quadrupole	Nominal K1	Optimised K1
LHA-LEL-MAG-QUAD-01	-22.5440	-21.1299
LHA-LEL-MAG-QUAD-02	31.3768	30.8374
LHA-LEL-MAG-QUAD-03	-31.5123	-29.5522
LHA-LEL-MAG-QUAD-04	-31.5123	-36.2771
LHA-LEL-MAG-QUAD-05	31.3768	32.4886
LHA-LEL-MAG-QUAD-06	-22.5440	-22.4983

the strengths shown in table 8. The GPT model was subsequently simulated with space-charge effects. The beam size optics are shown in figure 27 along with the target beam radius. A significant improvement in the beam size is observed, without impacting the form of the transverse profiles as seen in figure 28. The longitudinal profile and spectra are not impacted by the optimisation.

A notable difference in the arc optics is seen at the collimator where the horizontal beam size is smaller than the nominal design. As engineering efforts have also identified a possible requirement for length modifications in the vertical arc, the impact of the beam asymmetry on collimator performance in addition to possible re-optimisation will be studied at a later date in dedicated collimator studies.

At the time of writing, optimised solutions are yet to be found for the smallest spot sizes despite multiple optimisation methods being used. Results show consistent behaviour of beam focusing with a waist within $\sim$2 m of the final Gabor lens. Optimisation to achieve these smaller spot sizes remains an ongoing effort. Engineering efforts, however, have identified that minor modifications to the optics design are likely to be needed to accommodate diagnostics and operational apparatus, e.g. radiation shutters, vacuum pumps, Gabor lens electron-cloud injectors etc. Optimisation for smaller spot sizes will therefore be performed when a better un-

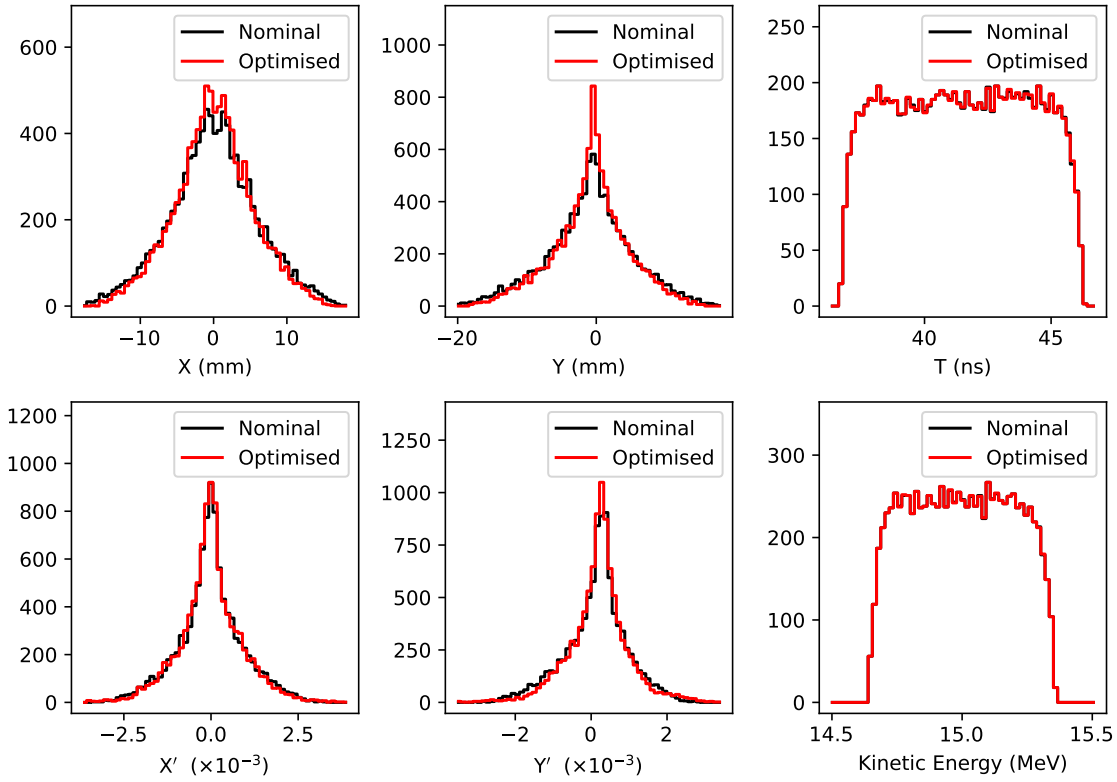

Figure 28: Beam profile and spectrum comparison at the endstation with a nominal and optimised vertical arc for delivering a 2.0 cm spot size.

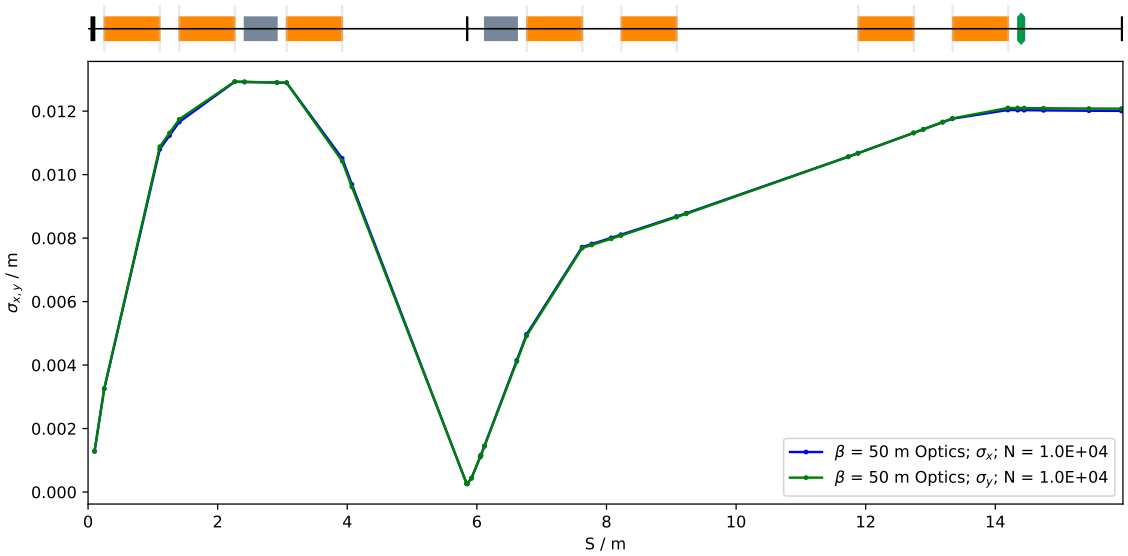

Figure 29: Beam size for the stage 1 configuration to meet the FFA injection line requirements.

Table 9: Beam parameters at the entrance of the FFA injection line switching magnet.

Parameter	GPT Value	Unit
ϵ_x	3.016×10^{-6}	[m rad]
ϵ_y	2.902×10^{-6}	[m rad]
α_x	0.0796	[1]
α_y	0.0709	[1]
β_x	48.682	[m]
β_y	51.165	[m]

derstanding of length modification requirements is reached.

FFA Injection Line Beam Conditions

Optimisation of Stage 1 to meet the FFA injection-line conditions has been achieved with constraints on the Courant-Snyder functions $\alpha = 0$ and $\beta = 50$ m. Whilst a solution was found with all four Gabor lenses actively focusing the beam, their impact on the emittance growth resulted in a larger than anticipated beam. As such, optimisation was tested where the fields of Gabor lenses 5 and 6 were set to zero. A solution was found yielding a smaller beam size, the optics of which are shown in figure 29. The final beam parameters at the entrance of the FFA injection line switching dipole are listed in table 9. The asymmetry previously observed is more apparent, however this cannot be mitigated with lenses alone. Is is believed that optimisation of the FFA injection can correct this, however the FFA ring and injection line are being redesigned at the time of writing, with updates to be published at a later date. The beam parameters achieved here are considered sufficient for beam transport through the current FFA injection line in the baseline design. The optimised Gabor lens electron densities and equivalent-solenoid fields are listed in table 10.

Preliminary octupole performance assessment

To achieve a flat transverse beam profile at the endstation, LhARA will use octupole magnets exploiting a

Table 10: Optimised strength parameters of Gabor lenses 4 to 7 and their equivalent-solenoid field for matching the FFA injection line requirements.

	Equivalent-solenoid field (T)	Gabor lens e^- density ($\times 10^{15}\ m^{-3}$)
GL4	1.0269	2.791
GL5	0	0
GL6	0	0
GL7	0.3129	0.259

known uniformity technique [61–63]. A degree of uniformity has been demonstrated in LhARA's pre-CDR [3], however the lattice modifications require that the feasibility of octupole correction be re-established. Scans of octupole strengths at the same order of magnitude as the pre-CDR proved challenging, with no strengths found to produce sufficient uniformity at the endstation. The transverse beam profile resulting from two example normalised octupole strengths, $K3$, of 60000 m^{-4} and 150000 m^{-4}, and the profile with no octupolar field, are shown in figure 30.

Whilst the 2D profiles clearly exhibit the characteristic filaments from octupular focusing, the central region appears either to be over-focused or to have experienced insufficient field strength to affect the beam as desired. When investigating the BDSIM data, the profile at the end of the vertical arc, or the start of the 2 m long vertical drift, was observed to exhibit far better uniformity in the horizontal axis, as shown in figure 31. Vertically, the asymmetry in beam size observed in spot size optimisation is observed as an asymmetric profile with the beam being 1.9 mm off axis at the octupole entrance. Due to the improved distribution at the end of the arc, movement of the octupole to the end of the arc was tested. A range of octupole strengths were simulated; figure 32 shows the qualitative transverse beam profile at the endstation, 2 m downstream of the octupole for $K3$ strengths of 0 m^{-4}, 30000 m^{-4}, and 80000 m^{-4}. Significant improvement is seen in the uniformity compared to that in figure 30. A nominal strength of $\sim$ 30000 m^{-4} exhibits some degree of uniformity, with higher strengths exhibiting over-focusing, however, optimisation will be conducted when further lattice modifications have been made.

Despite improved uniformity, the vertical asymmetry remains. This is believed to be a result of a mean vertical offset. This offset was artificially removed with the mean bunch position being subtracted from all particle coordinates. Figure 33 shows the beam profile at the endstation for the shifted beam has improved uniformity whilst not impacting the transverse profile. Whilst still imperfect, it indicates a strong beam position sensitivity for octupole-based uniformity correction. Planned studies of corrector magnets will investigate this further.

The field magnitude at the pole tip was calculated to be $\sim 0.82\,\mathrm{T}$ for $K_3 = 30000\,m^{-4}$, where K_3 is the normalised field gradient defined as

$$K_3 = \frac{1}{B\rho}\frac{d^3B_y}{dx^3}. \tag{1}$$

The calculation was performed using the field components:

$$\begin{aligned} B_x &= -\frac{d^3B_y}{dx^3}(y^3 - 3x^2y)\,; \\ B_y &= \frac{d^3B_y}{dx^3}(x^3 - 3y^2x)\,; \text{and} \\ B_z &= 0\,. \end{aligned} \tag{2}$$

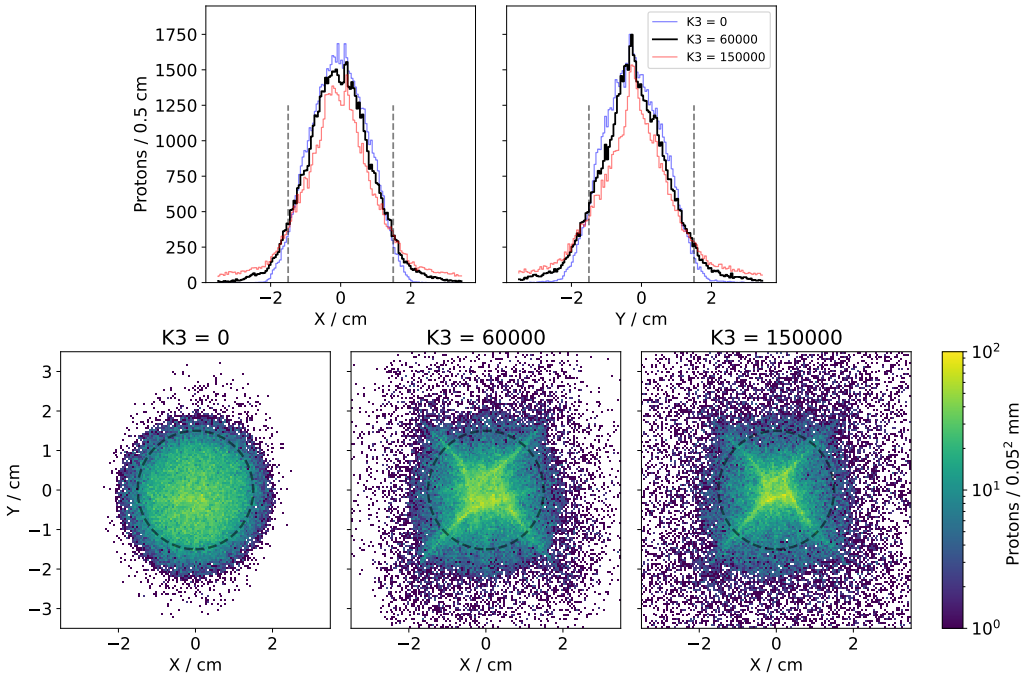

Figure 30: Transverse beam profile at the endstation from the matching section octupole with normalised $K3$ strengths of 0, 60000, and 150000 m^{-4}. Top: Horizontal and vertical 1D beam profiles. The black dashed lines shows the 2 σ radius for a 3.0 cm spot size beam. Bottom: full 2D spatial profile. The black dashed circle shows the 2σ radius for a 3.0 cm spot size beam.

Equations 2 were evaluated assuming a 15 MeV beam and an aperture of radius 3.65 cm. Such field strengths are larger than are normally considered in the literature due to the large aperture requirement. Whilst not small, the field values are believed to be achievable.

Octupoles for producing uniform beams for LhARA remain feasible, if corrector magnets can be shown to reduce the beam offset. Positioning the magnet at the end of the vertical arc yields more uniform distributions. Further optimisation is needed. The uniform region, however, remains smaller than the desired spot size, thus optimisation of the Gabor lens strengths for larger profiles may be required. Downstream collimation would also be required to reduce the lateral fall-off distance. The proximity of this additional collimation to the endstation will require careful consideration.

Summary

When attempts were made to retune the original baseline configuration of the Stage 1 beam line following recent PIC simulations of LhARA's laser-target setup, it proved to be difficult to achieve the flexible spot size and beam uniformity at the Stage 1 endstation. In addition, it was not possible to deliver the beam conditions required for injection into the FFA. A new beamline design with 7 Gabor lenses was therefore developed and shown to provide greater flexibility than the original baseline design. Optimised Gabor lens strengths have been shown to deliver beams 3.0 cm, 2.5 cm, and 2.0 cm in diameter to the endstation whilst mitigating space-charge effects. In the 2.0 cm beam case, changes to the quadrupole strengths in the vertical arc were needed. Two further idealised configurations have shown that spot sizes of 1.5 cm and 1.0 cm are possible, The challenges in mitigating space charge as well as planned lattice modifications to accommodate diagnostics and other components will be the subject of future studies. The 7 Gabor lens beam line has been shown to meet FFA injection line beam requirements.

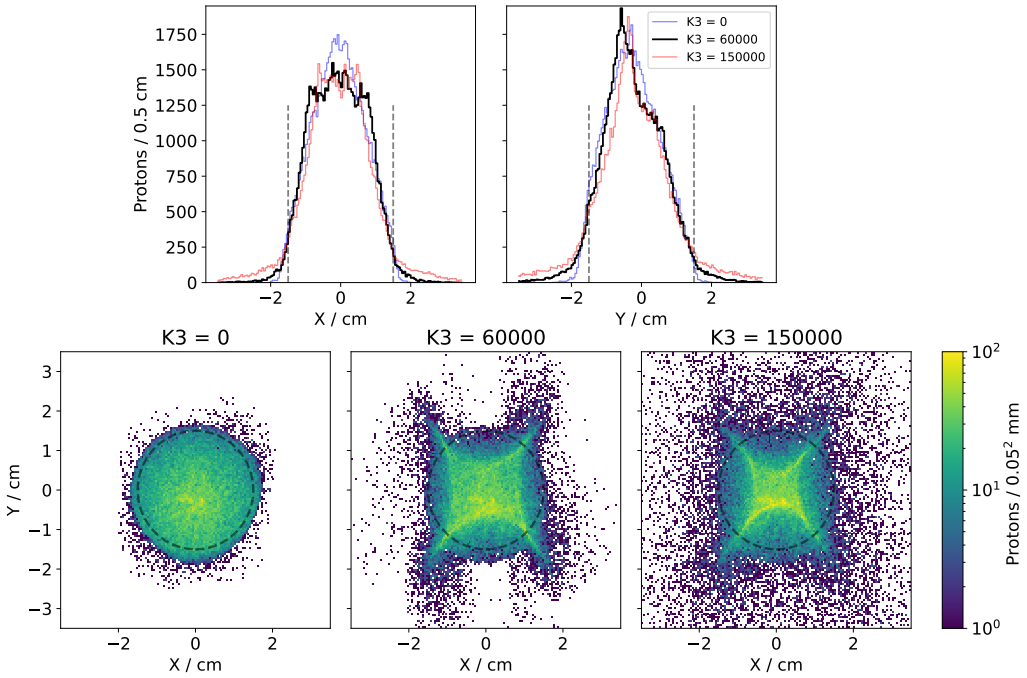

Figure 31: Transverse beam profile at the end of the vertical arc from the matching section octupole with normalised $K3$ strengths of 0, 60000, and 150000 m^{-4}. Top: Horizontal and vertical 1D beam profiles. The black dashed lines shows the 2 σ radius for a 3.0 cm spot size beam. Bottom: full 2D spatial profile. The black dashed circle shows the 2 σ radius for a 3.0 cm spot size beam.

One octupole has been removed due to inefficient positioning. Octupole-strength studies revealed that beam uniformity is best achieved when the remaining octupole is relocated to the end of the vertical arc. A normalised octupole strength of around $K_3 = 30000\,\mathrm{m}^{-4}$ has been identified. It has been shown, however, that uniformity is sensitive to beam position and corrector magnets would be required upstream.

1.6.3 Update on FFA post-accelerator design for Stage 2

The status of the baseline lattice for the FFA post-accelerator can be found in [3]. The FFA work in the last six months focused on the development of a novel design, which will allow for a flexible choice of the working point. This flexibility will enable the machine to be tuned around the nominal working point to avoid dangerous resonances driven by lattice imperfections and misalignments or to operate at different working points designed, for example, for slow extraction based on the third-order resonance or for working points for a high intensity round beam.

The novel lattice design is based on the double spiral scaling FFA principle [64], which is under consideration for the ISIS upgrade and for the proposed test ring FETS-FFA at RAL. In this type of the lattice, each cell consists of two magnets, each with spiral geometry, the magnetic field being governed by the scaling law. In the original proposal [64], magnets in the cell have opposite field polarity. To minimise the size of the ring, while keeping the length of the long straight section approximately the same as in the baseline, both magnets in the cell have the same polarity yielding the nominal working point $(Q_H, Q_V) = (2.83, 1.22)$. This configuration, called Ff, which denotes "Focusing"–"focusing", should be distinguished from Fd denoting "Focusing"–"defocusing", where the fields in the doublet magnets are in opposite directions. The small letter in this notation means that the additional second magnet in the cell is shorter and in general weaker. In fact,

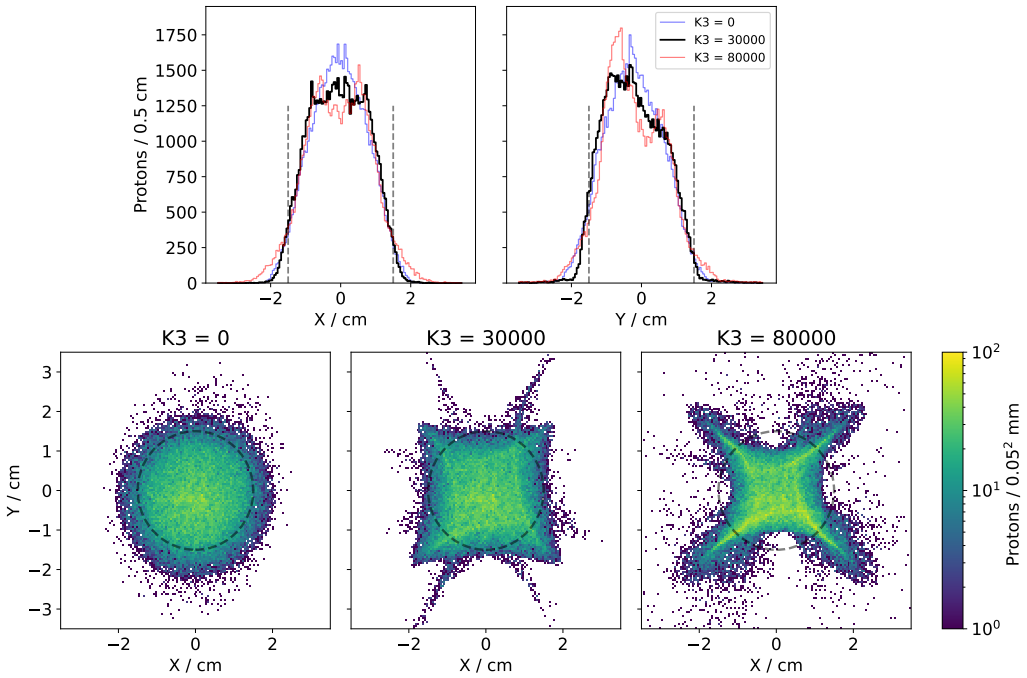

Figure 32: Transverse beam profile at the endstation from an octupole moved to the end of the vertical arc with normalised $K3$ strengths of 0, 30000, and 80000 m^{-4}. Top: Horizontal and vertical 1D beam profiles. The black dashed lines shows the 2 σ radius for a 3.0 cm spot size beam. Bottom: full 2D spatial profile. The black dashed circle shows the 2σ radius for a 3.0 cm spot size beam.

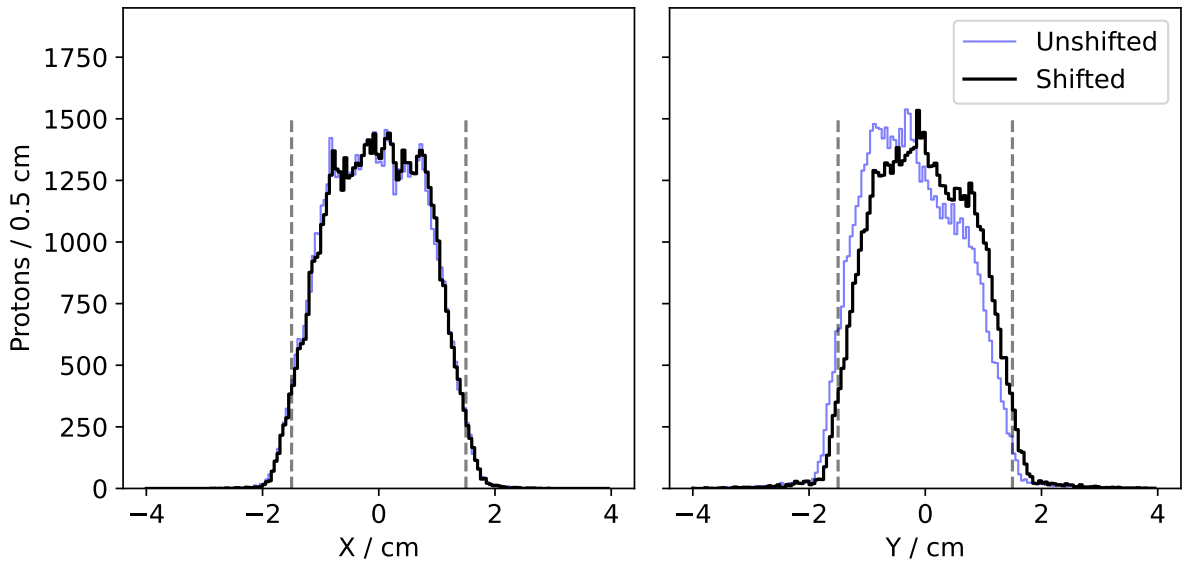

Figure 33: Transverse beam profile at the endstation from an octupole moved to the end of the vertical arc with a normalised $K3$ strengths of 30000 m^{-4} with a vertically shifted and unshifted beam entering the octupole. The black dashed lines shows the 2 σ radius for a 3.0 cm spot size beam.

it can be treated as a realisation of the concept of an "active clamp", where the adjustment of the field shape while keeping the field integral constant across the cell, affects the flutter functions, influencing, mainly, the vertical tune. The choice of length for the f magnet and the distance between the F and f follows approximately the design of the FETS-FFA magnets and is likely to be further adjusted.

The main parameters of the novel double spiral FFA lattice for the nominal tune are summarised in table 11. The layout is shown in figure 34. The lattice consists of ten identical cells each containing a doublet of scaling spiral magnets. The beam dynamics in the lattice is simulated using the 3D magnetic-field map created using the ideal scaling law. The fringe fields are described using the Enge model. The field map is calculated including fields from the adjacent cells. The contour of the field on the median plane in one lattice cell together with the closed orbits for the injection and extraction energies is shown in figure 35. The figure also shows the vertical magnetic field on the median plane as a function of the cell opening angle for two specific values of the radius close to the injection and extraction orbits. The betatron functions across the lattice cell, shown in figure 36, are calculated via tracking through the field map. The dependence of tunes on proton energy is shown in figure 36 and confirms the zero-chromatic behaviour of the lattice expected in the scaling FFA machine. The dynamic acceptances over 5000 cell crossings (500 turns) are shown in figure 37 and are significantly larger than needed to accept the beam from the laser source.

The novel double spiral scaling machine can also be tuned to the Fd configuration although the maximum achievable energy may be lower than the baseline value. To explore this configuration, the field map for the specific working point $(Q_H, Q_V) = (2.22, 2.19)$, assuming 3 MeV injection energy, was found. Such a working point would allow to study the space-charge effects with round beams and to study the original configuration of the double spiral FFA with reversed bending. The beam at injection to the FFA is expected to be space-charge dominated, even at the reference injection energy of 15 MeV due to a very short bunch length. Potential flexibility offered by the novel doublet lattice could be beneficial for radiobiological applications, but would also allow the exploration of FFAs in novel configurations and beam conditions.

The choice between the baseline singlet lattice and the novel doublet lattice described above depends on the level of flexibility needed for machine operation taking into account that variable energy extraction requires the magnets to be operated at various field values and therefore operation at different iron-saturation levels. The decision to revise the current baseline will be informed by the conceptual design of the LhARA FFA magnet. Current effort focuses at the FFA magnet design for the FETS-FFA ring and will be followed by the dedicated LhARA magnet conceptual design.

Future studies will include further lattice optimisation, injection line modifications, the conceptual designs for the magnet, the ring RF system and the beam diagnostics.

Table 11: LhARA double spiral scaling FFA ring parameters for the nominal tune.

Parameter	*Value*	*Units*	*Comments*
Lattice name:	Nominal LhARA doublet		
Lattice type:	Double spiral scaling FFA		
N:	10		
k:	5.26		
Spiral angle:	45.87	degrees	
B_{max}:	1.5	T	
R_{max}:	4.14	m	
R_{min}:	3.55	m	
(Q_H, Q_V):	(2.83, 1.22)		
Packing factor:	0.386		
Nominal proton injection energy:	15	MeV	
Nominal proton extraction energy:	127.4	MeV	
h:	1		
RF frequency:	2.37-5.47	MHz	
Configuration:	Ff		
F magnet opening angle:	0.163845 (9.38763)	rad (degrees)	
F magnet defining vertical field:	1.442559	T	on the median plane at R=4.26 m
f magnet opening angle:	0.039467 (2.26129)	rad (degrees)	
f magnet defining vertical field:	0.211023	T	on the median plane at R=4.26 m
Short drift opening angle:	0.039467 (2.26129)	rad (degrees)	
Enge coefficients:	C1=2.1		others are zero
Fringe field length:	0.12	m	at R=4.26 m
Fringe field opening angle:	0.028169 (1.61396)	rad (degrees)	

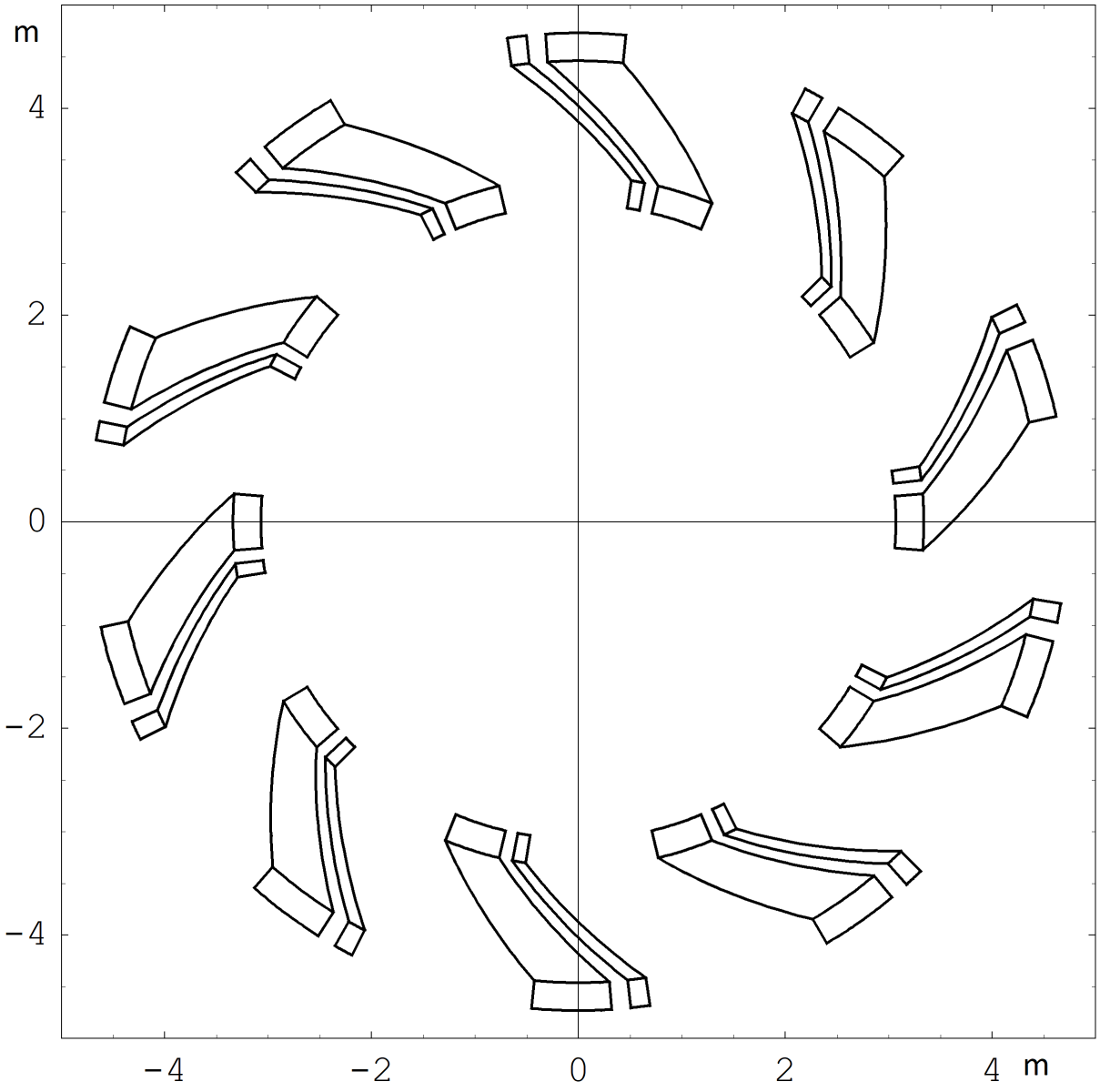

Figure 34: Layout of the double spiral scaling FFA ring.

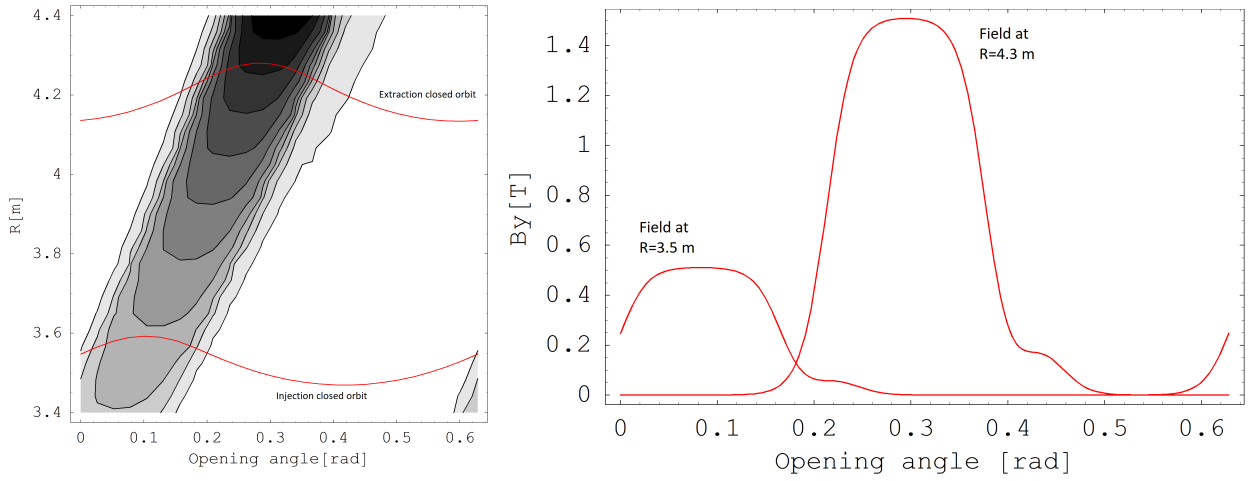

Figure 35: Magnetic field in cylindrical coordinates on the median plane in one LhARA lattice cell for the nominal working point plotted together with the injection and extraction closed orbits (left) and the vertical field on the median plane for two values of radius as a function of opening angle (right).

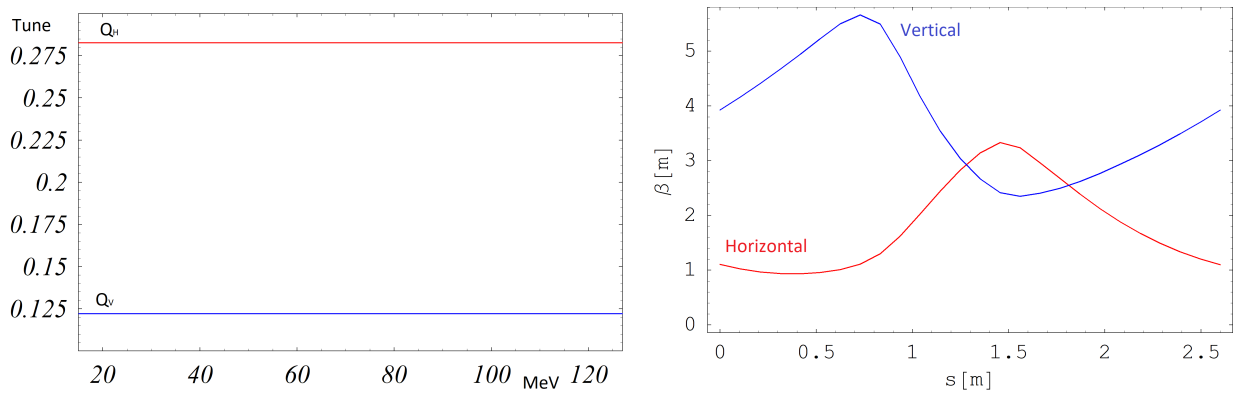

Figure 36: Tunes per cell calculated in tracking studies using 3D field map (left) and betatron functions in one lattice cell(right).

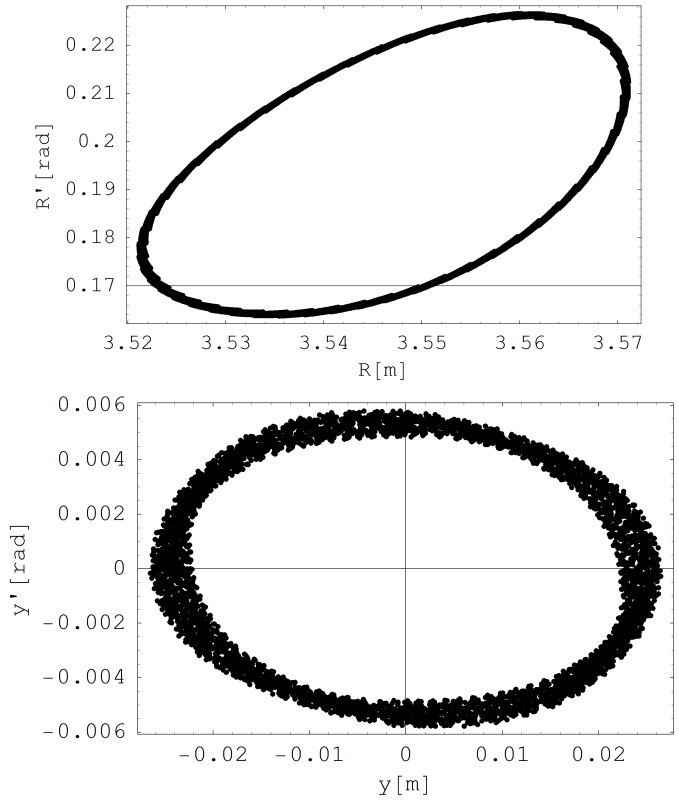

Figure 37: Dynamical acceptances calculated in tracking studies using 3D field map in the horizontal plane (left) and the vertical one (right).

2 Work Package 2: Infrastructure, Facilities and Costing

Work Package 2 (WP2) will provide a credible pathway, definition and costing for the delivery of the Infrastructure for ITRF. Over the first 12 months of PA1—the present Preliminary Activity aiming to produce a Conceptual Design Report for ITRF—the Project Team have developed a baseline layout and costing to inform the further definition of the facility and its design ready for the preparation of the Conceptual Design Report to be finalised at the end of PA1. The following sections describe the work that has been carried out in those 12 months.

2.1 Infrastructure

The building and technical infrastructure will require careful planning, design and implementation to ensure the facility delivers on its challenging scientific objectives and provides accommodation that inspires scientific research. The overall success of the facility requires an integrated approach for the high power laser, target, capture, matching and energy selection of ions, accelerator, end stations, control rooms, building, services, staff and user needs such as preparation laboratories, offices, meeting rooms and amenities that create a successful research environment.

To develop the requirements, planning and design, the needs of all stakeholders must be included from an early stage of the project to achieve the desired outcome. This section describes progress and status of the conceptual design of the building and its contents.

Particular attention must be paid at all stages of the design and construction of the building and technical infrastructure to ensure that the challenging performance of the facility can be achieved. The need for equipment stability will be crucial, involving the stringent control of vibration, floor stability and environment control in key areas. The vision is to construct a new purpose-built energy-efficient facility in terms of its design, construction, operation and decommissioning.

The facility concept design floor plan is shown in figure 38, that has been driven by the science requirements. Proton and ion beams are generated when a high-power Ti:Sapphire laser impacts on a target (see fuller discussion in Section 1). Just after the target, Gabor lenses capture and provide matching and energy selection of the proton or ion beams that are then delivered to the Stage 1 experimental areas. Particles are accelerated to the full energy (127 MeV protons or ion beams 34 MeV/u) needed for the Stage 2 experimental areas using a fixed-field alternating-gradient (FFA) accelerator that is injected from the Stage 1 plasma accelerator. Beam transport from the FFA to the in-vivo experiments is performed by a high-energy beamline.

There are three experimental end stations, each with a local control room; two end stations will be used for in-vitro experiments—shown in figure 39—which are located on the accelerator complex roof at the end of vertical beamlines. The low-energy in-vitro end station is served by 15 MeV protons. The second (high-energy) in-vitro end station and the in-vivo end station use the output of the Stage 2 FFA, which delivers either 15–127 MeV protons or carbon ions from 5–34 MeV/u. The in-vivo end station is located on the ground floor in Area 6. The in-vitro end stations are above the accelerator complex at the end of vertical beamlines, indicated on figure 38 and on figure 40.

The site plan has been estimated to be 72 m $\times$ 32 m of which 57 m $\times$ 32 m is the main building footprint next to a 15 m $\times$ 32 m fenced outside pen to locate the water cooling chillers, water storage tank, water pumping and transformers (figure 40). An approximate estimate for these systems has been conducted to inform the cost model, but more exact systems capacities will develop through the CDR and TDR phases of the project. The water cooling plant location has been chosen to be close to those heat exchangers and accelerator equipment with a high cooling load. Similarly, two transformers and the main electrical switchboard are located close to each other to reduce the length and cost of interconnecting cables. A 2.5 m wide access around the circumference of the accelerator is proposed to provide equipment access by fork lift.

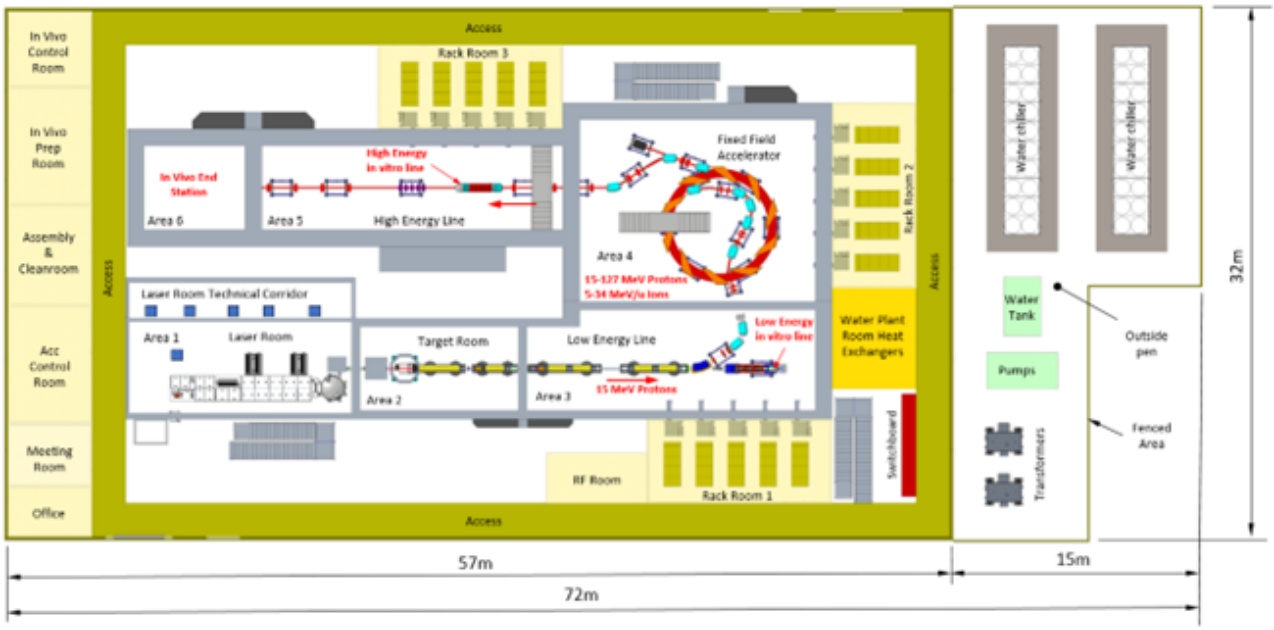

Figure 38: Facility ground floor plan.

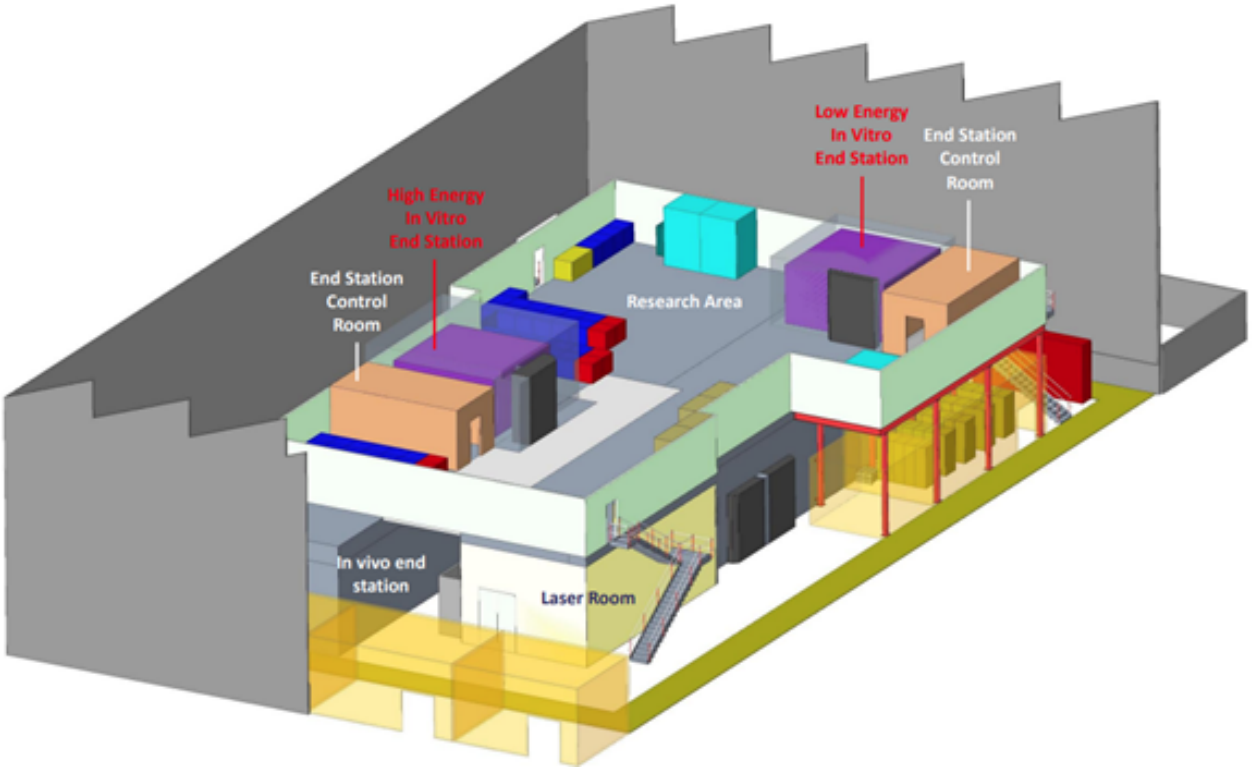

Figure 39: End stations and research area above the accelerator complex on the 1st floor.

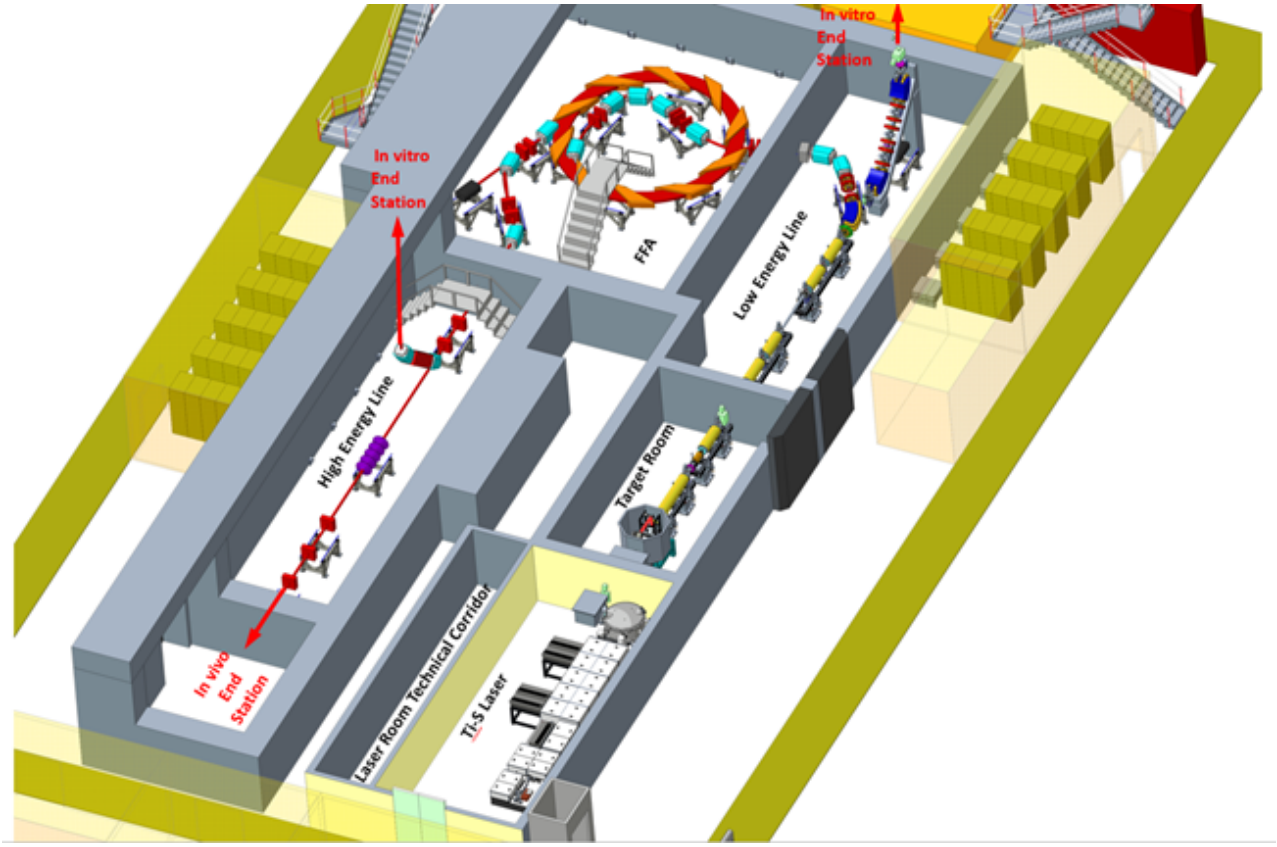

Figure 40: Accelerator complex with shielding cut away to schematically see equipment. The three end stations are indicated (red text).

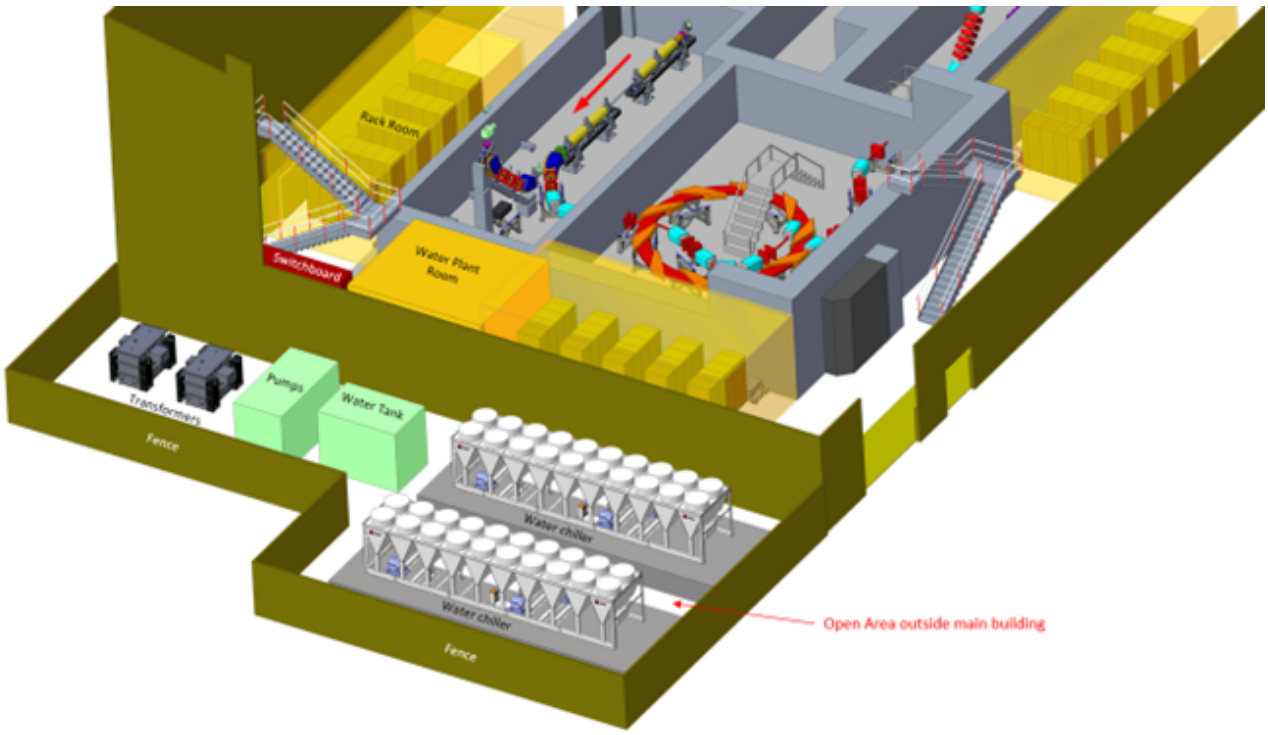

Figure 41: Water cooling plant and transformer(s) outside pen.

A cross section through the building is shown in figure 42. The overall height is estimated to be 14 m, which allows the installation of an overhead crane to install and decommission the facility. Lifting solutions will also be required inside the radiation enclosures for installation, maintenance and decommissioning. For installation, maintenance and decommissioning of the vertical beamlines, permanently-installed platforms next to the accelerator components are envisaged to provide a safe and efficient working environment. Sliding shield doors are shown in the figures, but labyrinth access will also be considered during the technical design stage of the facility.

A saw-tooth roof construction is proposed, comprising a series of ridges with dual pitches either side. The steeper surfaces at $\sim$70° are envisaged to have double-glazed windows to admit natural light. The shallower surfaces at $\sim$35° are proposed for the installation of solar panels facing south, to receive the most direct sunlight and energy gain.

Two sets of stairs and a lift are proposed for people and light equipment access. Heavy items may be lifted to the accelerator complex roof with the overhead crane.

For the accelerator systems shown on the ground floor, 60 power supply, control and instrumentation racks are currently estimated to be needed, as shown in the facility ground floor plan in figure 38 and table 12. The estimate will be updated as more detailed technical specification is generated. The racks will be located in three thermally-insulated air-conditioned rooms to minimise dust and to provide temperature control for the stability of the power supplies.

It is proposed that the laser room will contain an internal technical corridor to house power supplies to reduce the heat dissipation to the room, which has a stringent temperature stability requirement of 20–22°C to better than $\pm$1°C, monitored at less than 2 m from the optical tables. The laser room also requires humidity of 40–50% monitored at less than 2 m from the optical tables, and cleanliness to ISO 7 class [65].

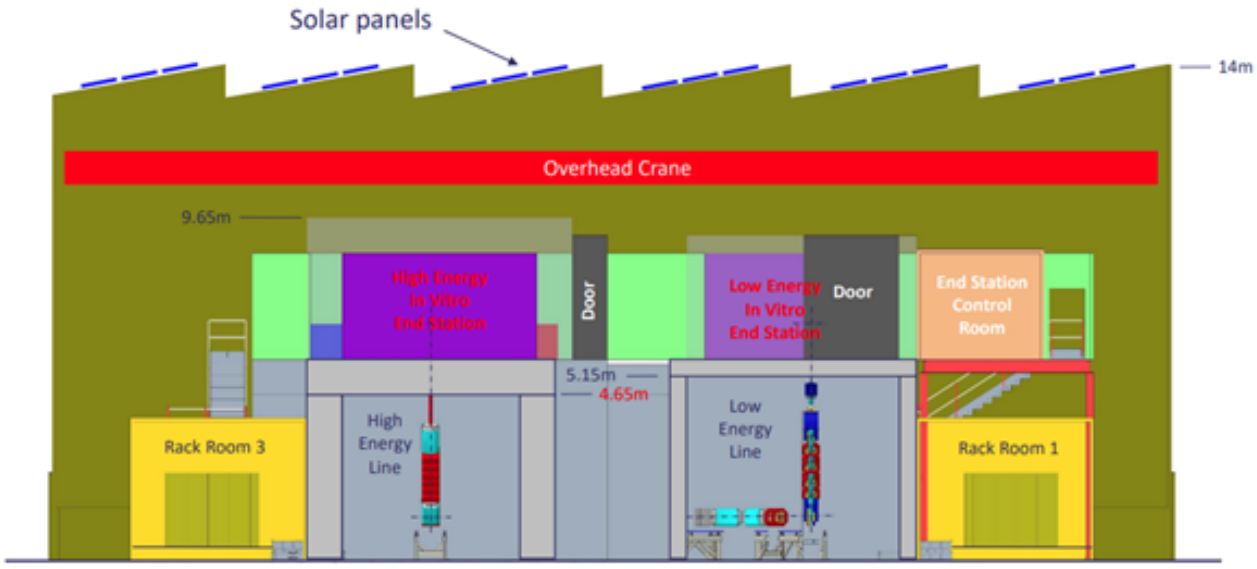

Figure 42: Cross section through the facility.

Table 12: Ground floor power supply, control and instrumentation rack rooms.

Parameter	**Equipment**	**No. of Racks**
1	Low Energy Line	20
2	Fixed Field Accelerator	20
3	High Energy Line and In Vivo End Station	20

Table 13: Laser room size.

Parameter	**Description**	**Size** m×m
1	100 TW laser room	13.3×5.5

2.2 Sustainability contributing to Net Zero by 2040

Sustainability aspects of the facility during the planning, design, construction, operation and decommissioning will be a crucial to the success of the project and contribute to the Green transformation for the UK science estate [66]. The UK Government has committed the nation to achieving so-called Net Zero emission by 2050, and this commitment is embodied in international agreements, legislation and policies. The Paris Agreement of COP21 commits the UK to reducing greenhouse gas emissions by at least 68% by 2030 (compared to 1990 levels). These targets are enshrined in UK Nationally Determined Contributions. The Climate Change Act (2008) sets legally-binding targets overseen by the Climate Change Committee. The UK Net Zero strategy (2021) lays out how emissions reductions will be achieved. These in turn determine policies for UK-funded research and infrastructure development that will, for example, include all future UKRI-funded infrastructures and research. Importantly, *STFC aims to reach Net Zero carbon emissions by 2040*, which is within the timescales of the ITRF facility operation. STFC's goals are laid out in the STFC Environmental Sustainability Action Plan, which includes an energy hierarchy framework to reduce its emissions burden. An accompanying Energy Roadmap and Decarbonisation Plan will be published toward the end of 2023. STFC is currently developing a suite of guidelines and methods for sustainable design, engineering, procurement and manufacture of its systems.

Technology choices to minimise materials use, power consumption and cooling requirements will be vital. Key examples of technology choices for the accelerator systems—that will reduce the carbon footprint of the facility both in construction and in operation—are the plasma lenses in the Stage 1 low-energy beamline and the fixed-field accelerator (FFA) that will be used to boost the energy in Stage 2. A geothermal groundwater cooling system is included in the cost model, that enables efficient heat transfer by recovering heat stored naturally in groundwater or aquifers; the facility cooling water will pass through heat pumps to yield its low grade heat before being returned to the aquifer at a lower temperature. Solar panels on a saw-tooth building roof design are also proposed (see figure 42).

Work is in progress to develop UKRI-STFC Sustainability Design Principles [67] that to date encompass:

- Cryogenics;
- Design for manufacture;
- Electrical;
- Sustainable radiation shielding; and
- Vacuum.

The ITRF building design included in the cost model complies with UKRI-STFC Sustainable Building Design Guide V3 [68] which adopts the RIBA Sustainable Outcomes Guide (RIBA, 2019) [69]. The RIBA Guide sets out eight key areas for sustainable performance and a clear process that must be followed for all building projects. By following the RIBA Sustainable Outcomes Guide, the sustainability approach aligns directly to the RIBA Plan of Work (2020) project stages [70]; the RIBA Plan of Work is an industry standard (first set out in 1963 but most recently updated in 2020) and is currently being used with all major new UKRI-STFC building projects. UKRI-STFC has also signed up to targets described in the RIBA 2030 Climate Challenge (RIBA, 2021).

These targets for building sustainability will be altered in future guideline iterations, but are adopted with the aim to achieve Net Zero by 2040. 'Net zero' for building is defined in the UK Government 'Net Zero Estate Playbook' [71] though only for energy in use; embodied carbon and whole-life carbon will be defined later. Due to the uncertainty in this topic, UKRI-STFC currently follows the following hierarchy of design:

- Reducing energy consumption through good design, especially a fabric-first approach and the selection of efficient plant and equipment;
- Installing low-carbon heating and ventilation options;
- Focus on control and benchmarking through a Building Management System to deliver and record continual improvement;

- Installation of renewable generation;
- Where suitable, use of bespoke and innovative technologies (e.g. heat and battery storage, demand-side management and artificial intelligence); and
- Achieving BREEAM [72] 'excellent' or better, as well as the specific targets set out in that standard.

The BREEAM standard is applicable to the building and its operational plant only, and excludes the impact of scientific equipment which will be considered separately. Work is underway within STFC to assess carbon emissions quantitatively during the construction and operation of accelerator facilities, and outcomes from that work will be reflected in future analyses of the emissions associated with the ITRF facility.

2.3 Radiation Safety

The Ionising Radiation Regulations 2017 (IRR17 [73]) requires employers to keep exposure to ionising radiations as low as reasonably practicable. Regulation 7 (IRR17) requires that *Consent* is granted by the Health and Safety Executive (HSE) to carry out specified practices, one of which is (IRR17 7.1.d) the *Consent* for the operation of an accelerator. The indicative list of information require to support an application for *Consent* includes:

1. Responsibilities and organisational arrangements for protection and safety;
2. Staff competences, including information and training;
3. Design features of the facility and of radiation sources;
4. Anticipated occupational and public exposures in normal operation;
5. Safety assessment of the activities and the facility in order to:
   a) Identify ways in which potential exposures or accidental and unintended medical exposures could occur;
   b) Estimate, to the extent practicable, the probabilities and magnitude of potential exposures;
   c) Assess the quality and extent of protection and safety provisions, including engineering features, as well as administrative procedures; and
   d) Define the operational limits and conditions of operation;
6. Emergency procedures;
7. Maintenance, testing, inspection and servicing so as to ensure that the radiation source and the facility continue to meet the design requirements, operational limits and conditions of operation throughout their lifetime;
8. Management of radioactive waste and arrangements for the disposal of such waste, in accordance with applicable regulatory requirements;
9. Management of disused sources; and
10. Quality assurance.

The accelerator complex on the ground floor is proposed to be divided into 6 areas to establish flexibility during the construction, maintenance and operation of the facility. By segregating the controlled areas shown in figure 38 and figure 39, access to downstream rooms will be possible when ion beams are present in the upstream controlled areas. This flexibility will allow the project construction duration to be significantly reduced, by allowing systems commissioning with beam and installation of downstream areas in parallel. An example is being able to operate the Stage 1 low-energy line while installing the Stage 2 fixed-field accelerator. Faster maintenance and checks are possible using individually searched areas by not having to search the full accelerator complex. To achieve that flexibility, radiation shutters will be required to cover each beam pipe aperture in the shielding dividing walls, the shutters interlocked to the access doors controlled within the personnel safety system.

The thickness of the bulk shielding shown in figure 38 and figure 39 has not yet been determined. A specialist company will perform a radiation study during Q1 and Q2 of 2024 that will contain the following activities:

Table 14: Facility room sizes.

Area	Description	Internal room size m×m
2	Target Room	9.4×5
3	Low energy line room	17×6
4	Fixed field accelerator room	14×10.8
5	High energy line room	18×5
6	In vivo end station	6×5
7	Low energy in vitro end station	5.5×5.5
8	High energy in vitro end station	5.5×5.5
9	Low energy in vitro end station control station	6.8×3.4
10	High energy in vitro end station control station	6.8×3.4

1. A high-level shielding design basis report that creates a point of reference for all the shielding protection calculations;
2. Radiological classification of areas;
3. Preliminary bulk shielding requirements;
4. Preliminary activation study (cooling water, environmental air and physical accelerator structure); and
5. Concrete sustainability appraisal.

Table 14 shows the ground floor accelerator complex room areas. The 100 TW laser room is specified to be constructed with thermally insulated panels.

Areas 2 to 8 form the radiation-shielded enclosures. To reduce the volume of concrete, the implementation of composite shielding is being considered. Composite shielding consists of a concrete skin filled with magnetite aggregate. Such a solution has been proposed for the CALA facility [74] based on previous constructions by Foster [9]. The construction technique provides significantly improved sustainability due to the reduction in the concrete that is required. A further development of this technique that is being considered would be to apply the composite approach to shielding blocks rather than in-situ casting of the concrete skin. Shielding blocks allow flexibility for cost-effective upgrades and simplification of staged installation and decommissioning. The ability to re-use shielding blocks many times on future facilities further improves sustainability and value for money after the lifetime of the proposed facility.

2.3.1 Designation of Areas

IRR17 [73] requires an area to be designated as a Controlled Radiation Area if a person entering that area is likely to receive an annual dose in excess of 6 mSv, or if they are required to follow special procedures intended to restrict their radiation dose or the effects of an accident. The radiation hazard inside the shielded enclosures will generally be negligible when they are not interlocked by the Personnel Safety system (although consideration must be given to components such as collimators and beam dumps which have the potential for high levels of induced activity after the ion beam has been switched off). Adopting the model used at similar facilities in designating areas, Areas 2 to 8 in table 14 will be designated as Controlled Radiation Areas on a permanent basis.

IRR17 defines a Supervised Radiation Area as one where it is necessary to keep the conditions of the area

under review to determine whether it should be designated as Controlled, or where a person is likely to receive an annual dose in excess of 1 mSv. It is therefore proposed that the surroundings of the accelerator complex are designated as Supervised Radiation Areas, at least for an initial period whilst environmental dose measurements are taken in the surrounding areas within the facility building.

2.3.2 Personnel Safety System

The Personnel Safety System will be similar to those in operation at the existing UKRI-STFC facilities in that it will be compliant with IRR17, STFC Safety Code SC40, and is implemented to achieve the required level of risk reduction.

The implementation of interlocks is a complex process that needs to ensure the system achieves adequate levels of risk reduction. Whether this is mechanical or electrical it still needs to follow an interlock lifecycle model to manage the process and ensure consistency in the management of similar safety systems. The implementation of interlocks requires consideration and planning of many aspects, covering a range of areas that are applicable throughout the lifecycle.

There are alternative methods available to comply with the requirements for implementation of interlocks within STFC Safety Code SC40, either:

1. A suitable recognised international standard that covers the lifecycle phases associated with, as a minimum, safety requirements allocation through to decommissioning:
   a) IEC 61508 [75] (or sub-standards, i.e. IEC 62061, IEC 61511, etc.); or
   b) ISO 13849 [76] (With the addition of an IMP, see section 3.5);
2. A process that is equivalent to or better than that detailed within the recognised international standards applicable to interlocks lifecycle implementation.

The application of electrical interlocks is the subject of extensive and detailed guidance and standards, referred to as Functional Safety. The general benchmark of good practice is IEC 61508: Functional safety of electrical/electronic/programmable electronic safety related systems. Functional safety is the accepted term applied to the part of the overall safety of a system that depends on the correct functioning of electrical, electronic and programmable electronic (E/E/PE) safety-related systems and other risk-reduction measures. This would include any mechanical interlocks that contribute to the overall safety of such a system.

IEC 61508 has been used as the basis for industry specific standards for functional safety such as:

- IEC 61511: process industry [77]; and
- IEC 62061: machinery [78].

Other standards exist that do not follow this model but are also commonly used and accepted as best practice in industry such as:

- ISO 138499 [76]: safety of machinery–safety-related parts of control systems.

As an extension to the implementation of functional safety, the use of the lifecycle model for the implementation of mechanical interlocks provides additional controls and consistency across the organisation.

STFC SHE Code 40 requires that a Risk Assessment as per STFC SHE Code 6 (Risk Management) has been carried out for the facility/system under consideration and that the following inputs are therefore available for that facility/system:

- The Concept;
- The Overall Scope Definition;
- A Hazard and Risk Analysis; and
- Overall Safety Requirements, to reduce risk to a level acceptable to STFC.

Overall Safety Requirements Allocation, in particular the extent to which the interlock system is required to contribute to the control of risk by reducing the probability of occurrence of the identified hazard(s).

2.4 Staged Construction

Site location has not yet been defined for the construction of the proposed facility, but it has been proposed that the facility may benefit from being built at a UKRI-STFC National Laboratory site to take advantage of existing facilities, multidisciplinary technical staff expertise, approved radiation site authorisation, and large electrical power capacity.

It is proposed that the construction of the facility be in 2 stages:

- Stage 1, providing beam to the low-energy in-vivo end station shown in figure 43 and figure 44, including:
  a) The full building size
  b) The full fenced outer pen to house the water cooling systems and transformer(s)
  c) Laser room
  d) Radiation shielding for areas 1 – 3 and low energy end station
  e) Laser, accelerator and end station technical systems for:
     – Laser-driven proton and ion source
     – Proton and ion capture section
     – Matching and energy selection section
     – Low energy abort line
     – Beam delivery to low-energy in-vitro end station
  f) 1st floor research area for Stage 1
  g) Low energy in vitro end station systems
  h) Low energy in vitro end station control room
  i) Rack room 1
  j) RF room
  k) Main switchboard
  l) Internal water plant room containing heat exchangers and pumping
  m) General technical services for the above described systems including electrical distribution, water cooling distribution, HVAC, compressed air and gases
  n) Accelerator control room, meeting room, cleanroom and general office.
  o) EPICs control system for above systems
  p) Personnel safety system
  q) Two sets of stairs and light duty equipment lift to Level 1.
- Stage 2, delivering the full functionality of the facility shown in figures 38, 39, and 40, including:
  a) Accelerator and end station technical systems for
     – Fixed field accelerator
     – High energy extract line
     – High energy abort line
     – Beam delivery to high-energy in vitro end station
     – Transfer line to the in-vivo end station
  b) Radiation shielding for; Areas 4 – 6, high energy in vitro end station and in vivo end station
  c) High energy in-vitro end station systems
  d) High energy in-vitro end station control room
  e) In-vivo end station
  f) In-vivo control room
  g) In-vivo experiments preparation room
  h) 1st floor research area rearrangement for Stage 2
  i) Rack room 2 and 3

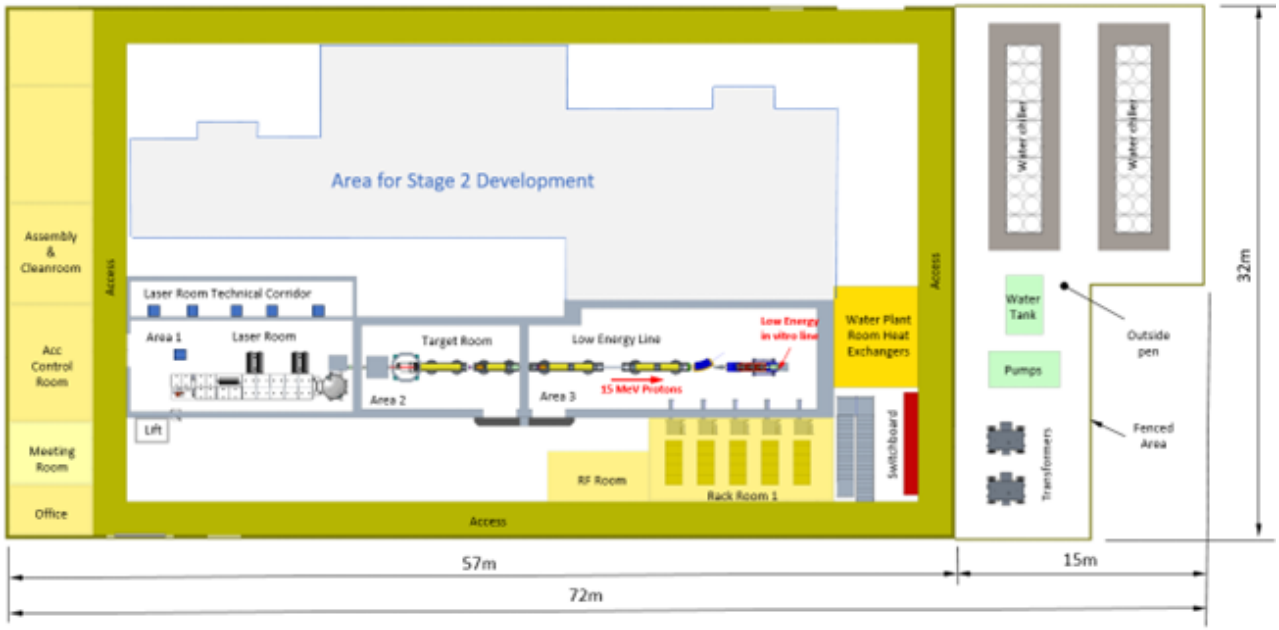

Figure 43: Stage 1 floor plan.

j) General technical services for the above described systems including electrical distribution, water cooling distribution, HVAC, compressed air and gases

k) EPICs control system for above systems

l) Upgrade to personnel safety system

m) Upgrade to accelerator control room

n) 3rd set of stairs to Level 1

2.5 Key Installation Milestones

The installation and commissioning of the ITRF systems will be coordinated so as to maximise the scientific output of ITRF. Thus, prior to the completion of construction, the goal will be to achieve the following scientific milestones:

Stage 1

- First demonstration of the capture of a laser-driven ion beam using a Gabor lens system;
- Demonstration of the energy selection capabilities of a Gabor lens system;
- Irradiation of cells with a laser-driven ion beam.

Stage 2

- Injection line to the FFA;
- Fixed Field Accelerator (FFA);
- Extraction line from the FFA and the transfer line to the in vivo end station;
- High energy in-vitro arc;
- High energy in-vitro end station;
- In-vivo end station.

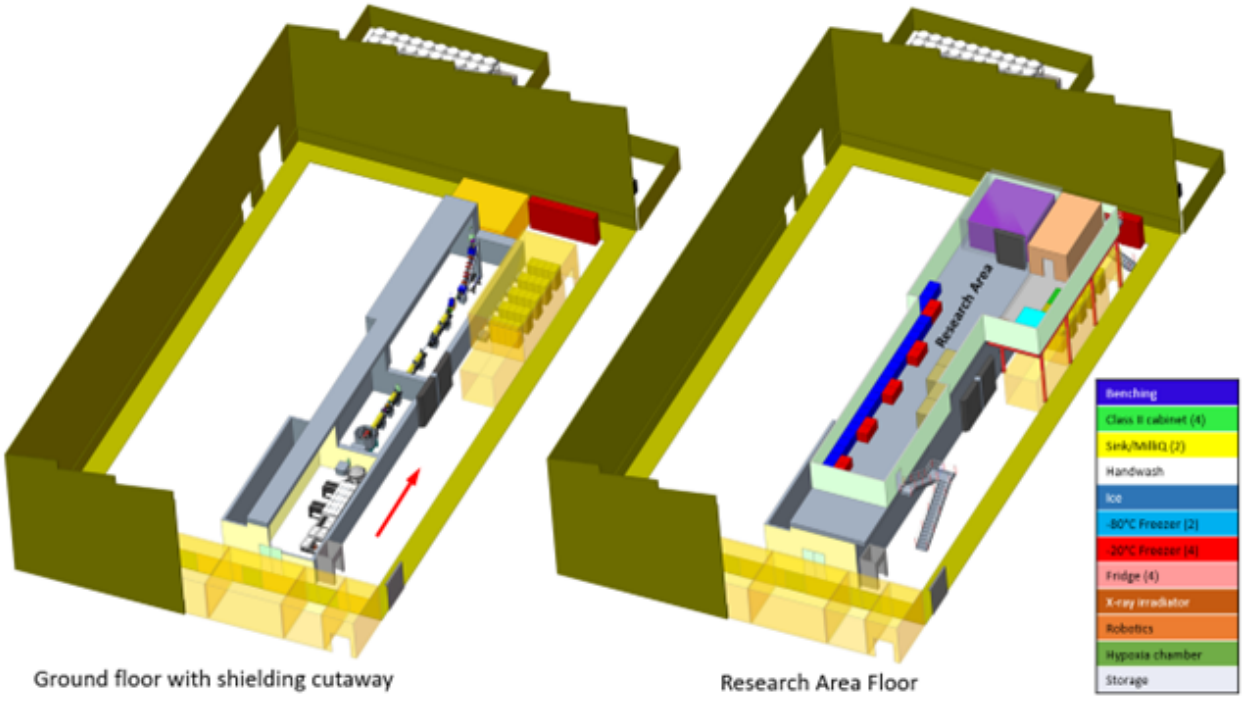

Figure 44: Stage 1 construction.

2.6 Stage 1 Engineering Concept

The engineering CAD model of the laser-driven ion source is in progress, as shown in figure 45. The CAD model representation of the 100 TW Ti:Sapphire laser and compressor chamber has been provided by Amplitude based on the Pulsar 140 system [12]. However, no decisions have been made on suppliers of equipment at this stage of the project. The laser equipment is shown supported by 2 optical tables (support modules M1 and M2) followed by a compressor chamber (module M3). Figure 46 shows a provisional representation of the target chamber internal components, which is a conceptual design to be developed over the next 18 months. A motorised vacuum valve has been introduced as an integral part of the nozzle assembly. The valve will allow the low-energy line vacuum region to be isolated from the target chamber vacuum region when the low-energy line is not in use, thereby minimising the risk of contamination of the downstream vacuum regions. Both horizontal and vertical laser-beam configurations have been studied. The vertical configuration, as shown, provides the best access and visibility around the target area. An idea being considered is to mount the 3^{rd} and 4^{th} optic in the chamber on a linear slide to create room between the target and the nozzle when operating at low energy to image the beam from the rear of the tape drive with a camera. The linear slide system would also create additional space for larger target configurations—not yet designed.

Modules labelled M4–M8 are independent support systems, and will be assembled, surveyed and tested prior to installation in the accelerator complex. Power supply, control and instrumentation racks will also be cabled to the modules in the pre-installation assembly area to test the racks and the control system. This proven methodology will solve as many technical issues as possible prior to installation, thus reducing the time taken for installation. Support, alignment and vacuum systems design is based on previous UKRI-STFC facilities. Module M9 is a representation of the 45° girder assembly. Permanently-installed working platforms next to module M9 are envisaged to provide safe and efficient working at height. Internal craneage will also be required in some areas.

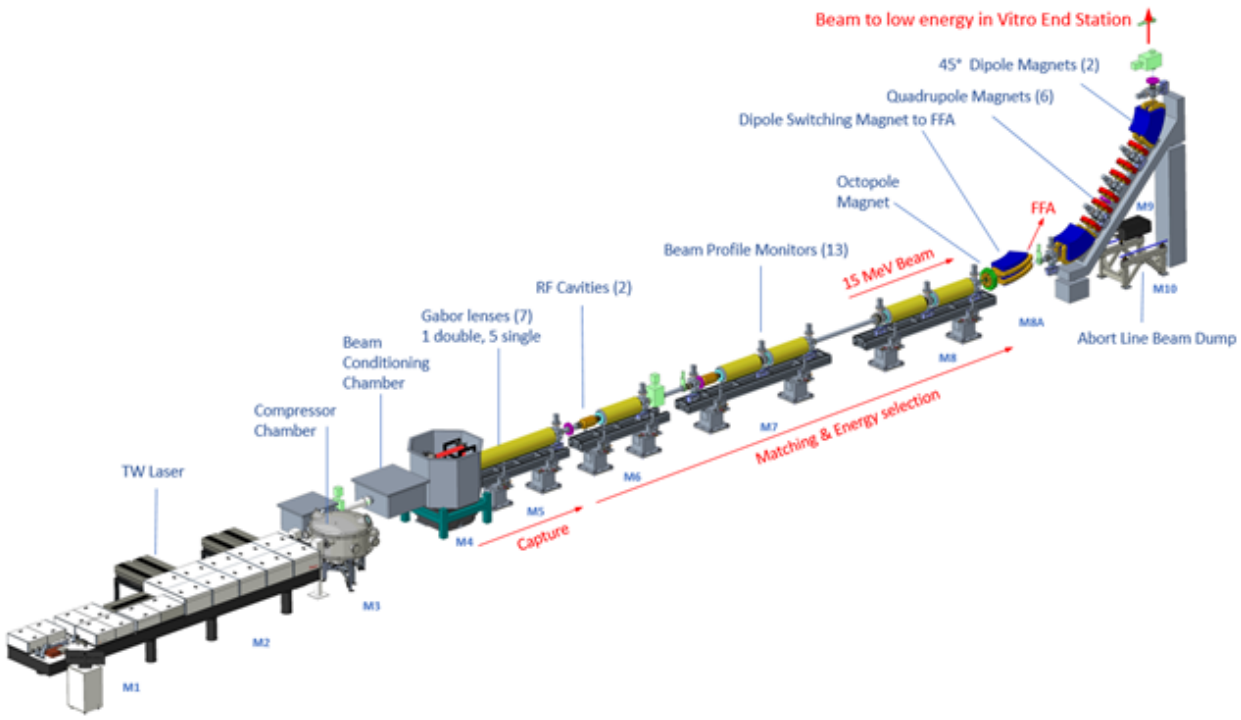

Figure 45: Stage 1 engineering concept design.

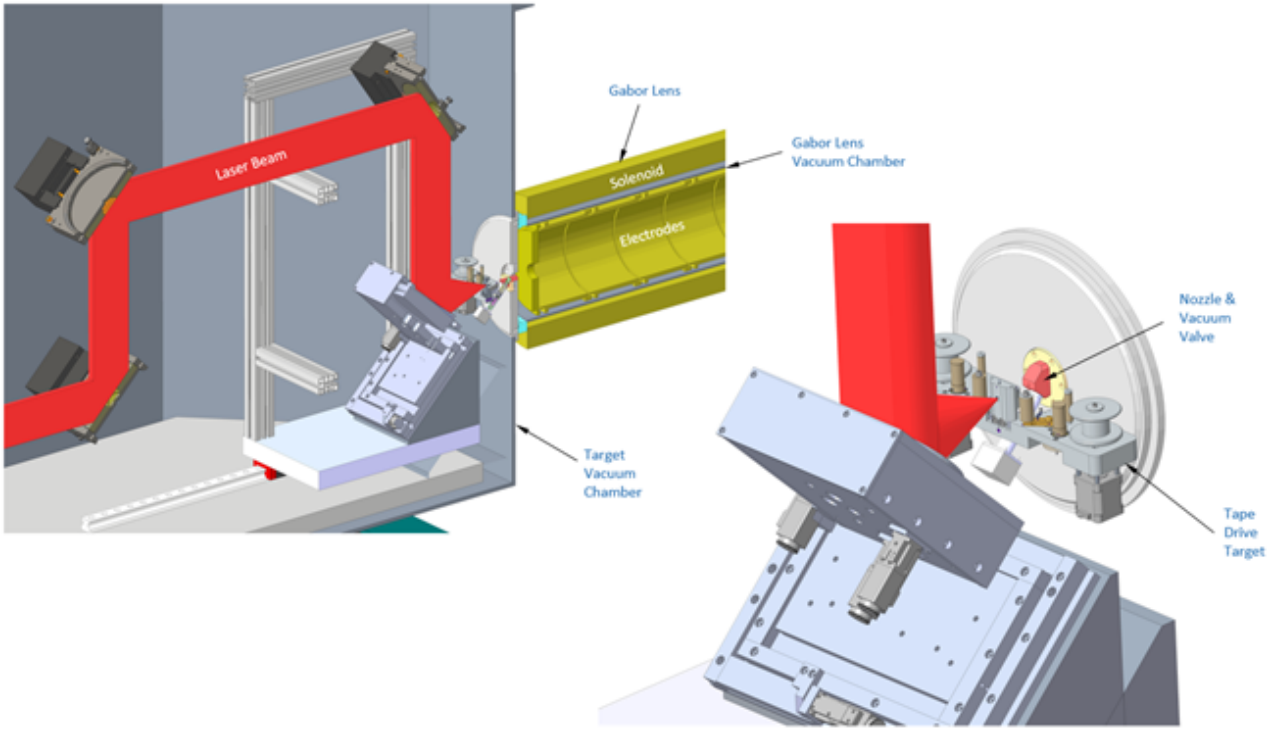

Figure 46: Concept design of the Target, Conductance Nozzle and 1st Gabor Lens.

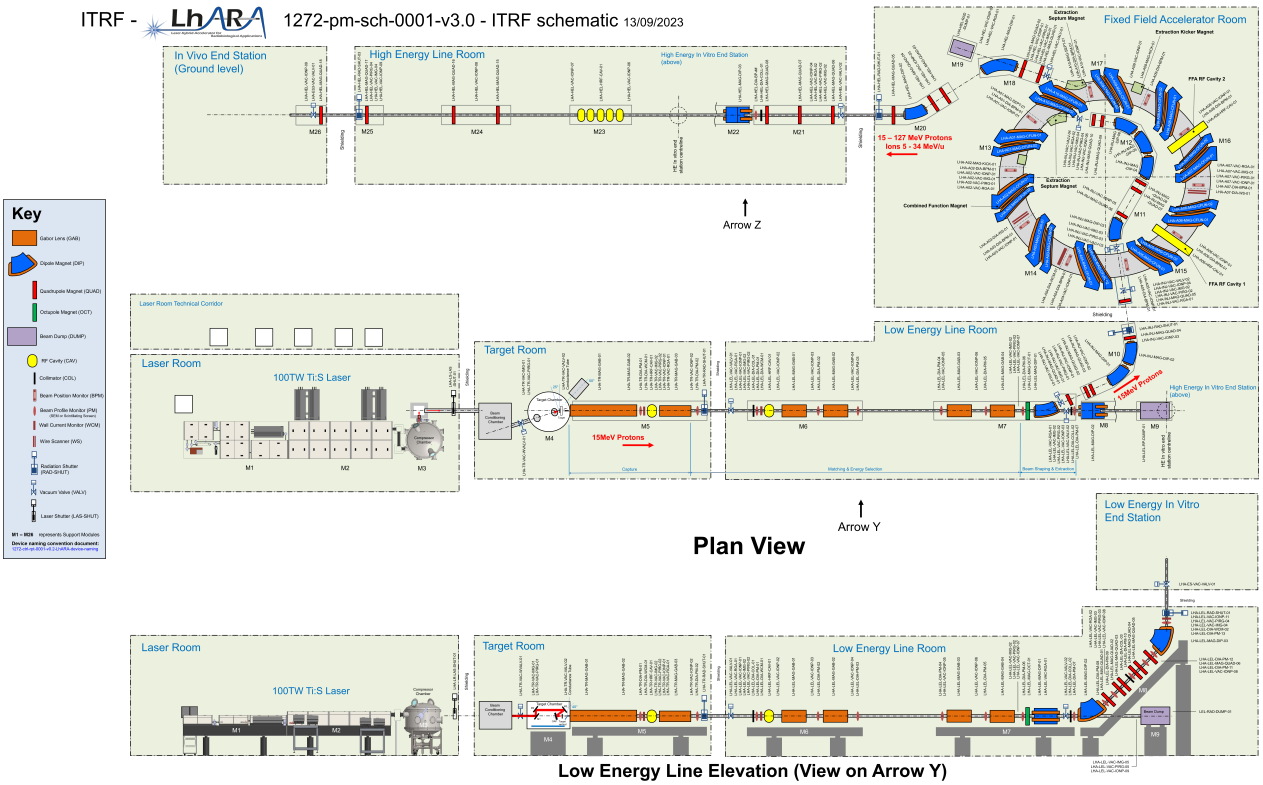

Figure 47: Schematic diagram of the facility equipment.

2.7 Schematic Diagram

A draft schematic diagram of the facility is shown in figure 47. A large format version with clearer visualisation of the required components is available [79]. A draft device naming convention has been established [80]. The device naming convention has the following benefits:

- Every device on the facility has a unique name;
- Names are used in an appropriate and consistent way;
- Duplicate names can be avoided;
- The function of a device can be derived from its name (and vice-versa); and
- Consistency with good practice adopted on previous accelerators constructed and operated successfully.

For these reasons it is proposed to introduce a formal device naming convention on the ITRF Control System. It is anticipated that the names will be used on the facility schematic, engineering drawings, in technical documents, control system display panels and in informal and formal discussions. The plan is to develop the schematic throughout the Conceptual Design Phase to capture all the equipment required that will inform the CAD model, cost model and schedule development.

2.8 Vacuum System

2.8.1 Introduction

The vacuum system of the ITRF project can be divided into a number of vacuum regions that require different vacuum specifications. In general, however, the design is based upon the extensive experience of the design team in delivering successful vacuum systems for facilities such as Diamond Light Source and ALICE, EMMA and CLARA at UKRI-STFC Daresbury Laboratory.

Table 15: Mean working pressure for each vacuum region.

Subsystem	Mean working pressure (mbar)
Laser systems	TBC
Laser beam conditioning chamber	TBC
Target chamber	1×10^{-6}
Gabor lenses	1×10^{-8}
Low energy line	1×10^{-8}
Low energy in vitro end station	TBC
Fixed field accelerator	1×10^{-9}
High energy line	1×10^{-8}
High energy in vitro end station	TBC
High energy in vivo end station	TBC

The range of vacuum requirements falls comfortably in the ultra-high vacuum (UHV) region and therefore the general design principles for this vacuum regime will be adopted. The Vacuum Quality Assurance Documents used at Daresbury Laboratory, developed for modern accelerator applications, provide a good example of design principles that can be adopted for ITRF.

As this project will involve a number of different partners it is essential that integration of the vacuum systems, delivered by the partners, is carefully addressed. This function has been identified and will be the role of a specific work package for integration of the whole project including vacuum systems.

Key vacuum challenges for ITRF include:

- Achieving low pressure without extensive in-situ bakeout;
- Maintaining a contamination free environment, including some particle controls, particularly in the region of the RF cavities;
- Providing sufficient differential pumping where vacuum specifications vary by more than one order of magnitude between sections; and
- Providing sufficient pumping for conductance limited beam pipes.

2.8.2 General Design Objectives

In any accelerator based project, it is inevitable that detailed consideration of the vacuum system comes some way down the line of the design process. The major reason for this is that a relatively detailed understanding of the mechanical layout of the machine and of the design of individual vacuum vessels and components are required before any final analysis of the pumping requirements can be made. At this stage in the ITRF design there are some areas where more detailed engineering is still required to finalise the conceptual design, this may result in some adjustments to the vacuum system but these are not expected to be significant.

Number density plays an important role in two general types of process, viz., scattering and ionisation, and impact rate on surfaces. LhARA, the basic accelerator system, can be considered as a single-pass machine and therefore a modest number density of gas molecules inside the vacuum envelope can be tolerated. Typically pressures in the region of 1×10^{-8} mbar are expected to be sufficient to meet both the accelerator physics and engineering requirements. Vacuum requirements in the RF cavities are more stringent and will be considered

separately. Although the pressure levels are generally quite modest, cleanliness criteria will still be stringent and will follow standard UHV practice.

It is recommended that all components receive a full UHV cleaning procedure followed by a vacuum bake to 250°C for 24 hours before installation (*ex-situ*) where possible. Differential pumping will be required to minimise gas and debris transfer between the laser target and the 1st Gabor lens.

2.8.3 Vacuum System Design Principles

General

In general, the vacuum system design of ITRF is based on well-tried and well understood design principles. It is not a particularly demanding design, except for the target/Gabor lens differential pumping section.

Knife-edge sealing is the default standard for bakeable vacuum systems of the type required for ITRF. However, in recent times, the reliability of EVAC seals has been proven on a number of machines and it may be that their compact size could be an advantage in some areas, which will be determined during the technical design stage of the project.

To ensure that all vacuum equipment is compatible with each region of the accelerator complex it is important that flange connections are clearly specified. Unless otherwise specified all vacuum equipment specified will be the ConFlat^{TM} Flange (CF) for connecting to the vacuum system. This is the most common type of flange connection for ultra-high vacuum systems and uses the knife-edge principle to achieve an all-metal vacuum seal.

Vacuum Pumping

It is expected that ITRF will be conductance-limited in most places, which will limit the pressures that can be achieved in the machine using a reasonable number of vacuum pumps. As usual, a number of iterations of machine layout and calculation of pressure distributions will be required before a satisfactory final scheme of vacuum pumping can be determined. At this stage an estimate has been made based upon previous experience. It is anticipated that at most the position of pumps may need to be modified to meet the vacuum specification.

Since the whole machine is sensitive to hydrocarbon contamination to a greater or lesser degree, rough pumping will not use any oil-sealed pumps. Pre-pumping will use proven scroll pumps for a good balance of pumping throughput and costs, and high vacuum pumping will use clean turbomolecular pumps. These pump sets will be mounted on roughing carts that can be moved into position when required.

Main UHV pumping will be by sputter ion pumps, supplemented by NEG cartridge pumps if required in critical areas. The ion-pump power supplies will be located in rack rooms outside the accelerator complex. To reduce costs, power supplies with multiple outlets will be used. The disadvantage of this approach is that the pressure indication for each individual pump is compromised such that it cannot be relied upon as a true indication of pressure. However, this approach reduces costs significantly and has been used successfully elsewhere.

Pressure Measurement

Adequate pressure measurement performance will be obtained by using Pirani Gauges and Inverted Magnetron Gauges supplemented by information from ion-pump power supplies and residual-gas analysers (RGAs). RGAs will be placed at a few strategic locations throughout the accelerator complex. Otherwise, RGA facilities will be mounted on the mobile roughing carts, where they will be used mainly for leak testing and monitoring of initial cleanliness of the systems.

The total pressure gauge controllers will be located in the rack rooms outside of the accelerator complex, and therefore long cables will be required to connect these to the gauge heads; the correct specification of cable will be specified for this purpose to minimise noise and interference of the gauge operation.

For the residual gas analysers, the main electronic unit will be located close to the analyser head but sufficiently decoupled (via an RF cable extender) to avoid unwanted radiation damage or high magnetic fields.

Valves

Gate valves are required to provide sectorisation of the complete LhARA vacuum system for practical reasons and for machine protection. Dividing the machine into discrete vacuum regions makes it easier to install and commission whilst at the same time simplifying maintenance and breakdown interventions. At the same time it is important to keep the number of gate valves at a minimum to reduce costs. In most circumstances gate valves will be all-metal. Roughing valves (right angled valves) and let up valves will be located in each vacuum region. These will be an all-metal construction and for pump-down will be sized as DN63.

Bakeout

It is likely that most of the machine will not be baked in-situ, although all the vacuum chambers of the machine will be baked prior to installation as part of the conditioning and cleaning process, unless there is a special component that cannot be baked. However, the system is designed such that in-situ bakeout may be used if necessary such as to improve vacuum levels after interventions that can only be solved by an in-situ bake.

Vacuum Control System

A full system of vacuum controls will be installed on LhARA, providing monitoring, automation, alarms and safety protection.

2.9 Control System

2.9.1 Introduction

The control system plays a central role in all accelerator facilities. The ITRF control system will be a facility-wide monitoring and control system integrating all parts of the ITRF facility. The control system will extend from the interface of the equipment being controlled in the technical sub-systems through to the operator, engineering expert or physicist. It will include all hardware and software between these bounds including computer systems, networking, hardware interfaces, programmable logic controllers (PLCs) and fieldbuses.

The Personnel Safety System (PSS) will be interfaced to, and monitored by, the ITRF control system. Timing and synchronisation of the lasers and RF systems is covered in other sections and is not considered to be part of the control system. A separate event synchronisation system will be implemented as part of the control system to ensure synchronisation of technical sub-systems and critical control operations and will also provide a common high resolution time-stamping and/or pulse numbering capability.

The ITRF control system will benefit from existing control system equipment standards and knowledge gained from recently-implemented STFC facilities e.g. CLARA, RAL Space Satellite Test Chambers. Consideration has been made for where technology has progressed e.g. new, more appropriate fieldbuses or protocols will be implemented.

2.9.2 Architecture

The ITRF control system will be implemented using the EPICS [15] software toolkit. EPICS is a proven software toolkit with well-defined interfaces at both the client and server and will enable fast integration and development. Due to its collaborative nature, using EPICS enables us to take advantage of work done at other laboratories. EPICS has been successfully applied on previous projects at Daresbury including the ALICE, EMMA, VELA and CLARA facilities and on many accelerator projects worldwide. For these previous Daresbury projects extensive use has been made of EPICS Version 3 and more recently EPICS Version 7. For ITRF we aim to deploy Version 7 and use the advanced features exposed via the pvAccess protocol including manipulation and transport of structured data over the network.

The various components of the control system will be connected to a high speed Ethernet local area network. This will consist of several class C subnets connected to the main site network. Access will be provided to the control system data via EPICS gateway systems running access security. The hardware interface layer of the control system will provide the connection to the underlying sub-systems. This will consist of a modular hardware solution of commercial rack mount PCs and embedded systems running the Linux operating system, real-time where required, connected to a range of I/O types directly or via selected fieldbuses.

Application software will be installed on central file servers to ensure consistent operation from any console on the control-system network. The control system will be implemented in such a way that it can be incrementally expanded and upgraded as the project proceeds. The control system must be able to be extended to new hardware and software technology during the project phase and later. A number of EPICS client interfaces will be supported for controls and physics application development in high-level languages. This is likely to include both Channel Access and "pvAccess" interfaces for languages such as C#/VB via .NET, Matlab, Mathematica and Python.

2.9.3 Controls Hardware

The network hardware and commercial PC hardware of the ITRF control system will use standards defined by the STFC Digital Infrastructure Department. As far as possible, controls hardware used on recent ASTeC Radiation Test Facilities should be preferred to take advantage of existing expertise and proven hardware standards. This hardware includes:

- *Industrial rack mount PC systems running a Linux operating system, with potential for a real-time kernel, as required*: Existing EPICS support is available for interfacing many I/O types including analogue, digital and serial (RS232/422/485) along with status/interlocking via Ethernet-connected Programmable Logic Controllers.
- *Omron NJ series PLCs*: Status and interlock systems for digital control and machine protection of accelerator hardware and sub-systems. As a replacement for Omron CJ series PLCs deployed on previous ASTeC RTFs, the NJ PLCs will either be integrated directly into the EPICS control system using the CIP protocol, or indirectly via a data aggregation tool with EPICS integration via OPC-UA or similar. This will allow PLC data tags to be directly mapped to EPICS process variables and/or to pvAccess structured data types.
- *Motion control systems*: Fieldbus-based systems with remote I/O via EtherCAT. In common with CLARA, and building on that experience, these will comprise Beckhoff TwinCAT real-time controllers with EtherCAT connected motion control and I/O modules. These controllers interface with the EPICS control system via Modbus TCP.

Any specialist control requirements would be solved using dedicated real-time controllers (for example embedded industrial hardware or FPGA based). Examples of such systems could include geographically isolated devices or systems that require the computing speed of a dedicated CPU. Any dedicated controllers would be integrated into the EPICS environment and software build processes.

For any sub-systems that demand fast or beam-synchronous data acquisition, dedicated real-time systems will be required to satisfy these requirements. Likely applications include data acquisition for beam diagnostic measurements or RF system measurements. For previous ASTeC RTF control systems, VMEbus processors and FPGA based I/O carriers were used. For ITRF it is expected that modular, open standard, MicroTCA will be adopted as a replacement for VMEbus. Options for embedded MicroTCA controllers and FPGA carriers will be evaluated further in the Technical Design phase.

2.9.4 Virtualisation

Virtualisation technology will be used both in the server infrastructure layer and, where appropriate, in the EPICS input/output controllers. This will increase flexibility, scalability, reliability and efficiency of the control system by abstracting hardware specifics from the controls software.

2.9.5 Timing and Synchronisation System

One of the principle challenges with a network distributed control system is the synchronisation and accurate time-stamping or pulse numbering of events spread across several physically and logically separated systems. An example of this is the simultaneous measurement of beam diagnostic information along an entire beam transport system. This operation will typically involve collecting beam-synchronous data simultaneously from a number of front-end server systems.

Commercially available synchronisation hardware, as used on CLARA (Micro-Research Finland), is available for a number of platforms and provides timing outputs with a sufficient resolution for ITRF applications. The system will differ from CLARA in that MicroTCA form-factor will be preferred over VMEbus. The MicroTCA timing hardware is protocol-compatible with VMEbus and similar performance to the CLARA timing system will be expected.

It will be important to ensure that the master clock used by the timing system is locked to the RF and laser systems of ITRF. GPS atomic clock synchronisation will be used to distribute accurate time via the timing system and can also be used to discipline the RF master oscillator.

2.9.6 Interlock Systems

The control system will provide a comprehensive interlock and machine protection system ranging from the enforcement of sensible operating limits right through to the protection of the facility against potentially dangerous operating conditions.

High Integrity:
If and where required, this will be used to provide high-speed and fail-safe local protection in situations where serious damage to equipment is likely to occur. Embedded micro-controllers could be used for this purpose.

Routine:
This level of protection is intended to prevent minor damage to individual machine components or sub-systems. An Omron PLC based interlock system based on the system from the CLARA facility will be used for this purpose. Both interlock systems will operate independently of EPICS with monitoring and control requests marshalled to the interlock systems via EPICS for processing via internally programmed logic. In addition, but not described here, there will also be local systems that supervise individual components such as RF structures.

Personnel Safety System:
This section does not cover details of the protection of personnel from facility hazards. In terms of logic implementation, the PSS would be implemented in a similar way to other ASTeC RTFs, making use of Omron safety controllers. The Omron NX series safety controllers are now preferred over the NE1A controller used for CLARA and other RTFs. The NX controllers make use of Ethernet based safety protocols and are more suited to a new facility, easing installation and enabling greater scalability and flexibility. Full monitoring of the PSS will be provided through the control system.

2.9.7 Feedback Systems

Digital feedback will be required in a number of places on ITRF. The primary requirements include closed-loop control of amplitude/phase in RF systems and water cooling for high-power RF infrastructure and accelerating cavities.

For slow feedback control e.g. water temperature stabilisation, this shall either be implemented in a commercially-supplied system, or within the control system via PLC or EPICS PID control. In the case of commercial systems, they should ideally support integration into the control system to allow remote monitoring and control of the process.

For faster, lower-latency feedback control, this will be integrated directly into the control system. In the case of RF amplitude/phase control, this shall be done either by embedding the control directly into the FPGA of the LLRF controller or by dedicated software directly on the CPU of the LLRF controller. For high repetition rates, the FPGA option will be required. Options for embedded feedback control will be evaluated further in the Technical Design phase.

2.9.8 High-level Application Software

For operation of the ITRF facility, high-level physics applications are required that will communicate with the facility via the control system. To abstract away the detailed implementation of devices in the control system, a mid-level interface is required. This allows operators and physicists to interact with sub-systems and devices in a consistent, structured and well-defined way. This also allows for automation of routine or complex tasks which will provide consistent and repeatable setup/operation of the facility. For CLARA, a common C++/Python middle-level-interface to the control system was developed: CATAP ('Controls Abstraction To Accelerator Physics'). For ITRF this interface will be replaced with a pvAccess interface using EPICS Version 7 to represent sub-systems and devices as consistent, structured data for direct consumption by high-level application software.

2.10 Electrical Engineering

2.10.1 Electrical Equipment and Services

There are 3 rack rooms proposed to be positioned around the accelerator, each capable of housing 20 standard racks; this even distribution of racks and the numerous local labyrinths minimises the cable lengths, improves energy efficiency and simplifies installation. The location of some equipment is restricted by cable length—such as motion control and laser auxiliaries—so their position will need to be allocated accordingly. The labyrinth design should consider cable routes inside the accelerator and ensure personnel access isn't affected; a possible alternative is to consider high-level cable management.

Although the overall estimated number of racks is 73, the available space in the rack rooms will remain fixed at 60 as it is anticipated that around 20 of the racks will be housed near to specialist equipment. These include 4 racks associated with the laser—which needs a dedicated auxiliary room—and the 9 racks for RF systems that will probably be located in an accelerator or RF room. Pulsed power units are expected to be positioned next to the pulsed magnets themselves, to minimise design complexity.

Each rack room will house DC magnet power converter, vacuum, diagnostics, motion control, personnel safety and network equipment. It is envisaged that these rooms will be temperature-controlled at $\pm 1^{\circ}$ C, as this will assist reliable and stable operation. The racks will be mounted on support frames providing a minimum of 300 mm clearance to install cable management. A floating floor will enable easy access to rack equipment and allow the air conditioning to be channelled under the floor and up through the racks, ensuring effective cooling.

The number of racks estimated to be needed for the low-energy line is dominated by the solenoid power converters, with an equivalent space of 2 standard racks needed to accommodate each of the 90 kW converters. However, if these are replaced by Gabor lenses, then there will be a significant saving on power consumption and rack quantities. It is important to note that the power requirements given below are the installed capacity assuming maximum powering of all systems; this will not occur during operation, and the average power of the accelerator will be significantly lower; the average power consumption of the facility will be determined later and included in the final Conceptual Design Report. The size of the low-energy rack room may need to be increased to house these large solenoid power converters, and rack positions will be dictated by restricted cable length and the substantial size of the magnet cables.

The energy efficiency of the power converters will dictate the rack layout and the heat loading within the rooms. It is highly likely that water cooling will be necessary. The physical size of the FFA and high-energy rack rooms will probably need to increase if the power levels estimated for the magnet power converters are confirmed. The magnet ratings have been scaled from existing magnet designs, with specific reference to similar medical accelerators. The performance of the magnet power converters has not yet been assessed, but it is assumed that the required stability, reproducibility and resolution can be achievable using standard commercially-available units. If degaussing or bipolar operation is specified this will increase the physical size of units and introduce additional cost and technical complexity.

The specification of the pulse power converters of the FFA will be a challenge due to the small circumference (and hence short orbit time) of the accelerator. The low-energy injection septum and kicker power converters should be feasible, although the effects on the circulating particle bunches must be minimised. The fall time of the kicker could be critical to ensure the magnetic field does not affect the circulating bunches, but the low energy will reduce the nominal current required. The rating for the extraction septum and kicker will need to be assessed and optimised, as this could introduce a significant challenge given the extraction energy, circumference and the extraction angle. If the kicker needs to be fully energised within the time taken for the beam to complete one orbit, the current in the magnet will need to reach its nominal value within approximately 5 ns. Once the pulse power converter specifications are developed, a review of existing pulse-power technology can be initiated, as this could impact on the final lattice design.

2.10.2 Electrical Distribution

The estimated total peak power consumption for the facility is 3.5 MW, which is comparable with other research medical and clinical accelerators of similar energy. The average power consumption will be determined later, and is likely to be significantly smaller; the average powering will also significantly influence the carbon budget of the facility. Given the predicted power consumption, ideally the chosen location for the facility will need to have an existing high-voltage (HV) sub-station with sufficient spare capacity. However, it is possible to locate the facility on a green field site, but a substantial increase in building cost will be incurred.

The facility will need to be supplied by at least two transformers (for cost purposes), each rated at 2.5 MVA. Although each transformer is not sufficiently rated to provide the total estimated power consumption, there will be enough capacity to operate at the reduced values indicated above. Fault analysis and maintenance is an important consideration when designing the distribution scheme, along with segregation of supplies and conducted harmonics. The electrical infrastructure should mitigate these factors, by increasing the number of transformers to offer a minimum of $n + 1$ redundancy; this means potentially installing 3 transformers rated at 2 MVA, with any 2 transformers capable of supporting the entire facility. There must be dual HV incoming supplies connected to local HV ring-main units, with each one feeding a transformer. This philosophy should be cascaded throughout the low-voltage (LV) distribution to ensure that the failure of one circuit does not result in prolonged periods of downtime.

The ITRF will have numerous non-sinusoidal loads such as DC magnet power converters, RF modulators

Table 16: Estimated maximum power consumption and rack quantities; average power loading during operation will be much lower. The figures given here also assume the use of solenoids in the capture line (Line 4 of the table above). Adoption of Gabor lenses would instead give a peak power consumption of 30 kW per lens, or 210 kW in total (for 7 lenses), therefore significantly reducing the overall power requirements of the facility.

	Technical Equipment	**No of racks**	**Power/rack kW**	**Total load kW**	**Water cooled kW**	**HVAC kW**
1	Laser	4	12	48	31	17
2	Target	4	2	8	0	8
3	Radio Frequency	5	n/a	186	170	16
4	Solenoid Lenses	14	n/a	658	592	66
5	Pulse Power	4	n/a	14	0	14
6	Power Converters (Magnets)	12	n/a	1411	1270	141
	Controls and Instrumentation					
7	Laser	n/a	n/a	0		0
8	Vacuum	6	2	12		12
9	Diagnostics	9	1	9		9
10	Personnel Safety	3	1	3		3
11	Network/Control	3	1	3		3
12	RF Control and Auxiliaries	3	2	6		6
13	Motion Control	6	2	12		12
14	End Stations	n/a	n/a			
	Total Racks and Power (kW)	72		2370		
	Services					
15	Lighting			10		10
16	Climate Control			133		
17	Chiller System			825		
18	Water Pumps			72		
19	Compressed Air			50		
20	Offices/Laboratories			15		15
	Total Ancillary Load (kW)			1105		
	Total Power (kW)			3475	2063	332

and ion pump power supplies. The harmonic currents generated from such equipment can have an adverse effect on other equipment connected to the distribution system. Ideally any issues from this should be dealt with at the equipment level but it is often overlooked, and an accumulated effect can occur when many devices are connected to the same network. Wherever the facility is built, existing harmonic levels will need to be measured and included in any calculations to ensure compliance with legislation.

Segregation of the mains supply is important to experimental performance, as some equipment will cause electrical disturbance: this can be due to harmonics, sudden changes to load demand, and inrush currents. The point of common coupling between these systems and the sensitive equipment becomes critical and should be considered when designing the electrical infrastructure.

2.10.3 Earthing Arrangements

The earthing (or grounding) scheme proposed for ITRF must guarantee the correct operation of power converters, vacuum systems, diagnostic instruments and motion control equipment, and also ensure compliance with safety and EMC requirements from applicable standards.

The primary goal of an earthing system is to ensure personnel safety and protection of installations against damage. Two critical phenomena are lightning and power system faults. These can give rise to the circulation of large currents, which might create hazardous voltages in installation structures. The task of the earthing system—in these conditions—is to be a path to the earth for currents, while maintaining minimum voltage differences between any two points of the installation.

The secondary goal of an earthing system is to serve as a common voltage reference and to contribute to the mitigation of electrical disturbances in installations with sensitive and interconnected electronic and electrical systems.

This facility is expected to generate conducted noise at the following frequencies:

- Mains frequency (50 Hz) and multiples of this frequency due to non-linear loads, which make use of uncontrolled rectifiers to convert from AC to DC. There are many examples of sources of noise at these frequencies, which include:
  - All devices that contain a switch-mode power supply;
  - Uninterruptible power supplies; and
  - Inverters for AC motors or pumps.
- High frequency (1kHz to 100 kHz): coming mainly from magnet power converters, and RF system capacitor chargers, due to switching within the converter.

Radiated noise is also expected throughout the RF spectrum emanating from equipment such as:

- Pulsed magnet power supplies for kickers and septum magnets;
- Pulsed power supplies for RF amplifiers such as klystrons; and
- Mobile phones and Wi-Fi signals (common, and required across much of the facility) whose associated frequencies also represent a source of radiated noise.

It must also be acknowledged that some specialist equipment may not comply with electromagnetic immunity or susceptibility standards. This may be due to the method of operation or the technology readiness level of the device. Detailed investigation of this equipment and the method of operation must be made to ensure this equipment does not have a detrimental impact on other local systems, and may require incorporating specialist noise reduction techniques.

Best practice for these types of facilities is to install two grounding networks—a safety grounding network and reference grounding network—bonded together. Their design and interconnection will depend on the layout of the accelerator and support areas, such as rack rooms and RF equipment.

2.10.4 Cooling System

The cooling system will comprise a primary chilled-water system, secondary de-ionised and general water=cooling circuits, and specific high-stability temperature-control systems for the RF cavities. The proposed use of ground water to provide up to 2 MW net of primary cooling is being considered as part of the overall cooling solution; if feasible, it will increase the capital cost but would significantly reduce operational costs through energy savings.

The cooling infrastructure would comprise bore holes, water chillers, pumps, heat exchangers, pipework, instrumentation, de-ionisation plant and a SCADA system. The system would have sufficient cooling capacity to satisfy the facility water cooling and air conditioning requirements.

The total water cooling load is currently estimated to be ∼2.1 MW, which has been included in the cost model.

2.10.5 Compressed Air

A compressed air supply and distribution system will be required in ITRF. The anticipated parameters are:

- Pressure: 6 bar; and
- Purity: Compliant with ISO 8573-1:2010 (1:2:1) (Food grade, non-direct contact) [81]

2.10.6 Air Conditioning

It is anticipated that a range of air conditioning solutions will be used to match individual room cooling requirements, including DX Comfort cooling systems and high sensible water cooled air handling units for more precision applications. The total air conditioning load is estimated to be ∼0.4 MW.

2.11 List of Highlights since the 6-Month Design Review

- Sustainability contributing to Net Zero by 2040, section 1.1 added.
- Estimate of the ITRF power consumption, document 1272-pa1-pm-est-0001-v2.0-power-consumption-est-2023-09-07.
- Estimate of the Full Infrastructure cost for UKRI IF preliminary activity 2 proposal, document 1272-pa2-pm-fin-0002-v2.0-ITRF-construction-cost-model-2023-09-08.
- Update to the facility schematic, document 1272-pa1-pm-sch-0001-v3.0-ITRF schematic. Figure 10 in this report.
- New draft ITRF vacuum flow diagram, document 1272-pa1-vac-vfd-0001-v0.1
- Mechanical design concept for the laser target chamber for a proton beam tape drive configuration, document 1272-pa1-meng-prs-0009-v1.0-target-chamber-2023-08-22. Update to figure 9 in this report.
- Target chamber vacuum simulations, document 1272-pa1-vac-prs-0001-v1.0-nozzle-gas-trans-prob-2023-08-15
- Mechanical engineering design and Finite Element Analysis of a Fixed Field Accelerator vacuum chamber to inform the combined function magnet gap, document RFS-1055-meng-fea-0001-v2.0-FETS-FFA-Vacuum-Chamber-2023-09-08.
- Update to the Building concept in this report. Figures 1-7 and facility room sized tables 2 and 3.
- Update to the low energy line engineering concept in this report. Figure 8.
- Update to the Vacuum design. Amended section 1.7 in this report.
- Update to the Controls design. Amended section 1.8 in this report.
- Update to the Electrical Engineering design based on the electrical power consumption. Amended section 1.9 in this report.

- Cooling System design concept based on the electrical power consumption added. New section 1.10 in this report.
- Compressed Air and Air Conditioning section 1.11 and 1.12 added to this report.

Table 17: Summary of ITRF Key Events.

Date	Event
13.01.2022	UKRI Ion Therapy Research Facility Webinar Document: UK Ion Therapy Research Facility Webinar - Agenda 130122
26.01.2022	4th ITRF Advisory Committee Meeting
27.04.2022	LhARA Collaboration Meeting
28.04.2022	Future accelerators for biomedical applications Workshop
18.05.2022	5th ITRF Advisory Committee Meeting
13.06.2022	CERN – UKRI STFC Framework Collaboration Agreement KN 5444/ATS signed
20.07.2022	6th ITRF Advisory Committee Meeting
28/9/2022	ITRF IF monitoring Kick Off Meeting
01/10/2022	ITRF Project Start
14/10/2022	LhARA collaboration meeting. Schedule of presentations and agenda at https://indico.stfc.ac.uk/event/628/
19/10/2022	ITRF STFC press release https://www.ukri.org/news/researching-a-new-generation-of-technology-to-treat-cancer/
26/10/2022	LhARA/ITRF international review https://ccap.hep.ph.ic.ac.uk/trac/wiki/Research/DesignStudy/Reviews/AugSep22/Review/29-30Sep22
03/11/2022	7th ITRF Advisory Committee Meeting
07/11/2022	1st ITRF Project Board meeting
29/11/2023	LhARA/ITRF international review Feedback. Document LhARA-Gov-Rev-2022-01 https://ccap.hep.ph.ic.ac.uk/trac/wiki/Research/LhARA/Documentation/TN/Governance Document reviewed: LhARA R&D proposal for the preliminary, pre-construction phases. CCAP-TN-10.
01/12/2022	ITRF JeS grants approved
05/12/2022	Request to UKRI to re-profile finance
14/12/2022	Novel End Station Consultation Meeting https://indico.stfc.ac.uk/event/668/Baselinedocument:LhARA-Gov-PMB-2022-01
18/01/2023	Infrastructure Fund Project Catch-up - Ion Therapy Research Facility
01/02/2023	Ion Therapy Research Facility updated award letter received via J A Clarke by e-mail
08/02/2023	LhARA Collaboration meeting #3 Vinen Room in Physics West, School of Physics and Astronomy, Birmingham, B15 2TT https://indico.stfc.ac.uk/event/685/
12/03/2023	LhARA collaboration response to international review of LhARA, document LhARA-Gov-PMB-2022-02
21/03/2023	ITRF 6 month Design Review https://indico.stfc.ac.uk/event/722/
23/03/2023	2nd ITRF Project Board Meeting
21/04/2023	8th ITRF Advisory Committee meeting
07/05/2023	IPAC 23 conference, Venice. https://www.ipac23.org/
24/05/2023	6 month progress meeting with UKRI Infrastructure Fund Team
01/06/2023	LhARA – ISIS FETS Fixed Field Accelerator common themes meeting
04/06/2023	CRUK–ARR Radiation Research conference 2023, University of Glasgow https://www.cancerresearchuk.org/funding-for-researchers/research-events-and-conferences/cruk-arr-radiation-research-conference-2023
08/06/2023	New trends and initiatives in accelerators for ion therapy of cancer, HITRIplus Seminar, Online. https://indico.cern.ch/event/1282936/
13/06/2023	VS12 Technical Meeting (with IOP) Vacuum in Medical Applications, STFC – DL https://www.vacuum-uk.org/vs12_programme/
19/06/2023	ITRF - LhARA 2nd User Consultation Meeting, University of Birmingham.
22/06/2023	3rd ITRF Project Board.
29/06/2023	Particle Accelerator Beams 2023 conference, University of Strathclyde, Glasgow https://indico.cern.ch/event/1248024/
12/07/2023	IET Medical Accelerators, The Institute of Cancer Research, Royal Marsden, Sutton.
17/07/2023	9th ITRF Advisory Committee meeting.
06/09/2023	4th ITRF Project Board. – propose this meeting is moved to after the 12 month design review
20/09/2023	ITRF 12 month design review, University of Strathclyde, Glasgow https://indico.stfc.ac.uk/event/823/

3 Work Package 3: Conventional technology

The work carried out within ITRF Work Package 3 (WP3) will provide a comparison of conventional technologies with those of the baseline, laser-hybrid, approach adopted by the LhARA collaboration [2]. The scope of WP3 includes the conceptual design of a facility based around a slow-cycling (~ 1 Hz) room-temperature synchrotron, fed from an injector that uses established ion-source technologies and pre-acceleration methods. This design study is intended to enable quantitative comparisons between a conventional accelerator and a facility served by LhARA.

Here, we describe the current status of the WP3 synchrotron design study. In section 3.1 we state the original requirements for the synchrotron design, and review similar designs proposed by the CERN NIMMS study. In section 3.2 we describe the preliminary design of a machine that meets these requirements. Section 3.3 gives an overview of the proposed injector parameters, while section 3.4 outlines the main scheme for beam extraction. Finally, section 3.5 provides estimates for the dose rates delivered to endstations from the synchrotron.

3.1 Synchrotron Requirements

The key requirements for the WP3 synchrotron design were originally defined as follows:

Choice of Ion Species

To maximise the usefulness of the synchrotron, its specifications should be chosen to accommodate the ion species that are most likely to be used for radiotherapy. At present, these are expected to be protons (H^+), helium ($^4He^{2+}$) and carbon ($^{12}C^{6+}$) ions [82].

Machine Parameters

To provide a direct comparison against the baseline LhARA design, the synchrotron should fit within the circumference of the LhARA Fixed-Field Accelerator (FFA) ring (21.86 m) and accommodate beam energies up to its nominal extraction energy. The maximum extraction energy of the LhARA FFA for protons is 127 MeV and for $^{12}C^{6+}$ ions is 33.4 MeV/u [83].

Beam Intensity

Ideally, the synchrotron should support beam intensities that are compatible with the delivery of FLASH dose rates to its endstations. The FLASH regime is generally defined as time-averaged dose rates of $\gtrsim$ 40 Gy/s. For a small synchrotron, this implies that the number of ions extracted per spill should be of order $\sim 10^{10}$.

Choice of Technologies

Consistent with the scope of WP3, the synchrotron design should be based on accessible, conventional technologies. For instance, the synchrotron dipoles should be normal conducting, room-temperature magnets rather than high-field superconducting magnets. The machine specifications should not push the limits of conventional technologies beyond what has routinely been achieved at other accelerator facilities.

3.1.1 Examples

The Next Ion Medical Machine Study (NIMMS) is an umbrella R&D framework established by CERN to consider designs for next-generation radiotherapy machines. The NIMMS collaboration has already proposed several synchrotron designs relevant to this study, including a superconducting carbon ion machine [84], and a room-temperature helium-ion synchrotron [85]. Both designs are intended as the basis for a clinical radiotherapy facility, and therefore accommodate beam energies of several hundred MeV/u and intensities up to 10^{10} ions per cycle.

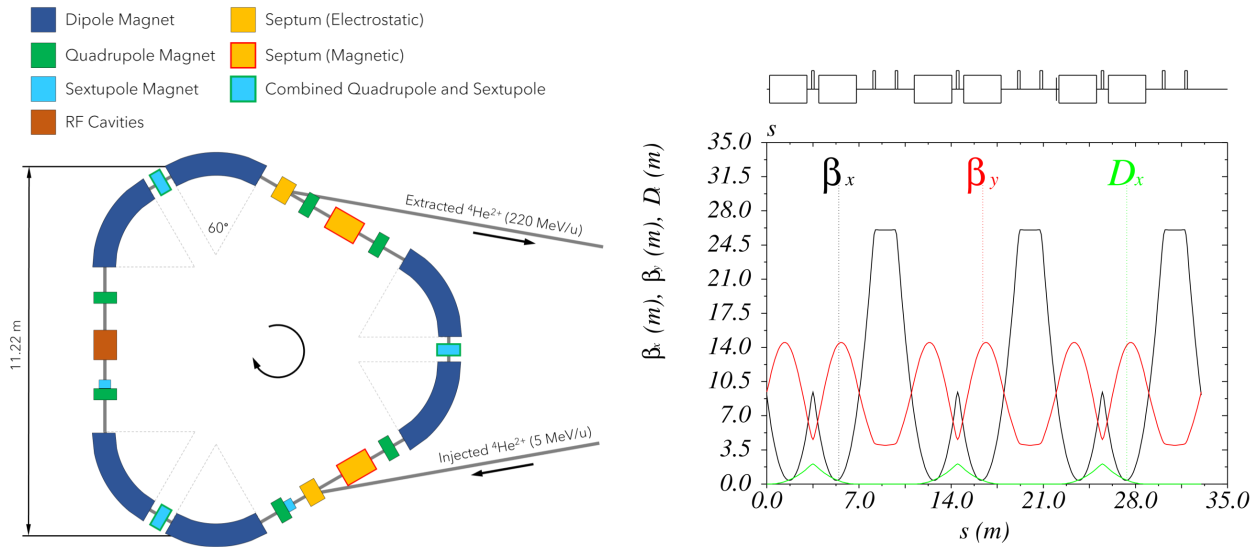

Figure 48: (a) Schematic layout of the NIMMS $^4He^{2+}$ synchrotron, and (b) preliminary optics for the NIMMS synchrotron, calculated in MAD-X. Both figures adapted from Vretenar *et al.* 2023 [85].

The NIMMS helium synchrotron (figure 48(a)) has a circumference of ∼33 m, and is designed to deliver $^4He^{2+}$ ions at energies up to 250 MeV/u. The synchrotron lattice is comprised of three identical achromat cells [86], with each cell containing two 60° sector dipoles. Each dipole has a bending radius of 2.7 m and a maximum field of 1.65 T, with a small defocusing gradient. A strong quadrupole at the centre of each bending section is used to cancel the dispersion in the straight sections, which accommodate the injection, extraction and RF hardware, respectively. These dispersion-cancelling quadrupoles have additional sextupole windings, which are used to control the horizontal chromaticity of the lattice. Figure 48(b) shows the beam optics functions over the full circumference of the NIMMS $^4He^{2+}$ synchrotron.

The NIMMS designs build on CERN's previous experience with small hadron synchrotrons, that includes the ELENA decelerator [87] at the Antiproton Decelerator (AD) facility. ELENA is a small (30.4 m) circumference) synchrotron that decelerates antiprotons ($\bar{p}$) from 5.3 MeV to an extraction energy of only 100 keV. While ELENA operates at far lower beam intensities (typically 10^7 $\bar{p}$ per cycle) and repetition rates (∼0.01 Hz), it employs many of the technologies required by the NIMMS synchrotrons. For example, the ELENA RF system is based on a wideband (0.14 – 2 MHz) cavity loaded with magnetic alloy (MA) cores, allowing operation over a wide range of energies.

3.2 Synchrotron Design

3.2.1 Machine Parameters

The NIMMS $^4He^{2+}$ synchrotron [85] has been used as the basis for the ITRF WP3 synchrotron design, due to its small footprint and large beam intensity. However, the NIMMS helium synchrotron is still significantly larger than the LhARA FFA and must be scaled down by approximately 30% to fit within the same footprint.

The NIMMS design can readily be scaled to match the size and energy range of the LhARA FFA, by simply reducing both the bending radius and maximum field of its dipole magnets. However, much higher beam energies (up to 80 MeV/u for $^{12}C^{6+}$) can be achieved by increasing the circumference of the synchrotron by ∼10% relative to the LhARA FFA. This would yield significant advantages for the facility as a whole—providing greater flexibility in irradiation depth and dose rate at the endstations (see section 3.5)—and has

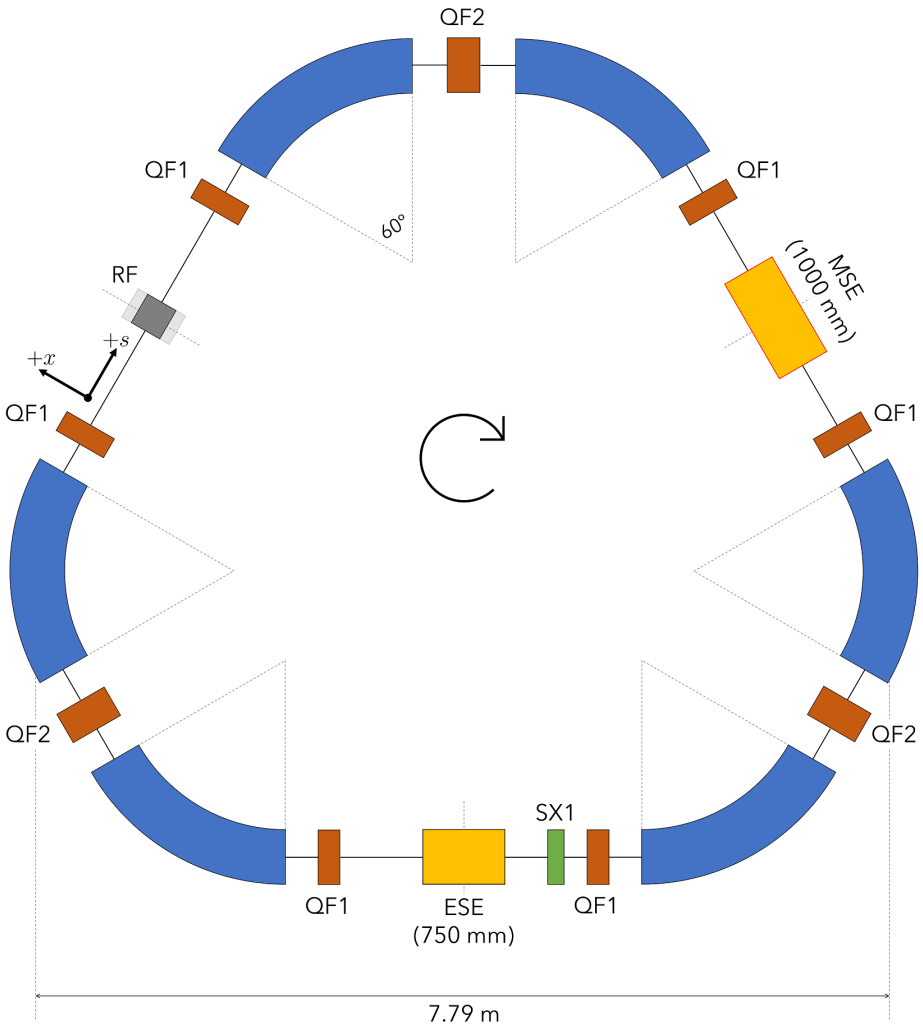

Figure 49: Schematic showing the preliminary layout of the ITRF WP3 synchrotron design, accurate at the time of writing. Elements are approximately to scale.

therefore been chosen here.

Figure 49 shows a schematic layout of the WP3 synchrotron design, which has a circumference of 23.88 m. Table 18 lists the specifications for the six sector dipole magnets. Both the bending radius and maximum field of the dipoles have been reduced relative to the NIMMS design, giving a maximum beam rigidity (at extraction) of 2.70 Tm. This allows the ring to accommodate $^{4}He^{2+}$ and $^{12}C^{6+}$ ions with energies up to 83.5 MeV/u, around 2.5 times higher than the extraction energy of the LhARA FFA. In principle, the dipole magnets can accommodate proton beams with energies up to 300 MeV; however, we anticipate that the maximum H^{+} energy will be limited by the bandwidth of the synchrotron RF system. Assuming an RF bandwidth of 1.0 – 5.5 MHz, the synchrotron may accelerate proton beams to a maximum energy of 105.5 MeV.

3.2.2 Beam Optics

The beam optics functions were primarily calculated using MAD-X [55], accessed via the `cpymad` python library [88]. To enable slow extraction using RF knock-out (RF-KO) or a similar scheme, the synchrotron

Table 18: Specifications for the ITRF synchrotron dipole magnets, and the corresponding maximum beam energies for different ion species.

Parameter		**Value**	
Dipole radius [m]		1.80	
Max. dipole field [T]		1.50	
Max. beam rigidity [T m]		2.70	
Ion species	H^+	$^4He^{2+}$	$^{12}C^{6+}$
Max. beam energy [MeV/u]	105.5	83.5	83.5
Orbital frequency [MHz]	5.50	4.97	4.97

working point must be established close to a third-order betatron resonance. Figure 50 shows the preliminary optics at a working point with $Q_x = 2.66$. Figure 51 shows the location of this working point on a tune diagram, with resonances plotted up to fourth order.

By adjusting the strengths of the QF1 quadrupoles (see lattice layout shown in figure 49) the ring can also be operated at a working point with $Q_x = 2.33$. However, this working point cannot be used in practice, as it provides insufficient phase advance between the electrostatic and magnetic extraction septa (see section 3.4). Table 19 summarises the beam optics for our chosen working point with $Q_x = 2.66$.

3.3 Injector

3.3.1 Key Parameters

As proposed in both NIMMS designs, we expect that the synchrotron will be filled from a conventional injector that resembles CERN's Linac 4. Several ion sources can be connected to the injector via a magnetic switchyard, allowing a range of ion species to be used interchangeably.

In the NIMMS injector [85], ions are accelerated to a nominal injection energy of 5 MeV/u using a 352 MHz Radio-Frequency Quadrupole (RFQ) followed by a single (Linac-4-like) Drift Tube Linac (DTL) tank. The injection energy of 5 MeV/u was chosen primarily based on the efficiency of typical stripping foils, such as those used to produce $^{12}C^{6+}$ ions from $^{12}C^{4+}$. To mitigate space charge effects, protons are injected at 10 MeV using a second DTL tank, which can be turned off entirely when working with ions.

For the purposes of this design study, we assume a set of injector parameters based on those of the proposed SEEIST facility [89]. Table 20 lists the expected beam current for protons, $^4He^{2+}$ and $^{12}C^{6+}$ ions at injection. Commercial Electron Cyclotron Resonance (ECR) ion sources such as the Pantechnik *Supernanogan* source [90, 91] can provide up to 2 mA of H^+ current.

3.3.2 Multi-Turn Injection

In order to accumulate sufficient ions for FLASH extraction during each synchrotron cycle, we expect to load beam using multi-turn (MT) injection. In this scheme, ions are typically injected over 15 – 20 successive turns. Assuming that the injector emittance is much smaller than the synchrotron acceptance, the phase space of the circulating beam is gradually filled with charge, as illustrated in figure 52. The charge distribution is then smoothed out due to phase space filamentation over subsequent turns.

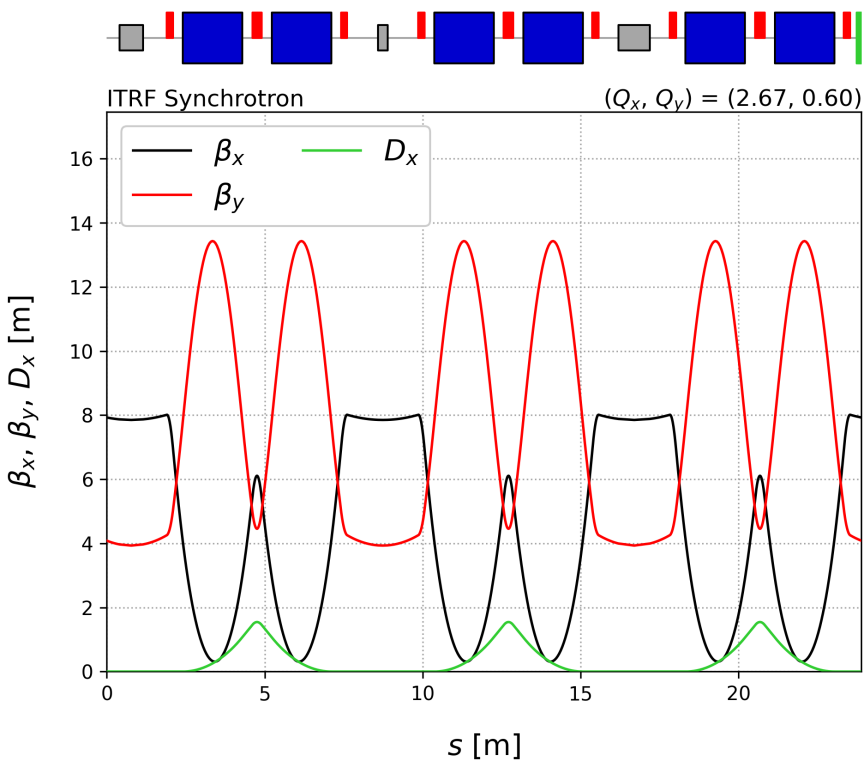

Figure 50: MAD-X calculation showing the preliminary synchrotron optics, with the machine tuned to a working point close to the third-order resonance $Q_x = 2.66$.

Table 19: Summary of beam optics parameters for the synchrotron working point with $Q_x = 2.66$, as shown in figure 50.

Parameter	**Value**
Focusing Strengths	
QF1 Quadrupoles [m^{-2}]	+3.76
QF2 Quadrupoles [m^{-2}]	+5.35
Sector Dipoles [m^{-2}]	-0.57
Optics functions	
Max. β_x [m]	8.01
Max. β_y [m]	13.4
Max. D_x [m]	1.55
Working Point	
Tune Q_x, Q_y	2.66, 0.60
Natural Chromaticity Q'_x, Q'_y	-3.82, -3.62

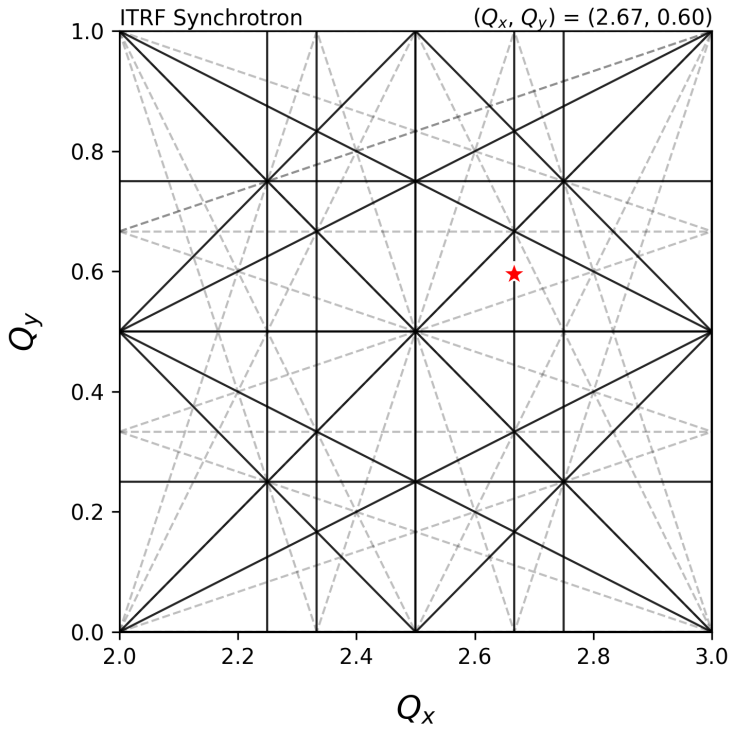

Figure 51: Tune diagram showing the location of the proposed working point $(Q_x,\, Q_y) = (2.66,\, 0.60)$ relative to resonances up to fourth order. The working point is indicated with a red star. Skew resonances are shown as dashed lines.

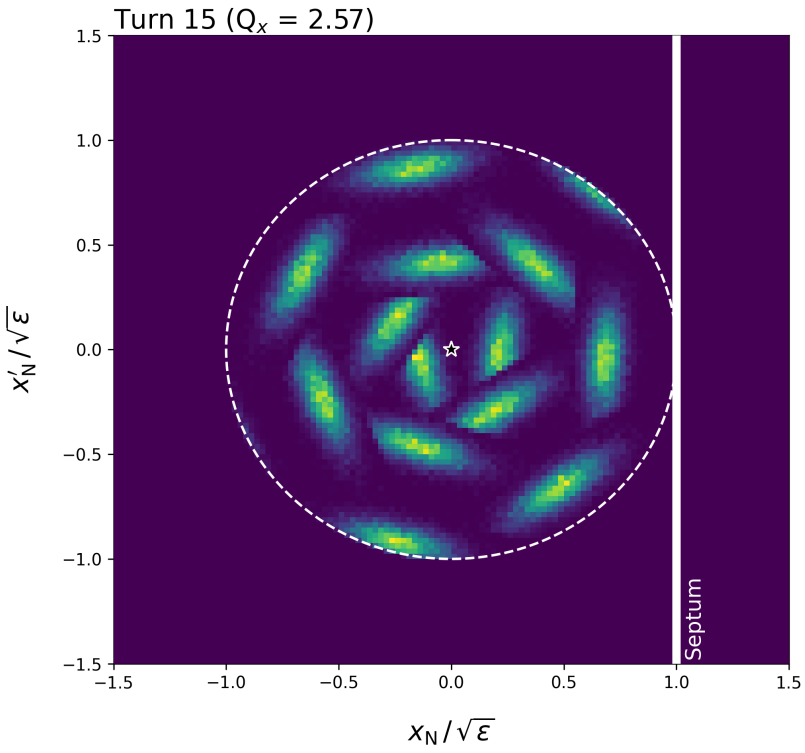

Figure 52: The distribution of charge density in normalised transverse phase space after MT injection. The distribution was calculated using a toy model, assuming a synchrotron tune of $Q_x = 2.27$ and MT injection over 15 turns. The synchrotron acceptance is shown as a dashed white line, and the septum location is indicated as a solid white line.

Table 20: Injector parameters and corresponding stored intensities for different ion species. Injector parameters are based on those of the proposed SEEIST facility [89].

Parameter	**Values**		
	H^+	$^4He^{2+}$	$^{12}C^{6+}$
Linac Current [mA]	2.0	1.0	0.2
Injection Energy [MeV/u]	10.0	5.0	5.0
Orbital Period [MHz]	1.82	1.29	1.29
MT Injection Efficiency [%]		60%	
Ions After 15 Turns [10^{10}]	6.19	2.18	0.15
Space Charge Tune Shifts			
ΔQ_x	-0.12	-0.01	< 0.01
ΔQ_y	-0.13	-0.02	< 0.01

We estimate the stored intensity for each ion species using the parameters in table 20, assuming MT injection over 15 turns with an efficiency of 60% [92]. The maximum number of circulating ions for both H^+ and $^4He^{2+}$ that is predicted to be possible is greater than 10^{10}. Only $\sim 10^9$ $^{12}C^{6+}$ions can be accelerated per synchrotron cycle, limited by the lower beam current generated by the carbon ion source.

The tune shift due to the transverse defocusing effect of space charge is largest at injection. In general, a space charge tune shift $|\Delta Q| \leq 0.25$ is considered to be acceptable; larger tune shifts may require a resonance compensation scheme. For each ion species, we estimate the space charge tune shift in the horizontal plane as

$$\Delta Q_x = -\frac{Z^2 r_p N_0}{2\pi A \beta^2 \gamma^3 \epsilon_x} \left\langle \frac{2}{1+\sqrt{\epsilon_y \beta_y / \epsilon_x \beta_x}} \right\rangle , \tag{3}$$

where N_0 is the number of circulating ions, r_p is the classical proton radius, ϵ_x is the geometric emittance in the horizontal plane, and A and Z are, respectively, the atomic mass and charge state of the ion. The relativistic β and γ functions and optical beta functions $\beta_{x,y}$ are defined as usual. A similar expression can be obtained for the tune shift in the vertical plane.

As shown in table 20, the space charge tune shift is within an acceptable bound for each ion species. The number of ions per spill is therefore limited by the injector parameters rather than by space charge considerations, in contrast to the NIMMS designs on which the present lattice is based.

3.4 Beam Extraction

3.4.1 Extraction Scheme

We expect to use RF knock-out (RF-KO) for slow resonant beam extraction, consistent with the original NIMMS $^4He^{2+}$ synchrotron design. In this scheme, the horizontal tune of the synchrotron is set to a third order resonance (such as $Q_x = 2.66$, as shown in figure 50), which is excited using one or more resonant sextupole magnets.

Close to a third-order resonance, the ion trajectories in normalised phase space are defined by the Kobayashi Hamiltonian [93]:

$$H = 3\pi\,\delta Q \left(x_N^2 + x'^2_N\right) + \frac{S}{4}\left(3\,x_N\,x'^2_N - x_N^3\right) ; \tag{4}$$

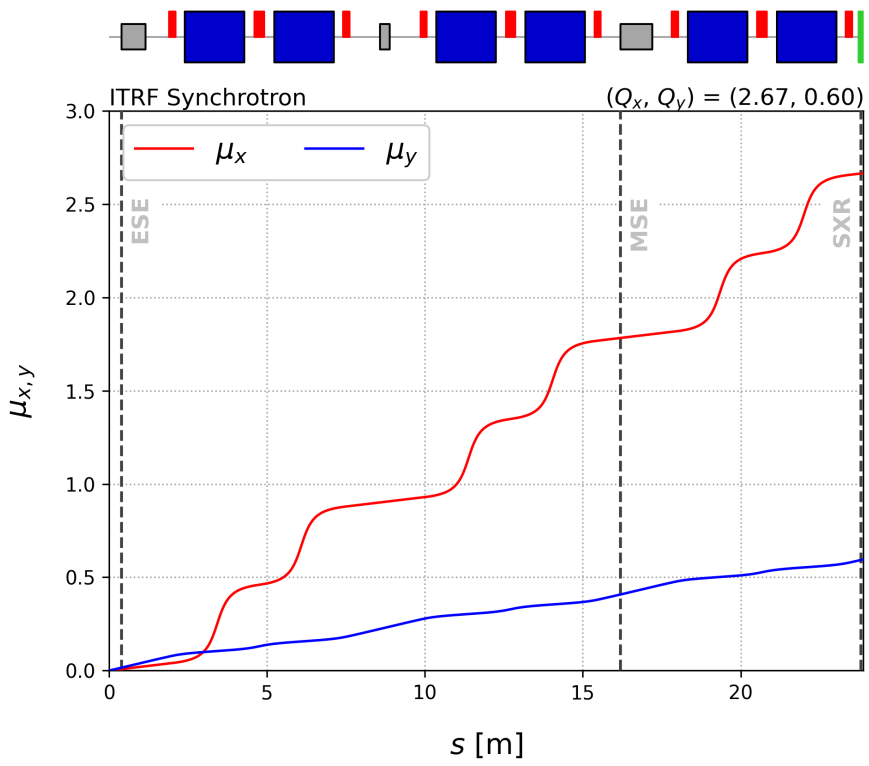

Figure 53: Horizontal and vertical phase advance (shown in Q units) as a function of longitudinal distance around the synchrotron ring. The locations of the electrostatic (ESE) and magnetic (MSE) extraction septa and resonant sextupole (SXR) are indicated as dashed vertical lines.

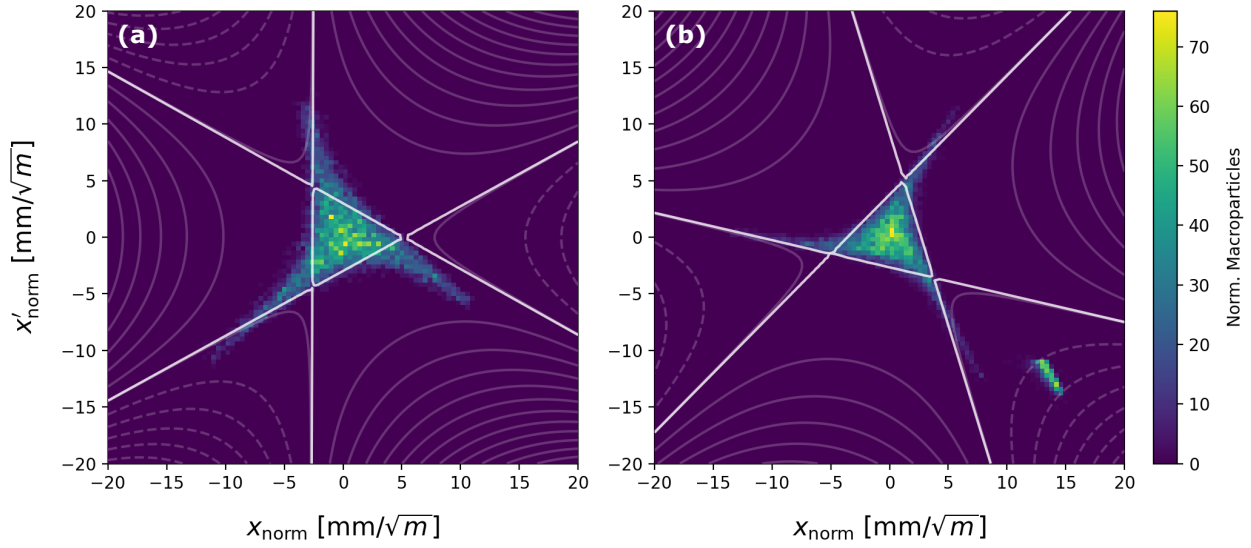

Figure 54: MAD-X particle tracking simulation showing the (normalised) horizontal phase space of a proton beam during resonant extraction. The phase space is shown (a) immediately after the resonant sextupole and (b) at the magnetic extraction septum (MSE). The smooth lines show the contours of equation refeq:kobayashi-hamiltonian. Panel (a) shows only the circulating beam, while (b) also shows ions that have been extracted from the main distribution.

where $\delta Q = (Q_{\mathrm{ion}} - Q_{\mathrm{res}})$ is the tune distance of the ion from the nearest third-order resonance, and x_N and ${x'}_N$ are the standard particle coordinates in normalised phase space. The parameter S represents the effect of the resonant sextupole, with

$$S = \frac{1}{2}\beta_x^{3/2}\, l_S\, k_2\,, \tag{5}$$

where l_S and k_2 are respectively the effective length and normalised strength of the resonant sextupole; β_x is the horizontal beta function at the location of that sextupole.

Close to a third-order resonance, the second term of equation 4 will distort the phase space trajectories of ions into triangular shapes (see figure 54). Ions within a central region of phase space (the 'stable triangle') will follow closed trajectories and remain stable over many turns. However, ions outside of this region are unstable, and will eventually follow the separatrices of the Hamiltonian to large amplitudes.

In the RF-KO extraction scheme, a pair of electrostatic plates are used to kick the beam at frequencies close to the betatron tune [94, 95]. These transverse kicks gradually drive ions out of the stable region of phase space, allowing them to be extracted at the Electrostatic Extraction Septum (labelled ESE in figure 50). Ions that exceed the aperture of the ESE are imparted with a horizontal kick that causes their orbit to deviate from the circulating beam. These ions arrive at the magnetic extraction septum (labelled MSE in figure 49) with a large transverse offset from the main beam, allowing them to be safely extracted from the synchrotron with minimal losses.

3.4.2 Particle Tracking Simulations

Figure 53 shows the horizontal and vertical phase advance as a function of distance around the synchrotron ring. To maximise the separation between the extracted ions and circulating beam at the magnetic septum, it

must be placed at a phase advance of either $90°$ or $270°$ from the ESE. As shown in figure 53, the phase advance between septa is approximately $280°$ in the proposed synchrotron design.

Particle tracking simulations using MAD-X [55] were used to verify that the proposed synchrotron lattice is compatible with slow resonant extraction. In these simulations, a resonant sextupole (labelled SXR in figures 49 and 53) was used to excite the third-order resonance at $Q_x = 2.660$. An ion distribution (typically comprising 10^4 macroparticles) was then tracked around the synchrotron for several hundred turns. If the initial emittance of the simulated beam is chosen to be larger than the stable region of phase space, some ions are initialised on unstable trajectories and quickly exceed the aperture of the electrostatic septum. Figure 54(a) shows the phase space of a simulated 100 MeV H^+ beam during resonant extraction.

We assume an electrostatic septum with an aperture of 25 mm and a deflection angle of 2.5 μrad, similar to the septum currently used in the operation CNAO carbon-ion therapy synchrotron. Ions that exceed the septum aperture are considered to be extracted, and are removed from the simulation and their coordinates recorded. These 'extracted' ions were then tracked around one full turn of the synchrotron to find their coordinates at the magnetic septum. Figure 54(b) shows the phase space distribution of extracted ions at the MSE. For comparison, the remaining part of the circulating beam is also shown; clearly, the extracted ions have a large transverse separation from the main beam.

The above simulations do not yet include time-dependent elements, such as the kicker used to drive ions out of the stable region of phase space during extraction. Consequently, our simulations are not yet a full dynamic representation of RF-KO extraction and cannot address the question of how quickly (or slowly) ions are extracted during a typical spill. However, extensive simulations have been carried out for the NIMMS and PIMMS therapy synchrotrons (the latter including those at CNAO and MedAustron) [94, 95]. Previous work has shown that RF-KO schemes can be used to produce a uniform spill over a timescale of 0.1 – 1.0 s.

For the ITRF synchrotron, an extraction timescale of 100 ms corresponds to around 550,000 turns for a proton beam, and 497,000 turns for either $^4He^{2+}$ or $^{12}C^{6+}$. Beam extraction on timescales below 100 ms may be possible, but has not been explored yet due to the challenging dosimetry requirements in this regime.

3.5 Extracted Dose Rates

3.5.1 Penetration Depth

Here, we estimate the range of each ion species (H^+, $^4He^{2+}$ and $^{12}C^{6+}$) at the extraction energies listed in table 22. Throughout this section, we use the ordinary convention of calculating ion ranges and dose rate assuming the irradiated volume is composed of water.

The range of an ion beam R_{water} can be estimated using the Bethe-Bloch equation, which describes the mean rate of energy loss for a relativistic ion passing through matter. The equation can be written as [96]

$$-\left\langle \frac{dE}{dx} \right\rangle = kz^2 \frac{Z}{A} \frac{1}{\beta^2} \left[\frac{1}{2} \ln \frac{2m_e c^2 \beta^2 \gamma^2 T_{\text{max}}}{I^2} - \beta^2 - \frac{\delta(\beta\gamma)}{2} \right], \tag{6}$$

where Z and A are the atomic number and atomic mass of the absorber, z is the charge of the incident particle, and $I \simeq 11.5Z$ eV is the mean ionisation potential. $T_{max} = 2m_e c^2 \beta^2 \gamma^2 / [1 + 2\gamma m_e / M + (m_e/M)^2]$ is the maximum kinetic energy that can be imparted to an electron in a single collision, $k = 4\pi N_A r_e^2 m_e c^2$, and β and γ are the conventional relativistic factors. $\delta(\beta\gamma)$ is a density correction term. We note that the PDG formula overestimates the experimentally achieved range by a few percent [97], but is good enough for the approximate estimates here.

In order to use the Bethe-Bloch equation to estimate the range of an ion beam, equation 6 must be integrated over the path of an ion until it loses most of its initial kinetic energy. A more straightforward estimate can be

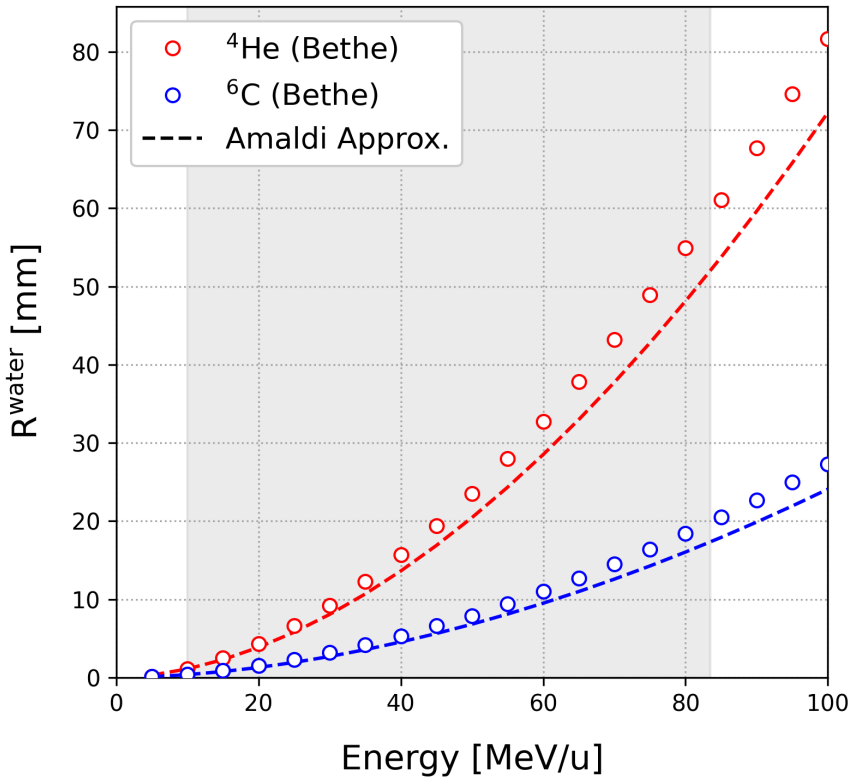

Figure 55: Penetration depth of $^4He^{2+}$ and $^{12}C^{6+}$ ions in water, as a function of initial beam energy. Penetration depths calculated were calculated analytically using the Bethe-Bloch equation and the Amaldi approximation. The shaded region indicates the energy range of the proposed synchrotron design.

obtained using the Amaldi approximation [98]:

$$R_{\text{water}} \simeq 425\,\text{cm}\,\frac{A}{Z^2}\left(\frac{E_k}{m_p c^2}\right)^{1.82}\;; \tag{7}$$

where E_k is the total initial kinetic energy of the ion; this approximation is a refinement of the Bragg-Kleeman relationship [99].

Figure 55 shows the ranges of $^4He^{2+}$ and $^{12}C^{6+}$ ions with initial energies up to 100 MeV/u. As noted earlier, the extraction energy of the proposed synchrotron has been defined so that carbon ions will penetrate up to 20 mm in water. This provides increased flexibility in user experiments, and may enable *in vivo* experiments with small animal models.

3.5.2 Dose Calculation for Protons

The achievable dose rates from any accelerator source depend not only upon the accelerator source parameters—notably ions per spill, source repetition rate (the latter being here the synchrotron cycling rate), and extracted particle energy—but also upon the field size and depth into which the ions are delivered. To illustrate the likely dose rates that may be obtained, we consider two indicative situations:

(a) Target volume with a 3×3 cm field size, extending from a depth of 0 – 1 cm to enclose a 9 cm^3 volume; and

(b) Target volume with a 1×1 cm field size, extending from a depth of 0 – 1 cm to enclose a 1 cm^3 volume.

For simplicity (since we are in essence concerned with orders of magnitude), we follow the method outlined in Owen *et al.* 2014 [100]. The basis of this method is to note that total deposited energy determined by the number of ions in a spill and by the kinetic energy of each ion. We assume that dose is uniformly deposited over the volume by using a spread-out Bragg peak (SOBP) approach; the extraction energy is therefore adjusted for each depth layer to position a Bragg peak at that depth. There will be some additional dose deposited outside the target volume due to lateral scattering (multiple Couloumb scattering), but given the low ion energies this is a small proportion of the overall energy carried by the incident ions.

For protons incident upon either target volume, a 1 cm depth requires 33.7 MeV protons, as estimated using the Amaldi approximation (equation 7). The required energy to place a Bragg peak mid-way through the depth range (at 0.5 cm) is around 23 MeV, so we use that as an estimate of the average energy deposited by a proton within the target volume; 23 MeV is 3.7 pJ per proton. With an estimated 5×10^{10} protons/spill, this is 0.184 J deposited per spill. In a 9 cm^3 volume this corresponds to 20.5 Gy dose per spill; if complete beam extraction can be achieved in 100 ms this would be a dose of 205 Gy/s for 100 ms, and a time-averaged dose rate of 20.5 Gy/s over multiple extraction spills at 1 Hz synchrotron cycling rate.

A similar estimate can be made for the smaller target volume (b). The same 0.184 J deposited energy within the smaller volume gives nine times the dose, around 184 Gy per spill. A 100 ms extraction duration would therefore achieve a dose rate of 184 Gy/s, and a time-averaged dose rate of 184 Gy/s over multiple spills.

3.5.3 Dose Estimates for Ions

We can make similar estimates of achievable dose rates for heavier ions; here we consider $^4He^{2+}$ and $^{12}C^{6+}$ incident upon the same water volumes. Helium ions of 21.8 MeV/u kinetic energy have a Bragg peak half-way through the two volumes (0.5 cm), and 31.8 MeV/u is needed to reach the furthest (1 cm) depth. Using the same method as for protons but accounting for the lower number of extracted ions, the dose per spill is somewhat greater than it is for protons (see table 21). Carbon ion dose rates can be calculated the same way; despite the far lower number of ions per spill, the much larger kinetic energy carried by each carbon ion means that the dose rate is comparable to that of protons.

Table 21: Estimated extracted dose rates for two indicative volumes (a) and (b) as described in the main text, assuming a synchrotron cycling rate of 1 Hz and a spill duration of 100 ms.

	Ion Species		
	H^+	$^4He^{2+}$	$^{12}C^{6+}$
Extraction Energy [MeV/u]	105.5	83.5	83.5
Extracted Ions [10^{10}]	5.00	2.00	0.15
Median Ion Energy [MeV/u] (0.5 cm)	23.1	23.1	42.2
Max Ion Energy [MeV/u] (1 cm)	33.7	33.7	61.7
Target volume (a)			
Dose Per Spill [Gy/spill]	20.5	32.8	13.5
Dose Rate During 100 ms Spill [Gy/s]	205	328	135
Average Dose Rate (1 Hz Cycling) [Gy/s]	20.5	32.8	13.5
Target volume (b)			
Dose Per Spill [Gy/spill]	184	295	121
Dose Rate During 100 ms Spill [Gy/s]	1840	2950	1210
Average Dose Rate (1 Hz Cycling) [Gy/s]	184	295	121

3.6 Accelerator Magnet Parameters

The preliminary specifications for the main synchrotron magnet types are presented in this section. Tables 22, 23 and 24 list the specifications for the dipole, quadrupole and sextupole magnets, respectively.

3.7 Conclusions

A preliminary design for a slow-cycling (1 Hz) radiobiology synchrotron has been established as part of ITRF WP3. The synchrotron and its injector have been adapted from designs proposed by the CERN NIMMS project, using established technologies for both the ion sources and accelerator. The synchrotron parameters have been chosen to provide a direct comparison against the LhARA FFA post-acceleration stage, with a similar circumference and slightly higher beam energy at extraction. Based on typical injector parameters, we have shown that beam intensities of order 10^{10} ions per spill are possible, and also estimated the corresponding dose rates delivered to the endstations. A scheme for slow beam extraction using the RF knockout technique has been outlined, and explored using particle tracking simulations. In future, we expect to build upon these simulations to explore the accessible range of timescales for beam extraction from the synchrotron.

Table 22: Preliminary parameters for the synchrotron dipole magnets (SB1 in figure 49. Estimates for the magnet electrical properties and power consumption are based on existing magnet designs and simple scaling arguments.

Parameter	**Value**
Bend Angle [deg]	60
Bend Radius [m]	1.8
Magnetic Length [m]	1.885
Magnetic Field	
Min. Dipole Field [T]	0.25
Max. Dipole Field [T]	1.50
Quadrupole Coeffient k_1 [m^{-2}]	-0.57
Max. Quadrupole Gradient [T/m]	-1.53
Physical Aperture	
Horizontal [mm]	70
Vertical [mm]	35
Power Requirements	
Windings Resistance [mΩ]	570
Max. Current [A]	240
Max. Voltage [V]	135
Dissipated Power [kW]	32.5

Table 23: Preliminary parameters for the synchrotron quadrupole magnets (QF1 and QF2 in figure 49). Estimates for the magnet electrical properties and power consumption are based on existing magnet designs and simple scaling arguments.

Parameter	**Value**	
	QF1	**QF2**
Magnetic Length [m]	200.0	300.0
Physical Aperture [mm]	∅80.0	∅80.0
Magnetic Field		
Quadrupole Coeffient k_1 [m^{-2}]	+3.75	+5.35
Max. Quadrupole Gradient [T/m]	+10.1	+14.4
Sextupole Coeffient k_2 [m^{-3}]	-	+5.68
Max. Sextupole Gradient [T/m^2]	-	+15.35
Power Requirements		
Windings Resistance [mΩ]	225	335
Max. Current [A]	103	137
Max. Voltage [V]	11.8	25.2
Dissipated Power [kW]	1.20	3.70

Table 24: Preliminary parameters for the synchrotron resonant sextupole magnet (SXR figure 49). Estimates for the magnet electrical properties and power consumption are based on existing magnet designs and simple scaling arguments.

Parameter	**Value**
Magnetic Length [m]	150.0
Physical Aperture [mm]	∅80.0
Magnetic Field	
Sextupole Coeffient k_2 [m^{-3}]	20.0
Max. Sextupole Gradient [T/m^2]	54.00
Power Requirements	
Windings Resistance [mΩ]	
Max. Current [A]	
Max. Voltage [V]	
Dissipated Power [kW]	

References

[1] "ITRF Organisational Breakdown Structure," 1272-pa1-pm-pmp-0002-v2.2-organisational-breakdown-structure.

[2] G. Aymar, T. Becker, *et al.*, "LhARA: The Laser-hybrid Accelerator for Radiobiological Applications," *Frontiers in Physics* **8** (2020) . https://www.frontiersin.org/articles/10.3389/fphy.2020.567738.

[3] The LhARA consortium, "The Laser-hybrid Accelerator for Radiobiological Applications," Tech. Rep. CCAP-TN-01, The Centre for the Clinical Application of Particles, Imperial College London, 2020. https://ccap.hep.ph.ic.ac.uk/trac/raw-attachment/wiki/Communication/Notes/CCAP-TN-01.pdf.

[4] The LhARA collaboration, "The Laser-hybrid Accelerator for Radiobiological Applications: R&D proposal for the preliminary, pre-construction phases," Tech. Rep. CCAP-TN-10, The Centre for the Clinical Application of Particles, Imperial College London, 2022. https://ccap.hep.ph.ic.ac.uk/trac/raw-attachment/wiki/Communication/Notes/CCAP-TN-10.pdf.

[5] "ITRF Document Naming Convention," 1272-pa1-pm-rpt-0002-v1.0-ITRF-document-naming Ion Therapy Research Facility - rpt - Reports - All Documents (sharepoint.com).

[6] "ITRF SharePoint site," https://stfc365.sharepoint.com/sites/ITRF.

[7] "LhARA; the Laser-hybrid Accelerator for Radiobiological Applications," https://ccap.hep.ph.ic.ac.uk/trac/wiki/Research/LhARA. (Accessed 31-03-2023).

[8] "ITRF project roles and responsibility, 1272-pa1-pm-pmp-0004-v3.0-roles-governance," https://stfc365.sharepoint.com/sites/ITRF/ Ion Therapy Research Facility - pmp - Project Management Plan - All Documents (sharepoint.com).

[9] "ISO9001 Quality Management ," https://www.iso.org/iso-9001-quality-management.html.

[10] "BSI ISO 9001 Certification," https://www.bsigroup.com/en-GB/iso-9001-quality-management/Certification-for-ISO-9001/.

[11] "Business Case, 1272-pa1-pm-rpt-0003-v0.6-business-case," https://stfc365.sharepoint.com/sites/ITRF/" Ion Therapy Research Facility - rpt - Reports - All Documents (sharepoint.com).

[12] "Project Management Plan, 1272-pa1-pm-pmp-0001-v13.0-ITRF-2023-09-28," https://stfc365.sharepoint.com/sites/ITRF/ Ion Therapy Research Facility - pmp - Project Management Plan - All Documents (sharepoint.com).

[13] A. Lühr, C. von Neubeck, *et al.*, ""Radiobiology of Proton Therapy": Results of an international expert workshop," *Radiother Oncol* **128** no. 1, (June, 2018) 56–67.

[14] T.-S. Dascalu, *Study of non-neutral electron plasma lenses for focusing laser-driven ion beams*. PhD thesis, Imperial College London, May, 2023. Available at https://ccap.hep.ph.ic.ac.uk/trac/attachment/wiki/Communication/Theses/2023/2023-05-DASCALU_TS.pdf.

[15] J. Bin, K. Allinger, *et al.*, "A laser-driven nanosecond proton source for radiobiological studies," *Applied Physics Letters* **101** no. 24, (12, 2012) 243701, https://pubs.aip.org/aip/apl/article-pdf/doi/10.1063/1.4769372/13567881/243701 https://doi.org/10.1063/1.4769372.

[16] The LhARA collaboration, "Baseline for the LhARA design update," Tech. Rep. CCAP-TN-11, The Centre for the Clinical Application of Particles, Imperial College London, 2022. https://ccap.hep.ph.ic.ac.uk/trac/raw-attachment/wiki/Communication/Notes/CCAP-TN-11-LhARA-Design-Baseline.pdf.

[17] "Design of a superconducting solenoid suitable to work with a laser particle source," https://cds.cern.ch/record/2781684.

[18] **LhARA** Collaboration, "LhARA Project Management Board pages," https://ccap.hep.ph.ic.ac.uk/trac/wiki/Research/LhARA/Governance/ProjectManagementBoard, 2023. Accessed: 2023-03-21.

[19] **LhARA** Collaboration, "Laser-driven proton and ion source," https://ccap.hep.ph.ic.ac.uk/trac/wiki/Research/LhARA/LaserDrivenSource, 2023. Accessed: 2023-03-21.

[20] **LhARA** Collaboration, "Gabor Lens," https://ccap.hep.ph.ic.ac.uk/trac/wiki/Research/LhARA/GaborLens, 2023. Accessed: 2023-03-21.

[21] **LhARA** Collaboration, "Ionacoustic dose mapping," https://ccap.hep.ph.ic.ac.uk/trac/wiki/Research/LhARA/IonAcoustic, 2023. Accessed: 2023-03-21.

[22] **LhARA** Collaboration, "End station R&D and vertical beam line development," https://ccap.hep.ph.ic.ac.uk/trac/wiki/Research/LhARA/EndStation, 2023. Accessed: 2023-03-21.

[23] **LhARA** Collaboration, "Accelerator design and facility integration," https://ccap.hep.ph.ic.ac.uk/trac/wiki/Research/LhARA/DesignAndIntegration, 2023. Accessed: 2023-03-21.

[24] **LhARA** Collaboration, "LhARA Executive Board," https://ccap.hep.ph.ic.ac.uk/trac/wiki/Research/LhARA/Governance/ExecutiveBoard, 2023. Accessed: 2023-03-21.

[25] **LhARA** Collaboration, "NOVEL END-STATION DEVELOPMENT: CONSULTATION 1," https://indico.stfc.ac.uk/event/668/, 2022. Accessed: 2023-09-30.

[26] **LhARA** Collaboration, "NOVEL END-STATION DEVELOPMENT: CONSULTATION 2," https://indico.stfc.ac.uk/event/780/, 2023. Accessed: 2023-09-30.

[27] **LhARA** Collaboration, "LhARA Collaboration Meeting," https://indico.stfc.ac.uk/event/685/, 2023. Accessed: 2023-03-21.

[28] B. Fryxell, K. Olson, and P. Ricker, "FLASH: AN ADAPTIVE MESH HYDRODYNAMICS CODE FOR MODELING ASTROPHYSICAL THERMONUCLEAR FLASHES," *The Astrophysical Journal Supplement Series* **131** (2000) 273–334. http://iopscience.iop.org/0067-0049/131/1/273.

[29] D. A. Mariscal, B. Z. Djordjević, *et al.*, "A flexible proton beam imaging energy spectrometer (PROBIES) for high repetition rate or single-shot high energy density (HED) experiments (invited)," *Review of Scientific Instruments* **94** no. 2, (2023) 023507, https://doi.org/10.1063/5.0101845. https://doi.org/10.1063/5.0101845.

[30] "ITRF 6-Month Report," 1272-pa1-pm-rpt-0005-v1.0-six-month-design-review-report.

[31] J. Hills, Private Communication, 2023.

[32] N. Xu, M. J. Streeter, *et al.*, "Versatile tape-drive target for high-repetition-rate laser-driven proton acceleration," *High Power Laser Science and Engineering* **11** (2023) e23.

[33] "WarpX," https://github.com/ECP-WarpX/WarpX.

[34] J.-L. Vay, A. Almgren, *et al.*, "Warp-X: A new exascale computing platform for beam–plasma simulations," *Nuclear Instruments and Methods in Physics Research Section A: Accelerators, Spectrometers, Detectors and Associated Equipment* **909** (2018) 476–479. https://www.sciencedirect.com/science/article/pii/S0168900218300524. 3rd European Advanced Accelerator Concepts workshop (EAAC2017).

[35] "VSim (Tech-X)," https://txcorp.com/vsim/.

[36] The LhARA collaboration, "The Laser-hybrid Accelerator for Radiobiological Applications: Scope of work to be carried out under the ITRF Preliminary Activity," Tech. Rep. CCAP-TN-10 Annex, The Centre for the Clinical Application of Particles, Imperial College London, 2022. https://ccap.hep.ph.ic.ac.uk/trac/raw-attachment/wiki/Communication/Notes/CCAP-TN-10-LhARA-ITRF-proposal-annex.pdf.

[37] W. Zhang, I. Oraiqat, *et al.*, "Real-time, volumetric imaging of radiation dose delivery deep into the liver during cancer treatment," *Nature Biotechnology* **41** no. 8, (Aug, 2023) 1160–1167. https://doi.org/10.1038/s41587-022-01593-8.

[38] T. Bortfeld, "An analytical approximation of the Bragg curve for therapeutic proton beams," *Medical Physics* **24** no. 12, (1997) 2024–2033, https://aapm.onlinelibrary.wiley.com/doi/pdf/10.1118/1.598116. https://aapm.onlinelibrary.wiley.com/doi/abs/10.1118/1.598116.

[39] "NOVEL END-STATION DEVELOPMENT: CONSULTATION 1," https://indico.stfc.ac.uk/event/668/.

[40] "LhARA second peer-group consultation," https://indico.stfc.ac.uk/event/780/.

[41] S. Ghithan, G. Roy, and S. Schuh, *Feasibility Study for BioLEIR*. CERN Yellow Reports: Monographs. CERN, Geneva, 2017. https://cds.cern.ch/record/2260516. 183 pages.

[42] ""LhARA Consultation User Survery"," https://forms.office.com/e/uszHSkq5Xe.

[43] "Quasar Group," https://www.liverpool.ac.uk/quasar/.

[44] A. Salehilashkajani, H. D. Zhang, *et al.*, "A gas curtain beam profile monitor using beam induced fluorescence for high intensity charged particle beams," *Applied Physics Letters* **120** no. 17, (04, 2022) 174101, https://pubs.aip.org/aip/apl/article-pdf/doi/10.1063/5.0085491/16480328/174101 https://doi.org/10.1063/5.0085491.

[45] J. Wolfenden, N. Kumar, A. Salehilashkajani, C. Welsch, and H. Zhang, "Gas Jet In-Vivo Dosimetry for Particle Beam Therapy," in *Proc. IPAC'21*, no. 12 in International Particle Accelerator Conference, pp. 4548–4551. JACoW Publishing, Geneva, Switzerland, 08, 2021. https://jacow.org/ipac2021/papers/frxc05.pdf. https://doi.org/10.18429/JACoW-IPAC2021-FRXC05.

[46] A. Lourenco *et al.*, "Absolute dosimetry for FLASH proton pencil beam scanning radiotherapy," *Scientific Reports* **13** no. 2054, (04, 2023) 1–11, https://www.nature.com/articles/s41598-023-28192-0. https://doi.org/10.1038/s41598-023-28192-0.

[47] J. Bourhis *et al.*, "Treatment of a first patient with FLASH-radiotherapy," *Radiotherapy and Oncology* **139** (10, 2019) 18. https://doi.org/10.1016/j.radonc.2019.06.019.

[48] J. Perl *et al.*, "TOPAS: An innovative proton Monte Carlo platform for researchand clinical applications," *Med. Phys.* **39** (11, 2012) 6818, https://aapm.onlinelibrary.wiley.com/doi/10.1118/1.4758060. https://doi.org/10.1118/1.4758060.

[49] T. Bohlen *et al.*, "The FLUKA Code: Developments and Challenges for High Energy and Medical Applications," *Nuclear Data Sheets* **120** (06, 2014) 211, https://www.sciencedirect.com/science/article/abs/pii/S0090375214005018. https://doi.org/10.1016/j.nds.2014.07.049.

[50] B. Mijnheer, S. Beddar, J. Izewska, and C. Reft, "In vivo dosimetry in external beam radiotherapy," *Med Phys.* **40(7)** (07, 2013) 070903, https://pubmed.ncbi.nlm.nih.gov/23822404/. https://doi.org/10.1118/1.4811216.

[51] B. Mijnheer, S. Beddar, J. Izewska, and C. Reft, "DIODE IN VIVO DOSIMETRY FOR PATIENTS RECEIVING EXTERNAL BEAM RADIATION THERAPY," *AAPM REPORT* **87** (02, 2005) 1–84. https://www.aapm.org/pubs/reports/RPT_87.pdf.

[52] "Development of Procedures for In Vivo Dosimetry in Radiotherapy," *IAEA Human Health Reports* **8** (2013) 978–92–0–141610–0, https://www.iaea.org/publications/8962/development-of-procedures-for-in-vivo-d

[53] P. A. J Izewska, "The IAEA/WHO TLD postal programme for radiotherapy hospitals," *Radiother Oncol.* **54(1)** (01, 2000) 65, https://pubmed.ncbi.nlm.nih.gov/10719701/. https://doi.org/10.1016/s0167-8140(99)00164-4.

[54] C. S. Reft, "The energy dependence and dose response of a commercial optically stimulated luminescent detector for kilovoltage photon, megavoltage photon, and electron, proton, and carbon beams," *Medical Physics* **36(5)** (04, 2009) 1690, https://aapm.onlinelibrary.wiley.com/doi/full/10.1118/1.3097283. https://doi.org/10.1118/1.3097283.

[55] H. Grote and F. Schmidt, "MAD-X: An upgrade from MAD8," *Conf. Proc. C* **030512** (2003) 3497.

[56] L. N. et al, "BDSIM: An accelerator tracking code with particle-matter interactions," *Computer Physics Communications* (2020) 107200.

[57] PulsarPhysics, "General Particle Tracer,". http://www.pulsar.nl/gpt/index.html.

[58] R. A. Fonseca, L. O. Silva, *et al.*, "OSIRIS: A Three-Dimensional, Fully Relativistic Particle in Cell Code for Modeling Plasma Based Accelerators," in *Computational Science — ICCS 2002*, pp. 342–351. 2002.

[59] M. Eshraqi, G. Franchetti, and A. M. Lombardi, "Emittance control in rf cavities and solenoids," *PR STAB* **12** (2009) 024201.

[60] B. E. Carlsten, "Emittance growth of an intense electron beam in a focusing channel," in *Proceedings, 1997 Particle Accelerator Conference (PAC 97): Vancouver, Canada, May 16, 1997*, pp. 1914–1916. 1997.

[61] N. Tsoupas *et al.*, "Uniform Beam Distributions Using Octupoles," *Proceedings of PAC 1991* (1991) 1695–1697.

[62] E. Urakabe *et al.*, "Beam-Profile Control Using an Octupole Magnet," *Jpn. J. Appl. Phys.* **38** (1999) 6145–6149.

[63] T. Amin, R. Barlow, S. Ghithan, G. Royb, and S. Schuhb, "Formation of a uniform ion beam using octupole magnets for BioLEIR facility at CERN," *JINST* **13** (2018) P04016.

[64] S. Machida, "Scaling Fixed-Field Alternating-Gradient accelerators with reverse bend and spiral edge angle," *Phys. Rev. Lett.* **119** no. 6, (2017) 064802, arXiv:1701.06782 [physics.acc-ph].

[65] "International Organization for Standardization, "Cleanrooms and associated controlled environments — Part 1: Classification of air cleanliness by particle concentration," Tech. Rep. ISO 14644-1:2015, International Organization for Standardization, 2015," https://www.iso.org/standard/53394.html, 2015.

[66] "Green transformation for UK science estate," https://www.ukri.org/news/green-transformation-for-uk-science-estate/, 2023.

[67] "STFC Sustainability Design Principles," https://stfc365.sharepoint.com/sites/SPADE/SitePages/Sustainable-Design-Principles.aspx, 2023.

[68] "STFC Sustainable Building Design Guide V3," https://www.stfc.ac.uk, 2023.

[69] "RIBA Sustainable Outcomes Guide (RIBA, 2019)," https://www.engc.org.uk/engcdocuments/internet/website/RIBA%20Sustainable%20Outcomes%20Guide%202019.pdf, 2019.

[70] "RIBA Plan of Work (RIBA, 2020)," https://www.architecture.com/knowledge-and-resources/resources-landing-page/riba-plan-of-work, 2020.

[71] "Net Zero Estate Playbook," https://www.gov.uk/government/publications/net-zero-estate-playbook, November, 2021.

[72] "BREEAM," https://bregroup.com/products/breeam/, 2023.

[73] UK Government, "The Ionising Radiations Regulations 2017 (UK Statutory Instruments No. 1075)," https://www.legislation.gov.uk/uksi/2017/1075/contents/made, 2017.

[74] F. S. Englbrecht, A. Döpp, *et al.*, "Radiation protection modelling for 2.5 Petawatt-laser production of ultrashort x-ray, proton and ion bunches: Monte Carlo model of the Munich CALA facility," *Journal of Radiological Protection* **40** no. 4, (Sep, 2020) 1048. https://dx.doi.org/10.1088/1361-6498/aba8e4.

[75] International Electrotechnical Commission, *Functional safety of electrical/electronic/programmable electronic safety-related systems*. International Electrotechnical Commission, 2010.

[76] International Standards Organisation, "ISO 13849-1:2015; Safety of machinery — Safety-related parts of control systems — Part 1: General principles for design," https://www.iso.org/standard/69883.html, 2015.

[77] International Electrotechnical Commission, "IEC 61511-1:2016+AMD1:2017 CSV Consolidated version; Functional safety - Safety instrumented systems for the process industry sector - Part 1: Framework, definitions, system, hardware and application programming requirements," https://webstore.iec.ch/publication/61289, 2017.

[78] International Electrotechnical Commission, "IEC 62061:2021; Safety of machinery - Functional safety of safety-related control systems," https://webstore.iec.ch/publication/59927, 2021.

[79] "ITRF draft schematic diagram. 1272-pa1-pm-sch-0001-v3.0-ITRF schematic," https://stfc365.sharepoint.com/sites/ITRF/, 2023.

[80] "LhARA draft device naming convention proposal. Document: 1272-pa1-ctrl-rpt-0001-v0.5-LhARA-device-naming," https://stfc365.sharepoint.com/sites/ITRF/, 2023.

[81] "ISO 8573-1:2010 (Compressed air)," https://www.iso.org/standard/46418.htmll, 2010.

[82] K. J. Kirkby, N. F. Kirkby, N. G. Burnet, H. Owen, R. I. Mackay, A. Crellin, and S. Green, "Heavy Charged Particle Beam Therapy and Related New Radiotherapy Technologies: The Clinical Potential, Physics and Technical Developments Required to Deliver Benefit for Patients with Cancer," *The British Journal of Radiology* **93** no. 1116, (2020) 20200247, https://doi.org/10.1259/bjr.20200247. https://doi.org/10.1259/bjr.20200247. PMID: 33021102.

[83] G. Aymar *et al.*, "LhARA: The Laser-hybrid Accelerator for Radiobiological Applications," *Frontiers in Physics* **8** (2020) . https://www.frontiersin.org/articles/10.3389/fphy.2020.567738.

[84] H. Norman, R. Appleby, E. Benedetto, M. Karppinen, H. Owen, and S. Sheehy, "Performance Study of the NIMMS Superconducting Compact Synchrotron for Ion Therapy with Strongly Curved Magnets," *JACoW IPAC* **2022** (2022) 3014–3017. https://cds.cern.ch/record/2845833.

[85] M. Vretenar, M. E. Angolettai, G. Bisoffi, J. Borburgh, L. Bottura, K. Paļskis, R. Taylor, G. Tranquille, E. Benedetto, and M. Sapinski, "A Compact Synchrotron for Advanced Cancer Therapy with Helium and Proton Beams," *Journal of Physics: Conference Series* **2420** no. 1, (Jan, 2023) 012103. https://dx.doi.org/10.1088/1742-6596/2420/1/012103.

[86] X. Zhang, "Lattice Design of a Carbon-Ion Synchrotron based on Double-Bend Achromat Lens." 2020. https://arxiv.org/abs/2007.11787.

[87] V. Chohan *et al.*, *Extra Low ENergy Antiproton (ELENA) ring and its Transfer Lines: Design Report*. CERN Yellow Reports: Monographs. CERN, Geneva, 2014. https://cds.cern.ch/record/1694484.

[88] cpymad 1.14, https://hibtc.github.io/cpymad/. (Accessed: 14.08.2023).

[89] U Amaldi and J. Balosso and M Dosanjh and J Overgaard and S Rossi and M Scholz and B Singers Sorensen, *A Facility for Tumour Therapy and Biomedical Research in South-Eastern Europe*. CERN Yellow Reports: Monographs. CERN, Geneva, 2019. https://e-publishing.cern.ch/index.php/CYRM/issue/view/88.

[90] "Pantechnik ECR Ion Sources," https://www.pantechnik.com/ecr-ion-sources. (Accessed: 17.03.2023).

[91] M. Muramatsu and A. Kitagawa, "A Review of Ion Sources for Medical Accelerators," *Review of Scientific Instruments* **83** no. 2, (2012) 02B909, https://doi.org/10.1063/1.3671744. https://doi.org/10.1063/1.3671744.

[92] E. Benedetto, "Carbon Ion Compact Medical Synchrotron: Key Parameters, CERN-ACC-NOTE-2022-0017, NIMMS-Note-008,". https://cds.cern.ch/record/2812328.

[93] P. J. Bryant, "Resonant extraction," *CERN Yellow Rep. School Proc.* **5** (2018) 315.

[94] R. Taylor, E. Benedetto, M. Sapinski, and J. Pasternak, "Slow Extraction Modelling for NIMMS Hadron Therapy Synchrotrons," *Journal of Physics: Conference Series* **2420** no. 1, (Jan, 2023) 012101. https://dx.doi.org/10.1088/1742-6596/2420/1/012101.

[95] F. Kühteubl, "Masters Thesis: Design Study of Radio Frequency Knockout Slow Extraction for the MedAustron Synchrotron," https://doi.org/10.34726/hss.2020.77640, 2020.

[96] J. Beringer *et al.*, "Review of Particle Physics," *Physical Review D* **86** no. 11, (2012) 010001.

[97] M. K. Hamad, "Bragg-curve simulation of carbon-ion beams for particle-therapy applications: A study with the GEANT4 toolkit," *Nuclear Engineering and Technology* **53** no. 8, (2021) 2767–2773. https://www.sciencedirect.com/science/article/pii/S1738573321001017.

[98] U. Amaldi, "Lectures at the Nuclear Technologies and Clinical Innovation in Radiation Oncology Workshop." 2011.

[99] W. H. B. M.A. and R. K. B.Sc., "XXXIX. On the α particles of radium, and their loss of range in passing through various atoms and molecules," *The London, Edinburgh, and Dublin Philosophical Magazine and Journal of Science* **10** no. 57, (1905) 318–340, https://doi.org/10.1080/14786440509463378. https://doi.org/10.1080/14786440509463378.

[100] H. Owen, R. MacKay, K. Peach, and S. Smith, "Hadron Accelerators for Radiotherapy," *Contemporary Physics* **55** no. 2, (2014) 55–74, https://doi.org/10.1080/00107514.2014.891313. https://doi.org/10.1080/00107514.2014.891313.